Spring 2007

Self -assembly on strained metallic interfaces, and, Novel collective excitations on metal surfaces

Bogdan Diaconescu
University of New Hampshire, Durham

Self-Assembly on Strained Metallic Interfaces
AND
Novel Collective Excitations on Metal Surfaces

BY

Bogdan Diaconescu

B.S., Bucharest University (1998)
M.S., Bucharest University (1999)

DISSERTATION

Submitted to the University of New Hampshire
in partial fulfillment of
the requirements for the degree of

Doctor of Philosophy

in

Physics

May 2007

This dissertation has been examined and approved.

Dissertation director, Karsten Pohl

Associate Professor of Physics

James Harper

Professor of Physics

Olof Echt

Professor of Physics

F. William Hersman

Professor of Physics

Theodore Einstein

Professor of Physics, University of Maryland

05/11/2007

Date

ACKNOWLEDGMENTS

This work is the culmination of many years of effort, the success of which would not have been possible without the help of many people. I would like to thank my advisor Karsten Pohl for being an inspiring mentor. He gave me all the freedom I needed, I could not ask for more. When I started the journey of becoming an experimentalist he taught me a great deal about UHV directly and indirectly through the scientists to whom he introduced me. His permanent advise and encouragement to ask the experts in the field has brought me in contact with great people and outstanding scientists. And the travels for experiments and conferences were great.

I would like to thank my doctoral committee. Thanks to Olof Echt, Ted Einstein, Jim Harper, and Bill Hersman. I know that I have pushed your schedule in the end and I truly appreciate you working with me to make it happen.

Many thanks to Iulian Ruset and Diana; without their friendship life would have been less fun around. Cristian Cocheci has contributed to my well being along the way, especially in my first months here and during Qual preparations when I was as stressed as a student can be. I will always remember the Friday nights at 3 Foss Farm listening to Pheonix and discussing theories of life. Noroc!

In the lab, many thanks to my colleagues Georgi Nenchev and Jiebing Sun. They have been a continuous source of entertainment and scientific and non scientific debate.

In the time when I was building and setting up the VT-STM chamber at UNH, the projects in Aarhus were a nice variation. Philip Hofmann had a great influence during that

time, as an experimentalist I really appreciate now the experience gained breaking things. Thank you Philip for continuously opening your lab to me.

A very unforgettable experience I had in Genoa, when Mario Rocca and Luca Vattuone spent so many hours helping me with the EELS measurement, and most importantly, walking me through the Italian bureaucracy. Thank you for all your help.

Along the way, various discussions with Norman Bartelt have helped me understand how to interpret my STM data. He has shown great patience when I was asking the same question few times; I am grateful for his constant advice.

I would also like to thank Slava Silkin and Eugene Chulkov for their hard work in computing the acoustic surface plasmon on Be(0001) and for their ideas that triggered my interest in this subject.

As a first year student, sharing the cubicle with Pete Karpius has been a very entertaining experience. Thank you Pete for all the advise and most importantly, for really teaching me how to ski.

Finally, I would like to thank my family, for all your unconditional support and love.

Table of Contents

List of Figures

ABSTRACT

SELF-ASSEMBLY ON STRAINED METALLIC INTERFACES

AND

NOVEL COLLECTIVE EXCITATIONS ON METAL SURFACES

by

Bogdan Diaconescu
University of New Hampshire, May, 2007

Recent interest in novel physical properties of reduced dimensional systems is spurred by the advance of investigation methods at the nanoscale. Understanding bottom–up techniques for the growth of nanomaterials with novel physical, chemical, and mechanical properties require specialized investigation tools.

I am presenting a novel design and performance of an ultra high vacuum scanning tunneling microscope (STM) that allows for large scale (8 μm $\times$ 8 μm), fast scanning (3 s for a 100 Å$\times$100 Å frame), and atomically resolved studies of reduced dimensional systems on metallic surfaces. The STM proved excellent performance, allowing for variable temperature (100 K to 700 K) and high resolution ($<$ 2 pm at 300 K) structural and dynamical studies on surfaces, as shown by the STM study of the general types of self–assembly processes on strained metallic interfaces.

With this new instrument, I performed a complete experimental investigation of the misfit dislocation network of one atom thick Ag films on Ru(0001) and of the restructuring induced by molecular sulfur adsorption when S filled Ag vacancy island are formed. The experiments suggest that the mechanism through which hundreds of Ag atoms are rearranging themselves following S deposition is driven by a process of threading dislocation

pair annihilation and glide. The experimental observations are explained via an atomistic model, which is based on first–principles interaction parameters. I have found that the self–assembly process is driven by stress relaxation in the Ag film.

While the first part of my thesis is focused on the structural properties of low–dimensional metallic systems and instrumentation methods needed to access the nano–scale, in the second part I investigated a novel low–energy electronic excitation of a metallic surface. I am presenting the first experimental measurement of an acoustic surface plasmon on metal surfaces. The experiment was performed using electron energy loss spectroscopy on Be(0001). This new mode is a collective excitation of the surface electrons. This discovery goes against the traditional wisdom that on metal surfaces only regular (optical) surface plasmons can exist. First–principles calculations show that this mode is caused by the coexistence of a partially occupied surface state band with the underlying bulk electrons.

CHAPTER 1

INTRODUCTION

1.1 Motivation

In the last decade, a tremendous worldwide effort is underway towards understanding the world of nanoscience, where, as the name implies, the characteristic length scales involved are of the order of few nanometers. A generally accepted definition being that at least one of the three dimensions of the system is reduced to a value below 100 nm. The explosion of both academic and industrial interest is fueled by the remarkable diversity and novelty of fundamental electronic, optical, catalytic, magnetic, ferroelectric, chemical, biological, and mechanical properties as dimensions are reduced from extended (periodic) solids to finite systems composed of just few atoms or molecules. The building blocks of nanostructures are atoms [1], molecules [2], clusters, and nanoparticles [3, 4], and they can be used to fabricate or grow advanced and totally new phases of condensed matter at the nanoscale [5, 6, 7, 8]. It is believed that by tailoring the dimensions, symmetry, and structure and by controlling the interactions between these building blocks, it will be possible to design novel functionalities in unprecedented ways.

As Feynman observed in his famous talk *'There is Plenty Room at the Bottom'* [9], studying the nano–world requires the development of new experimental techniques and specific instrumentation, which might also allow for the modification or manipulation of it.

The development of scanning tunneling microscope (STM) by Binnig and Rohrer [10, 11, 12] has opened the door towards real space, atomically resolved studies of surfaces and surface hosted systems. The nature of the method, which exploits the quantum mechanical tunnel current that flows between an atomically sharp electrically conductive tip and a conductive surface, allows for imaging surfaces with sub–Ångström resolution. Soon after, the advent of a family of related scanning probe microscopy (SPM) techniques [13, 14, 15] – atomic force microscope (AFM), scanning near field optical microscope (SNOM), magnetic force microscope (MFN) – was largely responsible for the emergence of nanoscience as a novel field of research. Although STM does not have strong chemical sensitivity, it has proven a powerful tool for the real space study of surface hosted processes as diffusion, adsorbed–surface interactions [16, 17, 7, 6], manipulation of individual adsorbates by careful control of tip–surface interactions [1, 18, 19], and more recently atomic scale chemical transformations [20, 21] and synthesis [22].

Even if STM (and SPM related techniques) is a very valuable tool for research of nanostructure fabrication and study of the interactions between nano building blocks and surfaces and with each other, the serial nature of the process involved, which is therefore inherently slow, limits dramatically the number of building blocks that could be assembled together. This has triggered a search for alternative methods for faster, parallel type, nanofabrication.

1.2 Self–assembly at surfaces

Very often nanomaterials are synthesized from atoms and molecules rather than being fabricated in the conventional lithographic approach. This bottom–up synthesis differs radically from the traditional top–down methods. Therefore, key to advancement toward nanomaterials is the ability to precisely understand and control the dynamics of growth

and self-assembly processes of nanoscale structures on an atomic level. These objectives are more or less directly related to the exploration of surface and thin film phenomena, in particular heteroepitaxial growth and interfacial stress [23, 24].

Ultrathin films, clusters and macromolecules on solid surfaces have been observed to self-assemble in ordered patterns with well-defined periodicities from a few to few tens of nanometers [5, 6, 7, 8, 25, 26], in a wide variety of systems, including surface dislocation arrays [27, 28, 29, 30], domain structures in surface alloys [31, 32, 33, 34], adatom gas induced reconstruction of metal surfaces [35, 36, 37], semiconductor quantum dots and wires [38, 39, 40], and supramolecular self–assembly on surfaces [41, 42]. It is expected that these structures with their specific properties find applications in higher density magnetic storage, more selective catalysis and higher sensitivity biochemical sensors, and photonics. However, the controlled fabrication of such nano-arrays with reproducible properties is a serious challenge, and surface physics has to play a key role in the understanding of their formation and their characterization. Theoretically, a quantitative description is difficult due the low symmetry and large number of constituents of these reduced dimensionality quantum mechanical systems. Various fundamental mechanisms have been proposed to explain the driving forces that control their formation, e.g. interacting electric [43] and bulk elastic strain fields [44, 45] for clusters on metals, and molecular recognition for organic molecules on surfaces [26]. However, many of these systems are way too complex to precisely measure the energies that stabilize these nano-arrays, and do not allow for the development and testing of the detailed atomic models that will shed more light on the fundamental driving forces of nanostructure evolution. Heteroepitaxial systems as one of the few systems for which the detailed atomic structure can be measured, play an important role in the quest for a better understanding of driving forces of nanostructure ordering and growth.

1.3 Self–assembly driven by stress relaxation in metallic ultrathin films

Stress relaxation occurs on clean metal surfaces because the top atomic layer can have different preferred lattice spacing than the underlying bulk crystal due to different electronic properties caused by electron charge redistribution at the surface as shown schematically in Fig. 1-1. Strain is often partially relieved through the formation of well-ordered networks of misfit dislocations [29], which are characterized by partial dislocations formed when a row of N surface atoms sits on top of a row of N±1 atoms in the atomic layer beneath the surface. The herringbone reconstruction of Au(111) is an example of how an ordered misfit dislocation network can form on a clean surface: terminating a Au crystal in a (111) surface leaves the top layer in compression by 4% with respect to the layers below, resulting in this

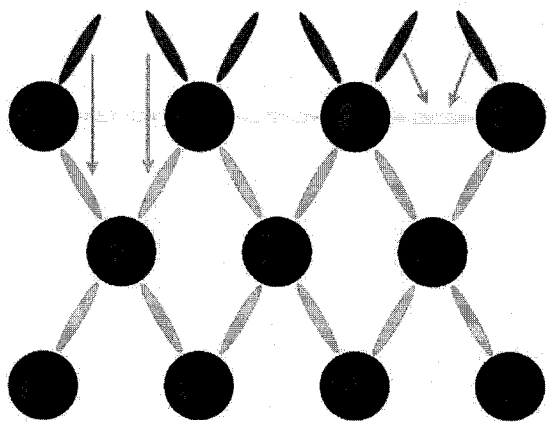

Fig. 1-1: Electronic origins of surface stress: a surface is created, by cleaving a bulk crystal, which has unsatisfied bonds (red). The electronic charge in the missing bond redistributes either between the first and second atomic layer strengthening the backbonds (top green), with the consequence that the interlayer spacing between the surface layer and the next bulk layer changes, or the extra charge redistributes between the surface atoms, which results in a strengthening of the in–surface plane bonds (yellow). In the last case, the in–plane bond length change, resulting in a strained surface layer.

well-known reconstruction [28, 46, 47]. The (111) surface of platinum exhibits a similar reconstruction [48].

In general, growth of a thin film on a dissimilar substrate results in a strained interface due to the lattice mismatch between the two materials. Every crystalline bulk material has a well–ordered bulk crystal lattice structure that is periodic, repeating structural arrangements of atoms (e. g. hexagonal, cubic). Atomic lattices are different for every material and have preferred spacings that arrive from minimization of the cohesive energy. Atoms at the interface are under stress to match the two lattices. As such, there is a competition between the energy cost of strain for the thin film surface to stretch in order to match the lattice space of the substrate and the energy cost for the adatoms to sit out of registry with that surface. Lattice mismatch introduces stress that can significantly influence surface atoms. Many parameters are controlling the type and size of the misfit dislocation networks, with some cases being discussed in Chapter 3 and 4.

The great potential of this template approach in strained thin films is that the feature sizes are believed to be tunable by controlling the misfit. This can be achieved e.g. by adjusting the coverage as has been observed in monolayer thick strained Ag films on Ru(0001) [49]. Preferential nucleation of ad-clusters at the cores of these dislocation networks can lead to highly-ordered functional arrays [27, 30, 33].

Self–assembly of cluster arrays on misfit dislocation networks is a special case because: (i) the ultrathin metallic films, which usually are one atomic layer high, could be thoroughly characterized structurally and dynamically with scanning probe microscopy techniques, and (ii) atomistic models can be constructed based on first–principles atomic interaction parameters and compared with the experimental data, thus revealing the mechanism through which the self–assembly occurs. Moreover, strained metallic interfaces show the ability of

ordered self–assembly on a large scale. Therefore, experimental studies of these systems require large scale, atomically resolves, and fast dynamical imaging of surfaces.

1.4 Scanning tunneling microscopy method

Scanning tunneling microscopy allows direct, real space determination of atomic configurations on conductive surfaces. The basic principle behind STM operation is the concept of quantum mechanical tunneling of electrons between an atomically sharp conductive tip and a conductive surface (Fig. 1-2) which are separated by a vacuum barrier (Fig. 1-3). The simplest way to model the tunneling current [13, 14] is to consider two plane parallel metallic electrodes separated by a distance s and a one dimensional potential barrier of height V_0. Electrons of energy E have inside the barrier wavefunctions $\psi = e^{\pm\kappa z}$ with $\kappa = [2m(V_0 - E)]^{1/2}/\hbar$ and a tunneling probability $T \propto e^{-2\kappa s}$. An important observation is that this exponential dependence of the tunneling probability on the tip–sample distance and the square root of the potential barrier height is typical for tunneling, independent of the exact shape of the barrier. Assuming a barrier width of 5 Å and an effective barrier height of 4 eV (a typical work function for a metal), we get a value of 10^{-5} for the exponential factor. Therefore, changing the barrier width by 1 Å then typically leads to a change of tunneling probability by one order of magnitude. This very strong dependence of the tunneling probability on the barrier width is the reason for the very high resolutions achievable by STM [10, 11, 12].

The very high resolutions attainable with STM depend dramatically on the ability to control the STM tip position with high precision. The usual way to achieve that is to use piezoceramic actuators. Fig. 1-4 shows a schematic of STM tip positioning system and data acquisition. A four quadrant piezoceramic tube is used to control the tip position vertically

and horizontally. The $X - Y$ scan control generates the HV scanning signals needed to move the tip across the surface of the sample in a raster pattern. There are two imaging modes. The first mode is called constant–current mode. Tunneling current is measured and a feedback control circuit automatically adjusts the height of the tip to maintain a preset current value while the tip scans the surface. In this way, the tip–sample distance is maintained constant and a topographic map of the surface is recorded. The vertical distance is inferred from the high voltage value for the Z directions and the sensitivity of the piezotube. The second operation mode is called constant–height mode. It is performed

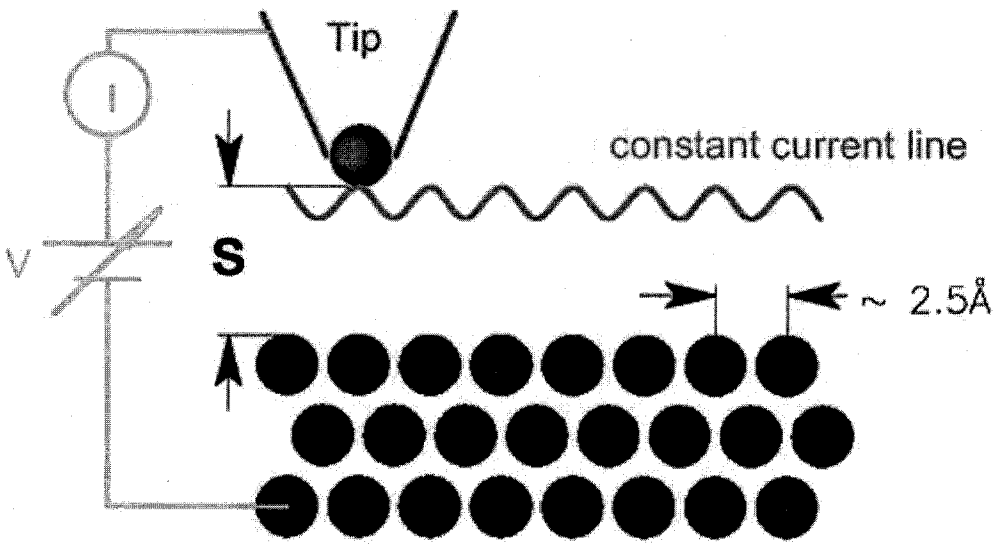

Fig. 1-2: STM tunneling junction. When a bias voltage V is applied, a net tunneling current I flows between the electrodes. Because I depends exponentially on the tunneling junction width s, more than 90% of the tip tunneling current is provided locally by the atom closest to the surface.

by scanning the sample while the vertical controlling signal is maintained constant. In this way, the scanner tube length remains unchanged all the time. The tunneling current is recorded as the Z value and a current map of the sample is obtained. This mode, since it does not employ the feedback loop for the Z direction, allows for higher scanning speeds.

A more careful interpretation of the STM data requires a more detailed calculation of the tunneling probabilities. In the formalism of Tersoff and Hamann [50, 14], which is valid for small bias voltages and temperature, the tunneling current calculated using first order perturbation theory is

$$I = \frac{2\pi e^2}{\hbar} V \sum_{\mu,\nu} |M_{\mu\nu}|^2 \delta(E_\mu - E_F)\delta(E_\nu - E_F) \tag{1.1}$$

where

$$M_{\mu\nu} = \frac{\hbar^2}{2m} \int ds(\psi_\mu^* \nabla\psi_\nu - \psi_\nu \nabla\psi_\mu^*) \tag{1.2}$$

is the tunneling matrix element between electronic states ψ_μ of the tip and ψ_ν of the sample

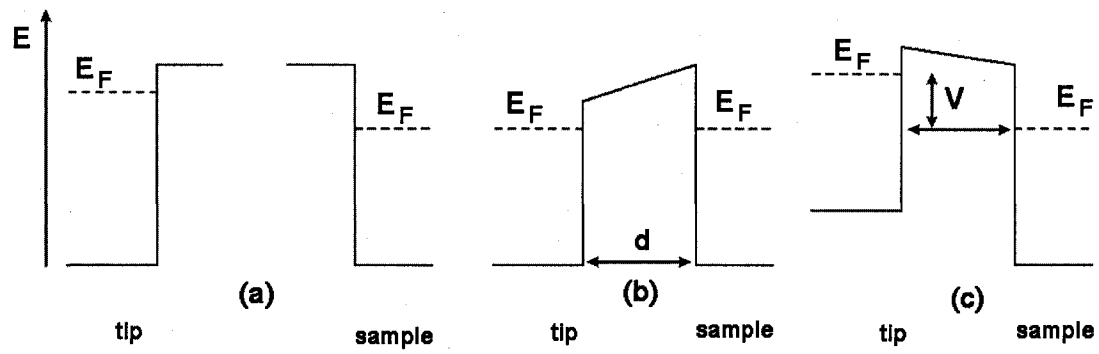

Fig. 1-3: Potential barrier between tip and sample in vacuum: (a) far away, non–interacting electrodes; the work function is the difference between the Fermi levels. (b) Tip and sample in electrical equilibrium, therefore they have the same Fermi level; the work function manifests as an electric field in the vacuum region. (c) a voltage is applied; the Fermi levels differ by eV and the field in the barrier includes contributions from both applied voltage and work function difference. Only electrons between those Fermi levels can tunnel. Typical work functions for metals are in the range of 4 to 5 eV and typical bias voltages applied between tip and sample are less than 1 eV.

surface and E_μ (E_ν) is the energy of the state ψ_μ (ψ_ν). The integral has to be evaluated over any surface lying entirely within the vacuum barrier region separating the two electrodes. When the tip is approximated by a point source of current, whose position is $\vec{r}_0$, the current becomes

$$I \propto V\ n_t(E_F)e^{-2\kappa s}\sum_\nu |\psi_\nu(\vec{r}_0)|^2\delta(E_\nu - E_F) = V\ n_t(E_F)e^{-2\kappa s}n_s(\vec{r}_0, E_F) \qquad (1.3)$$

with the decay rate $\kappa = (2m\phi)^{1/2}/\hbar$ where ϕ is the effective local barrier height, $n_t(E_F)$ is the density of states at the Fermi level for the tip, and $n_s(\vec{r}_0, E_F)$ is surface local density of states (LDOS) at the Fermi level at the tip location. Therefore, the tunneling current is exponentially dependent on the barrier width s, and barrier height κ as expected.

Equation 1.3 indicates that a STM image is a contour map of the surface local density

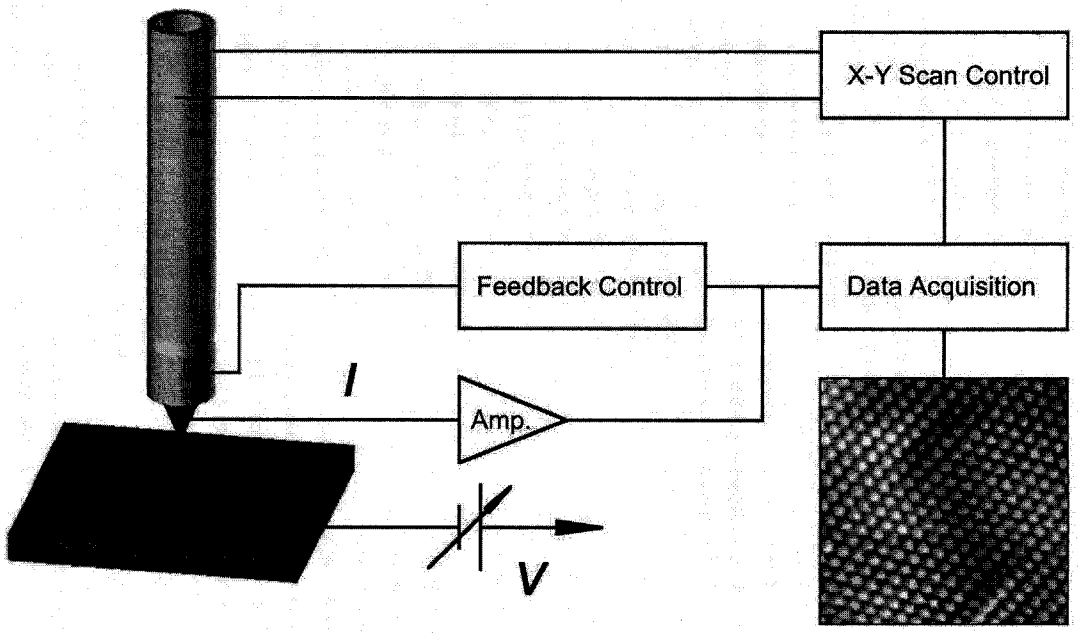

Fig. 1-4: Simplified schematic of the STM operation mode. The tip position is controlled with a piezoceramic actuator able to move both lateral and vertical to the surface. High voltage signals are generated by the electronics and used to bend (lateral movement) and stretch (vertical movement) the scanner tube.

of states evaluated at the Fermi energy of the surface. For simple metals as well for noble and transition metals, the LDOS roughly follows the topography of surface atoms [13, 14].

1.5 Collective electronic excitations at surfaces

The long–range nature of the Coulomb interaction between valence electrons into a metal is known to yield collective behavior known as plasma oscillations, which have a basic unit of energy called plasmon $\hbar\omega_p = \hbar(4\pi ne^2/m_e)^{1/2}$, where n is the valence electron density and m_e is the free electron mass [51, 52].

The termination of a bulk metal by a surface gives rise to surface–localized collective excitations of the electrons, with a 'lowered' energy $\hbar\omega_s = \hbar\omega_p/\sqrt{2}$ as firstly shown by Ritchie [53] and named by Stern and Farrell as surface plasmons [54]. These excitations have a characteristic optical dispersion as shown schematically in Fig. 1-5, i.e. they always have a finite energy, in general a few eV [55, 56, 57, 58]. Surface plasmons have important applications, in plasmon resonance microscopy [59], photonic crystals [60], and the emerging

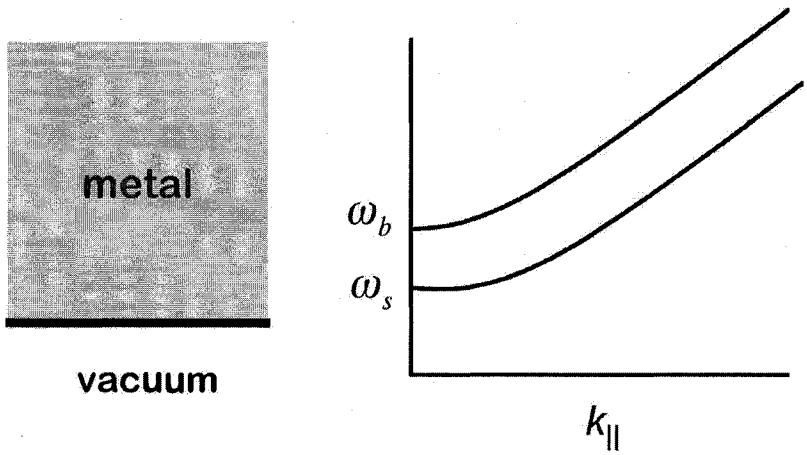

Fig. 1-5: Energy dispersion of bulk ω_b and surface plasmon ω_s (right) of valence electrons bond to the bulk metal and its surface (left); the characteristic energies are of the order of few eV.

field of subwavelength optics [61, 62]. However, due to their high energy they can neither be excited thermally nor do they contribute to the low-energy decay of electrons or phonons.

In contrast to bare metal surfaces, low-energy collective excitation modes have been predicted [63] and found for quasi two–dimensional (2D) electronic systems in layered materials, like the charge inversion layers in metal–oxide–semiconductor [64], and the metallic surface state of Ag on Silicon [65]. Also, low–energy collective excitations have been proposed for quasi two–dimensional electronic systems in the vicinity of a three dimensional (3D) electron gas [66, 67]. In both these cases, the collective mode disperses to zero for long wavelengths. The actual dispersion has a square-root dependence for the pure 2D case (Fig. 1-6), with $\hbar\omega_p^{2D} \propto \hbar v_F^{2D}\sqrt{k_\parallel}$, where v_F^{2D} is the Fermi velocity of the electrons in the 2D electron layer, and is expected to be linear for spatially separated 2D and 3D systems, with $\hbar\omega_p^{2D/3D} \propto \hbar v_F^{2D} k_\parallel$ as depicted in Fig. 1-7. These low–energy collective excitations of energy $\hbar\omega_p^{2D/3D}$, for a 2D electron layer in the presence of a 3D electron system, were proposed to exist *only* for spatially separated plasmas [66, 68].

In the case of Ag on Silicon system, the 2D electron gas is associated with 2D Bloch states which are found to exist on a variety of metals in regions of energy and momentum

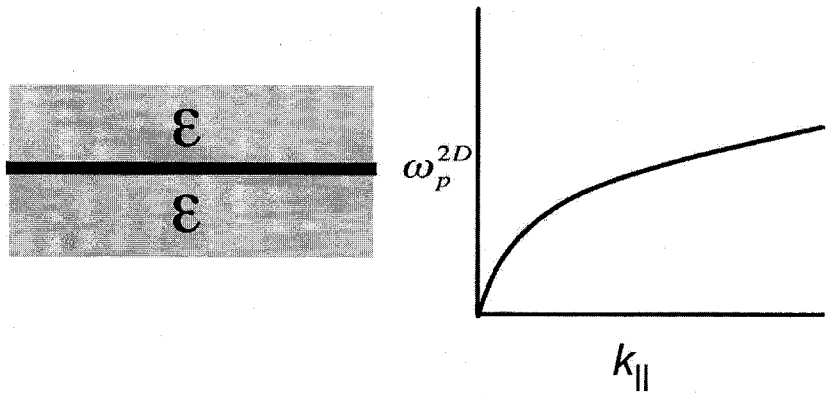

Fig. 1-6: Energy dispersion of a plasmon for a 2D electron gas ω_p^{2D} (right) embedded into a dielectric ϵ (left). The 2D plasmon energy depends on the $\sqrt{k_\parallel}$.

space forbidden for bulk states as a result to bulk band gap [69]. Therefore, these systems represent a promising area for exploring not only plasmons in a 2D electron gas, but also new physics that can arise from coupling of the 2D Bloch states with the bulk states.

Crystal surfaces are known to support electronic surface states, which are different than the bulk crystal electronic states, and they arise from the crystal symmetry breaking in the direction perpendicular to the surface. Since the potential felt by an electron is zero on the vacuum side of the surface, and periodic with the surface lattice periodicity in the surface plane, the solutions to the Schrödinger equation will have the form $u_{\vec{k}_{\|}(\vec{r}_{\|})} e^{i\vec{k}_{\|}\cdot\vec{r}_{\|}} e^{-k_{\perp}r_{\perp}}$, with an evanescent component perpendicular to the surface and a periodic component in the plane of the surface. Since these waves decay both in the vacuum and in the bulk, they are localized at the surface and called surface states. These two–dimensional Bloch states are characterized by the quantum number $\vec{k}_{\|}$ and an energy $E(\vec{k}_{\|})$ but not by $k_{\perp}$ because of the broken symmetry in the direction normal to the surface. True surface states exist in regions of energy and momentum space forbidden to bulk states, while surface resonances might overlap with bulk states. Surface states have been observed (Fig. 1-8) by angle resolved photoemission experiments, like in the case of Be(0001) surface [70].

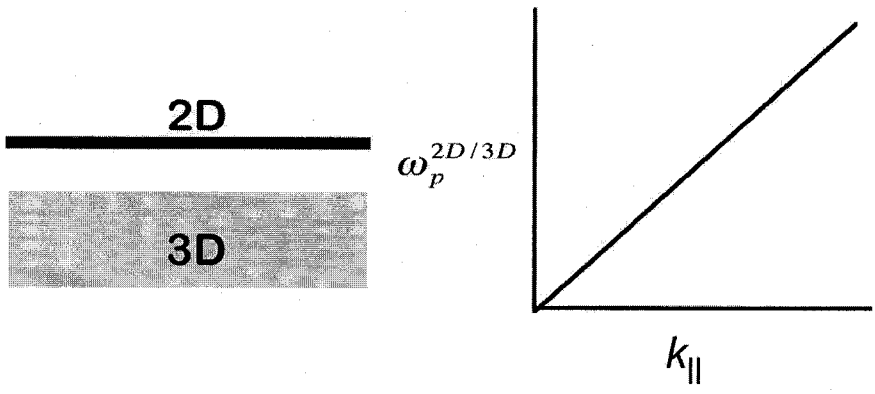

Fig. 1-7: Energy dispersion of a plasmon $\omega_p^{2D/3D}$ (right) for a 2D electron gas in the presence of a 3D electron system (left). The 2D plasmon energy depends on the $k_{\|}$.

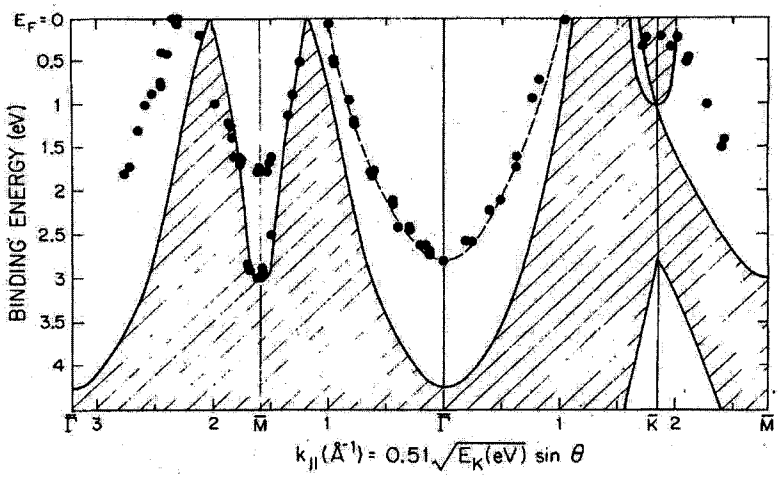

Fig. 1-8: Dispersion of the surface states along the high symmetry directions of the surface Brillouin zone of Be(0001) as a function of $k_{\|}$. The shaded area is the projected bulk states. Image from Ref. [70].

In the last part of my thesis (Chapter 5) I will present the first measurement of a low–energy collective excitation on a clean metal surface [71]. The very existence of collective low-energy excitations could have a profound effect on the physics of the systems in question. Indeed, low-energy collective excitations have even been proposed as possible candidates to mediate the attractive interaction responsible for the formation of Cooper pairs in high T_c superconductors [72, 73].

1.6 Thesis summary

- Chapter 1, *Introduction*, motivates the need for a better understanding of the nanosystems and the need for better investigative methods at the nanoscale.

- Chapter 2, *Variable–Temperature Scanning Tunneling Microscope*, describes the new design, development, and performance of a home built scanning tunneling microscope, which allows for large scale and fast–scanning atomically resolved investigation of

metallic surfaces.

- Chapter 3, *Self–organized nanotemplating on metallic misfit dislocation networks*, presents various self–assembly mechanisms of ordered arrays of clusters on strained metallic interfaces which have been investigated with the VT–STM. It empathizes the need of large scale atomically resolved and fast dynamical experimental data to explain the self–assembly processes on large systems involving a few hundreds to thousands of atoms.

- Chapter 4, *Self–assembly of 2D nanocluster arrays via dislocation pair annihilation and glide*, is focused on a detailed structural and dynamical case study of a self–assembly mechanism for S adsorbed on one atomic layer thick Ag film on Ru(0001). Atomically resolved STM data show how the self–assembly process, triggered by S_2 adsorbtion on the misfit dislocation network of Ag on Ru(0001), is driven by stress relaxation in the Ag film. An atomistic model based on first–principles interaction parameters between the atoms in the system is employed to explain the experimental data.

- Chapter 5, *Acoustic surface plasmon on Be(0001)*, presents a novel collective electron excitation on a dimensionally reduced nano system, the surface of Be(0001). Its energy momentum dispersion has been measured by electron energy loss spectroscopy and first–principles calculations show that it is the result of the single electron surface states crossing the Fermi level, which are dynamically and non–locally interacting with the bulk electron states, resulting in a collective oscillation of the surface electrons in the surface plane.

- Chapter 6, *Conclusions*, is a short description of the results presented in this thesis.

Chapter 2

Variable–Temperature Scanning Tunneling Microscope

2.1 Introduction

Scanning tunneling microscope (STM) [12] has proven to be a powerful tool for the real space investigation of surfaces and surface hosted phenomena. Its high spatial resolution makes it an important technique for studying atomic configurations of surfaces and adsorbate molecular aggregates with pico-meter resolution and also allows studies of the local electronic properties. Dynamical processes like nucleation and growth, self–assembly, surface diffusion, and chemical reactions can also be investigated. Both static and dynamical studies can hugely benefit from having a system able to operate in a large temperature range.

I have built a variable–temperature scanning tunneling microscope integrated in a new ultra high vacuum chamber for the surface studies in the group of Karsten Pohl, in the Department of Physics of University of New Hampshire. The primary motivation in designing and building a variable temperature STM came from the need of having a versatile system aimed at large scale atomically resolved static and fast dynamical studies of strained metallic interfaces and self–assembly processes onto them.

2.2 Instrument design

Designing an STM able to achieve sub–Ångstrom resolutions in a large temperature range while having low thermal drifts and integrating it into a larger surface science UHV chamber is a challenging task. The sub–Ångstrom resolution requires a careful design of the vibration isolation system where the usual approach is a two–stage damping for high and low frequencies [74]. Also, maintaining the ability to probe the same sample area after a large temperature change (few tens of degrees Kelvin) imposes hard restrictions on the thermally associated drifts. Other desired features are the ability to change sample temperature at a fast rate, the possibility of finding the same surface area after sample preparation, and also the design needed to accommodate a larger UHV chamber for surface science studies. To address all these restrictions, an in–vacuum damping–cooling system with a large bath cryostat [75] has been chosen. It has the advantage of being vibration–free and also, due to its large mass, it proved to be quite impervious to external vibrations which makes it well suited for a chamber having no external vibration isolation. Another design direction was to build a very rigid STM head with low thermal expansion, axial symmetry, and a self aligning sample holder – STM head system which allows for repeated investigations of the same sample area even after various sample preparation stages.

2.2.1 Vibration isolation and cooling system

A three dimensional and on scale rendering of the vibration isolation with the cold bath ensemble is presented in Fig. 2-1. It consists of a large cylindrical Al-6061 block (approx. 7 Kg) which rests on four spring-steel springs. The elastic constant of the springs has been chosen such that the resonant frequency of this ensemble is close to 1.5 Hz. An eddy current damping system consisting of twelve Sm-Co magnets which are protruding between Al fins

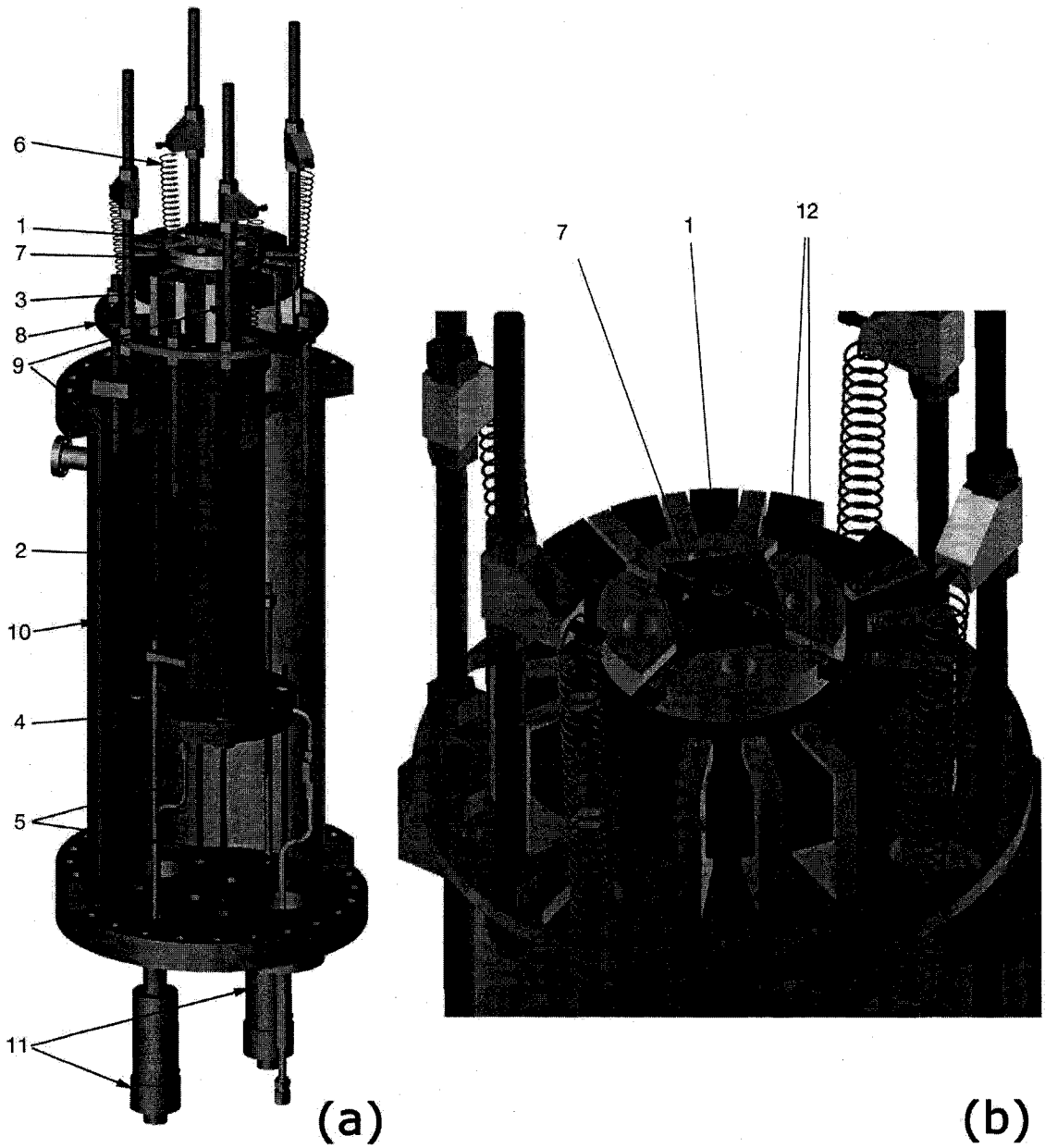

Fig. 2-1: Flange–on STM cryogenics and vibration isolation assembly: (a) all parts view and (b) inset of the sample holder area; (1) sample holder, (2) Al cold reservoir, (3) Sm-Co magnet assembly, (4) cold finger, (5) coolant feed-through, (6) springs, (7) sample holder Cu base, (8) St-St magnets ring holder, (9) threaded rods, (10) UHV chamber, (11) linear motion manipulators, (12) flat springs providing electrical contact for the sample's filament and the C-type thermocouple.

machined at the top side of the Al block are distributed in a circular fashion. An OFHC copper disk carrying the electrical contacts for the filament and thermocouple acts as a support and thermal path for the sample holder. A polished sapphire disk [76] mounted between the top part of the Al block and the copper disk electrically isolates the sample from the large bath cryostat while providing good thermal conduction at low temperatures. The sample is mounted inside the OFHC copper sample holder which contains a C–type thermocouple (a junction of a Tungsten–5% Rhenium wire with a Tungsten–26% Rhenium wire) required for high temperature annealing needed to prepare refractory metal surfaces like Ru(0001), and a filament. The heating of the sample could be done both by electron bombardment for high temperatures, larger than 2000 K, or radiatively when moderate temperatures are required. In order to reliably measure the temperature of the sample in the range between 70 K and 2500 K, a full C–type thermocouple line is used, which is made of the same alloys like the thermocouple itself. A second K–type thermocouple (Nickel–Chromium vs. Nickel–Aluminum) is mounted on the copper disk supporting the sample holder for the purpose of individual C–type thermocouple calibration in the cryogenic range while at thermal equilibrium. The design of the sample holder which contains a W filament and a C–type thermocouple allows for cooling and heating of the sample to be done in the STM scanning position as well as in the manipulator thus preparation of the sample and investigation with other tools being possible under controlled conditions in the whole temperature range. The sample holder is held in place in the STM scanning position by a μ–metal disk bolted to the underside and a magnet mounted in the sample holder Cu base (Fig. 2-1), which also caries the electrical contacts for the filament and C–type thermocouple mounted in the sample holder.

The cooling of the assembly is done by pulling down the bath cryostat in contact with

the cold finger made out of OFHC copper which is cooled with liquid nitrogen. The liquid nitrogen flows through a zig–zag channel machined in the copper body of the cold finger in order to maximize heat transfer and streamline the flow. In order to thermally isolate the bath cryostat, various Vespel® [77] and Al_2O_3 breakers have been placed between the mounting points of the springs and the chamber in this way slowing down the warm–up speed to $\approx$ 3 K/h around 100 K. While the cooling down of the bath cryostat takes about 6 h from room temperature to 90 K when using liquid nitrogen as coolant, the sample holder cooling down time from room temperature to 90 K is about 10 min.

When measurements are performed, the bath cryostat is released and is supported only by the springs, thus serving as a vibration–free cold reservoir for the sample holder, with the STM head sitting on the top of the sample holder. Any desirable sample temperature above the bath cryostat's temperature can be reached and maintained by radiatively heating the sample. Such a large bath cryostat needs a supplemental way of heating if fast warm–up speeds are needed. For this purpose a set of four BZY93V75 Zener diodes have been mounted along the bottom circumference of the bath cryostat with other four diodes on the circumference of the cold finger.

2.2.2 STM head

A compact, rigid, axially symmetrical STM head construction is desirable to achieve low noise and low thermal drifts. Fig. 2-2 shows (a) a side cross section and (b) a bottom view of the STM head. The main body is machined out of gold–plated invar (a second STM head with a body built out of tantalum was tested showing the same drift characteristics as the invar one) which has a cylindrical shape in order to minimize lateral thermal drifts. The STM head consists of two functionally distinctive assemblies, the STM scanner which

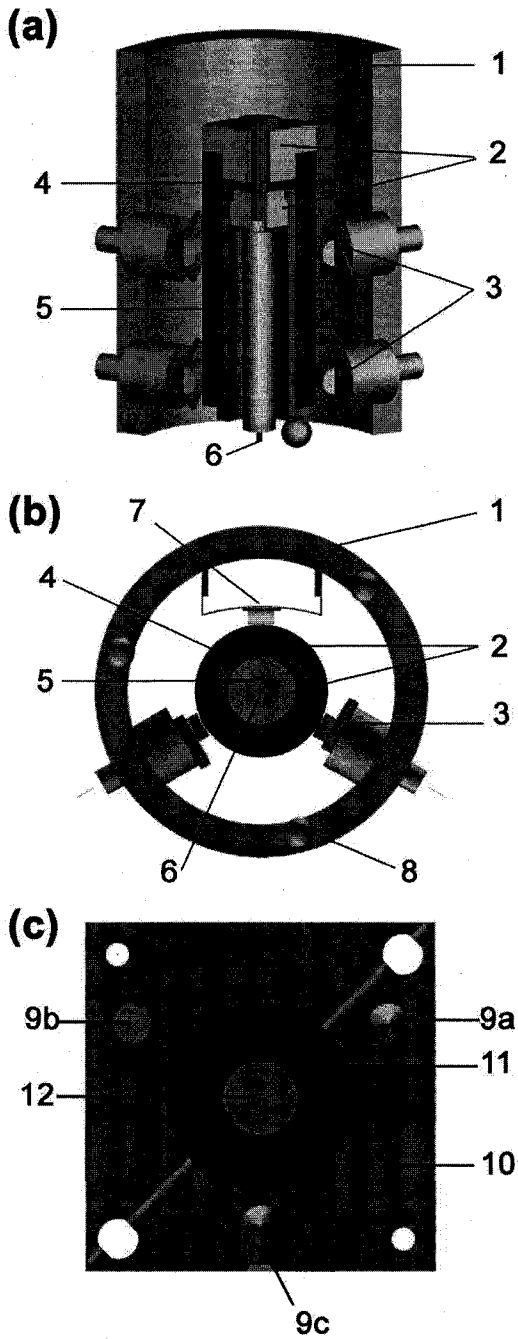

Fig. 2-2: STM cross section view with the spring removed for clarity (a), bottom view (b), and sample holder (c); STM Invar body (1), STM tube holder assembly (2), coarse motor piezo–stacks (3), sapphire tube (4), four–quadrant scanner tube (5), STM tip (6), spring (7), glass balls (8), self alignment grooves for the STM glass balls with conical (9a), cylindrical (9b), and edge profile (9c), OHFC copper body (10), Ta washer (11), and sample crystal(12).

provides the scanning abilities for STM measurements and the STM coarse approach motor assembly which is required to bring the STM tip in the proximity of the surface of the sample to be investigated.

STM scanner design and calibration

The STM body houses the STM's four quadrant piezoscanner tube mounted axially in a sapphire cylinder [76] with a 5 μm polished outer surface (Fig. 2-2) Various lengths of the scanner tube can be accommodated with a proper choice of the STM tube holder length. We are currently using EBL–1 piezoceramic with Ni electrodes of 19 mm length in order to achieve a large lateral scan range of 8 μm $\times$ 8 μm [78].

In order to achieve a construction which is as rigid as possible, therefore having mechanical resonance frequency modes as high as possible, the STM scanner assembly is mostly glued together with UHV compatible epoxy. An exploded view of the STM scanner is shown in Fig. 2-3a, with the places where the components are glued together marked in yellow, while Fig. 2-3b shows how the scanner tube is axially mounted inside the sapphire tube via a vented stainless steel (St.–St. 316) screw. The sapphire tube has an outer surface polished with 5μm precision and is thus providing a smooth sliding surface for the Al_2O_3 pads of the piezo–stack motors used for coarse movements of the scanner. All the scanner tube wiring is done with 0.15 mm diameter Kapton insulated Cu wires. The wires are axially guided along the STM tube further away from the STM tip. The holes in the St.–St. 316 scanner tube base and scanner end cap provide a way to guide the wires at the top of the assembly. Soldering of the Cu wires on the STM tube Ni electrodes need to be done at the lowest heat transfer possible to avoid extensive depolarization of the piezoceramic. Functional scanners are characterized by larger capacitances between the central, inner electrode and any of the

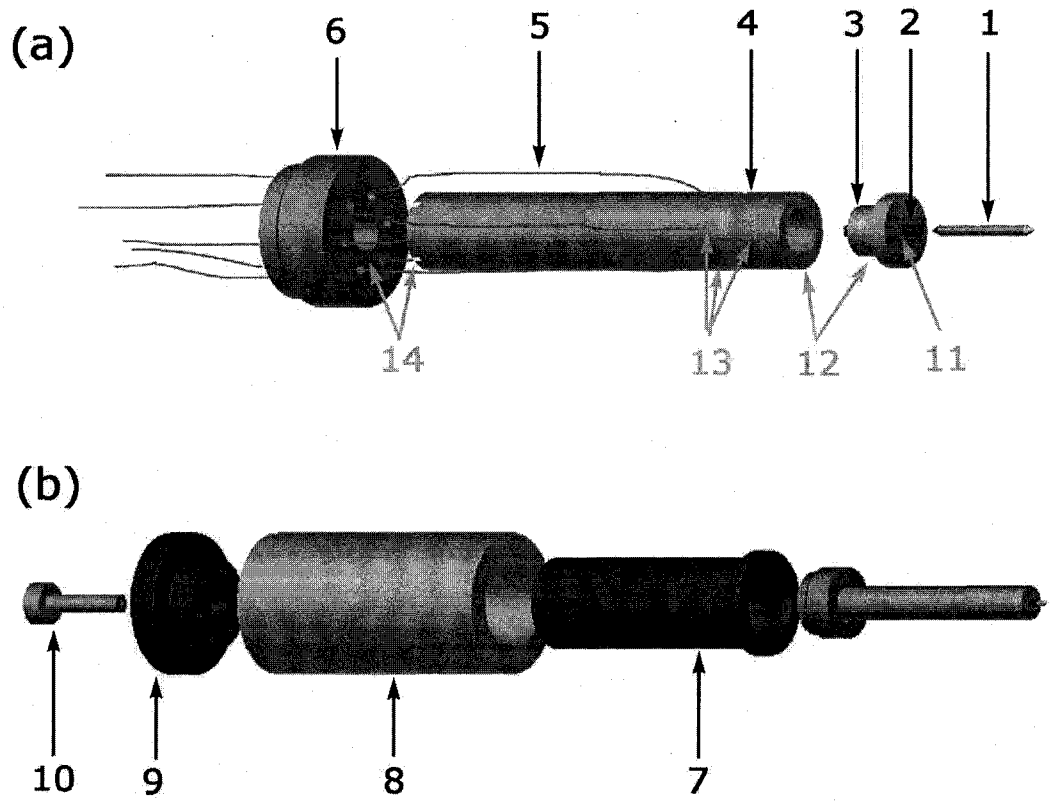

Fig. 2-3: STM scanner construction – exploded view: (a) enlarged view of the scanner tube only and (b) scanner tube housing; (1) 0.25 mm diameter, double end etched STM tip, (2) St.–St. 316 hypodermic tube, (3) Macor hat washer, (4) four quadrant piezoceramic tube with inner electrode, (5) 0.15 mm diameter Kapton insulated oxygen free tempered copper wires, (6) St.–St. 316 scanner tube base, (7) St.–St. 316 sapphire tube sleeve, (8) sapphire tube, (9) St.–St. 316 scanner end cap, (10) vented screw; non conductive epoxy is used to glue the parts at junctions 11, 12, and 14 and the Cu wires are low temperature soldered on the Ni electrodes (13).

quadrants of about 0.9 to 1 nF while the capacitance between any two quadrant electrodes is about 0.5 to 0.6 nF. The resistance between any two electrodes needs to be larger that 500 MΩ. The STM tip is electrically connected with the Low Current Amplifier (LCA) via a 0.15 mm Kapton insulated Cu wire which is shielded with a second wire wrapped around the signal wire and grounded on the STM body. In order to minimize capacitive coupling with the scanner tube wires carrying the High Voltage (HV) signals, its better to place the

tip wire radially from the STM tip to the STM body holding a teflon connector.

The STM piezoscanner tube used was custom built by Staveley [78] and detailed dimensions of it are presented in Appendix A. The tube is made of industry type PZT–4 (Lead Zirconate Titanate) piezoceramic and has a length L = 19.05 mm and an outer diameter of d_{OD} =3.18 mm with a wall thickness t =0.51 mm and Ni electrodes. The ideal vertical sensitivity is defined as the elongation per volt – $\Delta L/V$ of such a tube and can be calculated based on the relation 2.1. The ideal lateral sensitivity is defined as the deflection per volt – $\Delta X/V$ and is approximatively given by the equation 2.2.

$$\frac{\Delta L}{V} = \frac{d_{31} L}{t}, \tag{2.1}$$

$$\frac{\Delta X}{V} = \frac{0.9 d_{31} L^2}{d_m}, \tag{2.2}$$

where $d_m = (d_{OD} - d_{ID})/2$ with d_{ID} being the inside diameter of the tube and d_{31} = -1.27 Å/V at 293 K for PZT–4. For our tube we therefore obtain $\Delta L/V$ = 4.76 nm/V and $\Delta X/V = \Delta Y/V$ = 30.62 nm/V at 293 K. These are only approximative values since they neglect finite effects as nonuniform stiffness at the ends of the tube where it is glued on rigid materials or local depolarization at the places where the Cu wires carrying HV signals had to be soldered. Therefore, corrections needed to be found based on topographic and atomically resolved STM images of known metallic surfaces like Ru(0001) and Au(111). By analyzing multiple STM images images I found that $\Delta L_{STM}/V \approx 0.4 \Delta L/V$ = 2.06 nm/V and $\Delta X_{STM}/V$ = 26.16 nm/V. Since the STM head is well insulated from the sample holder while the sample is cold, the above mentioned STM sensitivities work well in a large range of sample temperatures.

STM coarse positioning motor assembly

The coarse movement of the STM tip is a stick and slip motion of the whole sapphire cylinder–scanner tube assembly done with the four coarse motors mounted in pairs of two at 120° around the vertical axis of the STM head. The third 120° symmetrical position is taken by the St.–St. spring assembly shown in Fig. 2-4, that has the role of pressing the sapphire tube against the four coarse motor pads.

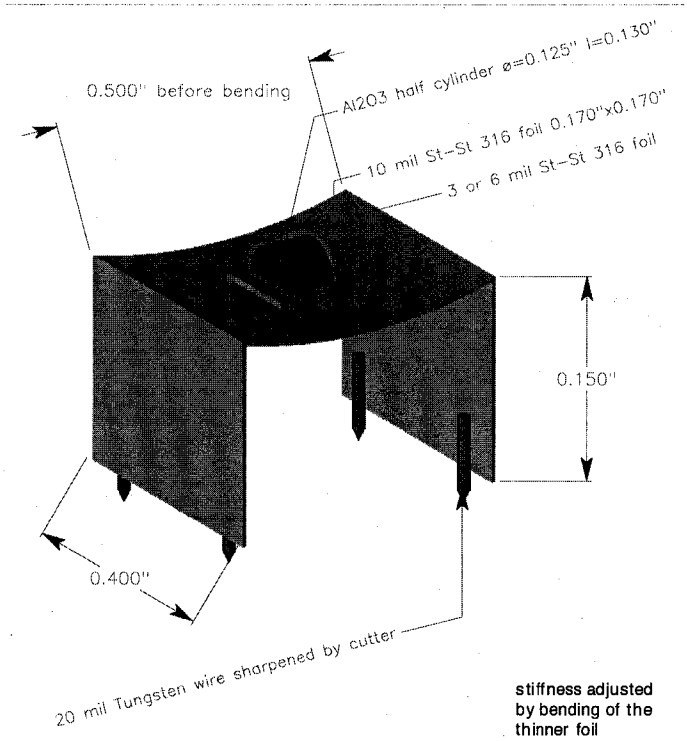

Fig. 2-4: STM spring. It presses against the sapphire tube thus providing the right amount of friction to allow for the stick–and–slip coarse approach motion.

The coarse motors shown in Fig. 2-5 consist of a sandwich of two EBL–1 [78] with Ni electrodes piezoceramic plates that are glued with conductive and low out–gassing epoxy [79] in a right angle geometry of the shear directions. The side of the piezo–stack facing the sapphire cylinder has a semi-cylindrical Al_2O_3 pad glued on it in a right angle orientation

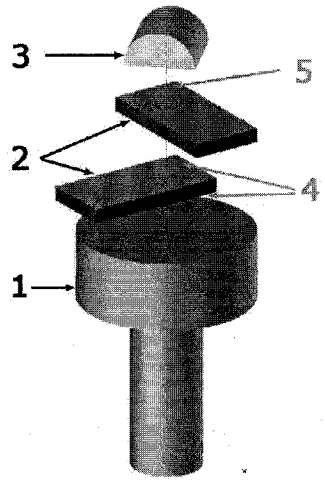

Fig. 2-5: STM piezo–stack coarse motor – axially exploded view: (1) St.–St. 316 flat top screw, (2) piezoceramic plates with Ni electrodes, (3) Al_2O_3 motor pad, (4) areas glued together with UHV compatible conductive epoxy [79] and (5) parts glued with UHV compatible and nonconductive epoxy [80]

with respect to the scanner axis such that it minimizes the contact area between the pad and the sapphire tube. Since electrically conductive epoxy is needed to glue the piezo–plates together to form the piezo–stacks, the gluing procedure is prone to yield short circuits (either by direct electric contact or electron field emission effect conduction while applying coarse HV signals). Care must be taken in applying only a very small amount of epoxy between the plates. I have found that electrical parameters of each individual stack is indicative of how reliable the stack will perform in UHV conditions after repeated bake–out cycles of the UHV chamber. Good piezo–stacks are thus characterized by the larger than 500 MΩ resistance between any two electrodes and by the capacitance between two consecutive electrodes of about 0.5 to 0.6 nF while the top–bottom capacitance is about 0.3 to 0.4 nF. After wiring four piezo–stacks in parallel configuration like in Fig. 2-6, good working coarse motor assembly have the following values of capacitances: C_{0-1} and C_{1-2} are between 1.6 to 1.8 nF, C_{0-2} between 0.8 to 1 nF.

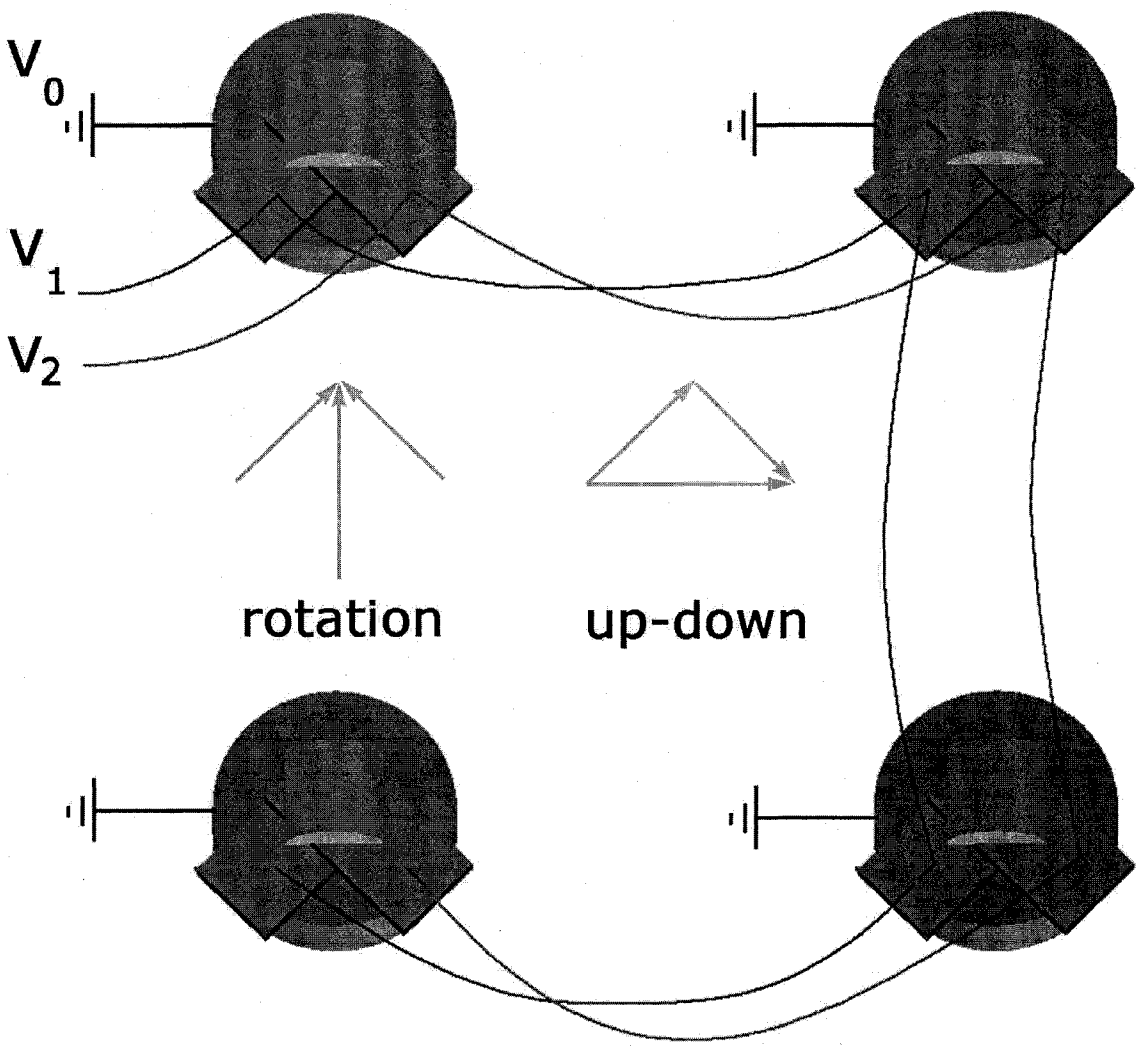

Fig. 2-6: STM coarse motors configuration and operation: four piezo–stacks are mounted in parallel configuration; both up–down and rotation motion of the scanner tube assembly can be obtained by appropriate voltages applied on the stacks. The bottom of the stack (V_0) is always grounded on the STM scanner body.

The four piezo–stacks are wired in a parallel configuration to obtain synchronous operation Fig. 2-6. For a given shear geometry of the piezo–stacks, the shear directions of

the piezoceramic plates are composed vectorial to give up–down or rotational motion of the scanner tube assembly [81, 82] while applying the sawtooth high voltage signals Fig. 2-7 [83]. Thus, for the configuration shown in Fig. 2-6, by applying HV signals between

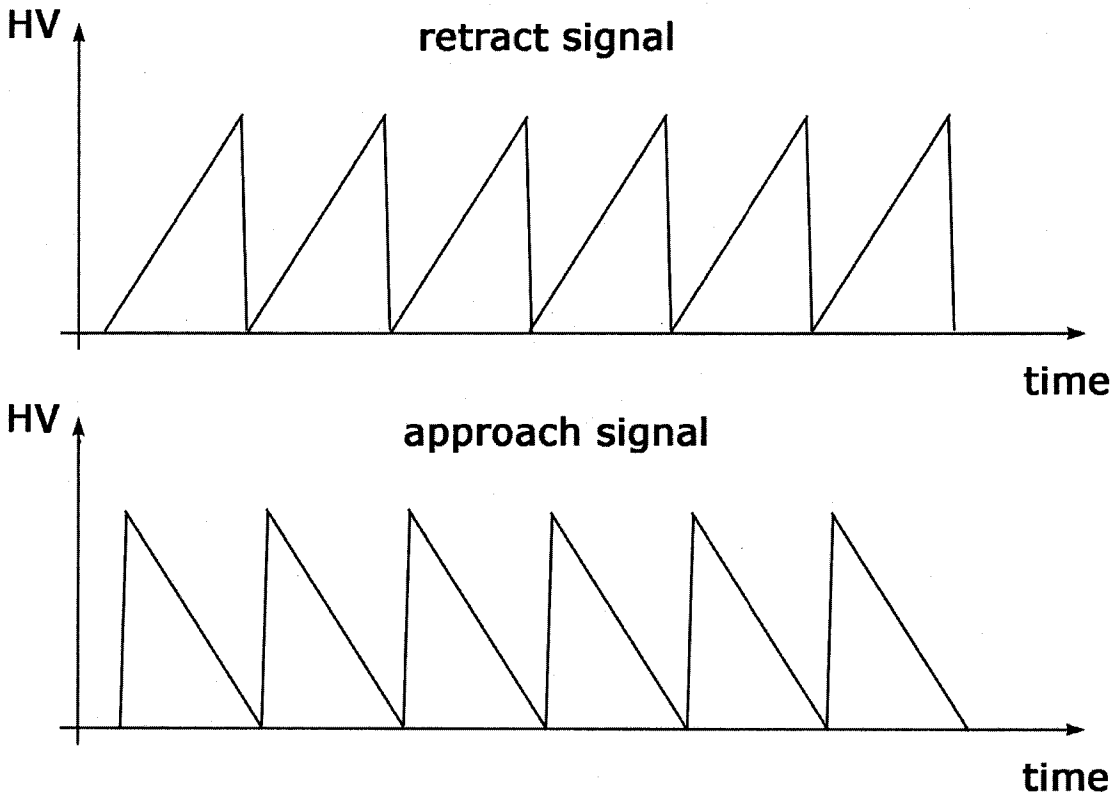

Fig. 2-7: Saw–tooth HV coarse motors signals. The speed of the motors depends on both amplitude and frequency of the signal. For up–down motion, the usable HV coarse signals can have amplitudes between 400 V and 1000 V and frequency ranging from 0.5 kHz and 5 kHz. The rotation motion requires amplitudes from 250 V to 500 V. Higher that 500 V could produce field effect electron conduction across the edge of the piezoceramic plate.

top (V_2) and bottom (V_0) terminals with the middle (V_1) terminal floating, up or down translational motion is obtained. This is the main operation mode for STM tip–sample

approach. For rotational motion of the STM scanner tube, the HV sawtooth signals are applied between the middle terminal (V_1) and the bottom (V_0) and top (V_2) terminals which are both grounded. This last operation mode is useful for investigating larger areas on the sample.

The STM–head rests on the sample holder via three symmetrically bottom placed glass balls in order to decouple thermally and electrically the STM from the sample holder. When the sample holder is kept at 100 K, the temperature of the STM head body thermalizes at about 0° C. The coarse approach speed can be adjusted by both sawtooth signal amplitude and frequency (Fig. 2-7) in a wide range from fractions of mm/min to few mm/min usually yielding about 3 min total STM tip approach time.

Self aligning STM head – sample holder mechanism and goniometer design

In order to be able to reach the same nano–meter size scanning area on the sample, (1) the position of the STM head with respect to the sample holder has to be fixed, and (2) the azimuthal angle of the scanner tube assembly with respect to the STM body has to be controlled. The glass balls on the bottom of the STM fit in a self–aligning system of grooves (Fig. 2-2c) machined on the top of the sample holder fixing the STM body – sample holder position. The rotational degree of freedom of the scanner tube assembly with respect to the STM body is controlled via a goniometer mounted in a window machined in the STM body that monitors the position of a vertical thin mark on the outer surface of the sapphire cylinder as shown in Fig. 2-8b. In terms of linear displacements of the tip with respect to the sample, the goniometer gives a precision of 1–2 μm (Fig. 2-8a), which is few times smaller than the total scanning area of 8 μm $\times$ 8 μm for EBL–1 scanner tube. Finer tuning can be achieved by looking at recognizable features on the sample.

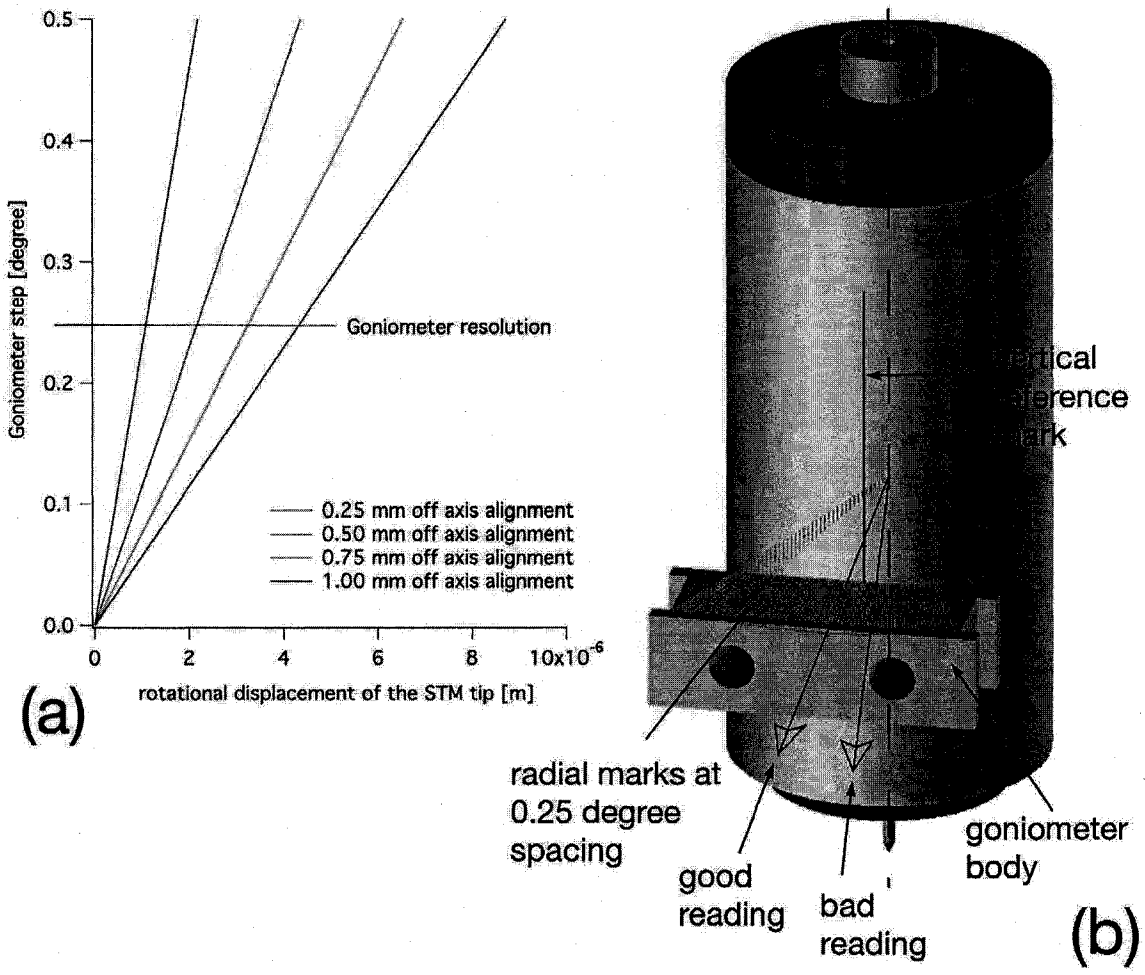

Fig. 2-8: STM goniometer. (a) Rotational displacements of the STM tip as a function of the goniometer step for various off–axis values of the STM tip; the lower off–axis value of 0.25 mm is the upper value obtained from adding the clearances of the machined parts used in the STM head construction while the highest value of 1.00 mm is the chosen maximum value for the worst case scenario when the piezo–tube is glued off-normal on the scanner tube base. (b) 3D on scale rendering of the STM scanner assembly and the goniometer body containing radially oriented marks etched at 0.25 degree interval chosen based on the estimates shown in (a). A good reading of the scanner tube assembly azimuthal position is obtained by choosing a line of sight that goes along the goniometer marking that best aligns with the vertical reference mark on the outer surface of the sapphire tube.

Access to the sample is done by raising the STM head in a vertical translation stage which also serves as a path for the STM wiring. The in vacuum part of wiring of the STM

is done with braided pairs of 0.1 mm Kapton insulated Copper wires in order to minimize mechanical coupling to the chamber.

2.2.3 STM tip preparation

An in situ cleaning and preparation procedure of the STM tips is mandatory if reliable and reproducible STM measurements are to be performed. One of the challenges is the usual lack of tip investigation methods other than STM itself in many UHV chambers. Moreover, since my experiments involve in vacuum sample preparation methods which require the use of various gases for sputtering and reaction–desorption type cleaning, in situ tip preparation became mandatory. I use polycrystalline high purity tungsten etched tips [84]. After air exposure or few sample cleaning and preparation cycles, each tip has to be conditioned in UHV in order to achieve clean, sharp, and stable tips needed for atomically resolved large scale imaging or for fast scanning. The procedure I use consists of initial Ar^+ sputtering under UHV condition which generally yields clean, stable but not very sharp tips followed by self–sputtering in field emission which I found to systematically yield sharp and stable tips. Due to the overall column type arrangement chosen for the STM head – sample holder – cooling assembly, axial sputtering of the STM tip with regular ion guns is not practical. I have therefore chosen to design a small ion source mounted internally in a specially designed sample holder which yields a well collimated ion beam with energies up to 2 keV (Fig. 2-9). During tip sputtering the STM head sits on the ion source, the grooves in the body providing a way to align the STM tip precisely in the ion beam.

This source can operate in two modes, as an energetic ion beam source or electron source, depending on the way accelerating voltages are applied to the electrodes. Fig. 2-10a shows the electrical diagram for the ion source mode while Fig. 2-10b shows the electrical diagram

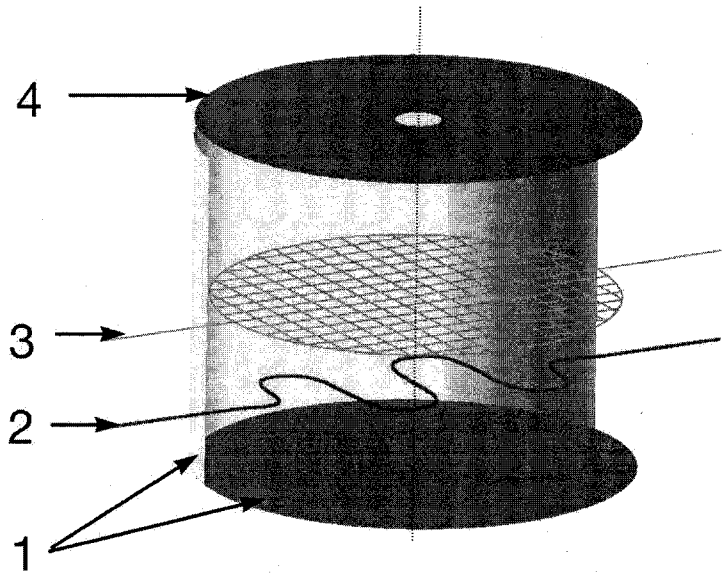

Fig. 2-9: Ion or electron source for STM tip cleaning: (1) high purity (4N5) tantalum cage (repeller) – the side walls have been removed for clarity, (2) 0.05 mm high purity (4N5) tungsten filament, (3) electron accelerating grill made of high purity tungsten, (4) extractor aperture made of high purity tantalum.

for electron beam source operation. In ion beam mode, the optimum settings for STM tip sputtering are: I_f = 1.0 A, V_r = +40 V, V_g = 100 V to 500 V. I found that 500 eV Ar^+ beam at a current density of 20–30 nA/mm^2 yields systematically clean polycrystalline W STM tips after few minutes of sputtering at an Ar partial pressure of about 5×10^{-7} Torr. The second part of the conditioning method involves tip self–sputtering in field emission conditions. A good recipe is to apply up to 700 V between the tip and a polycrystalline Ta foil while the distance between them is adjusted such that a field emission current of 150 to 200 nA is achieved. A short sputtering of 1 to 2 min at a partial pressure of 1 $\times$ 10^{-7} Torr Ar is then sufficient to sharpen the tip while maintaining it clean. A STM tip is usually considered ready for STM experiments when stable, few nA field emission currents are obtained at bias voltages of about 100 V. Electron bombardment was also used

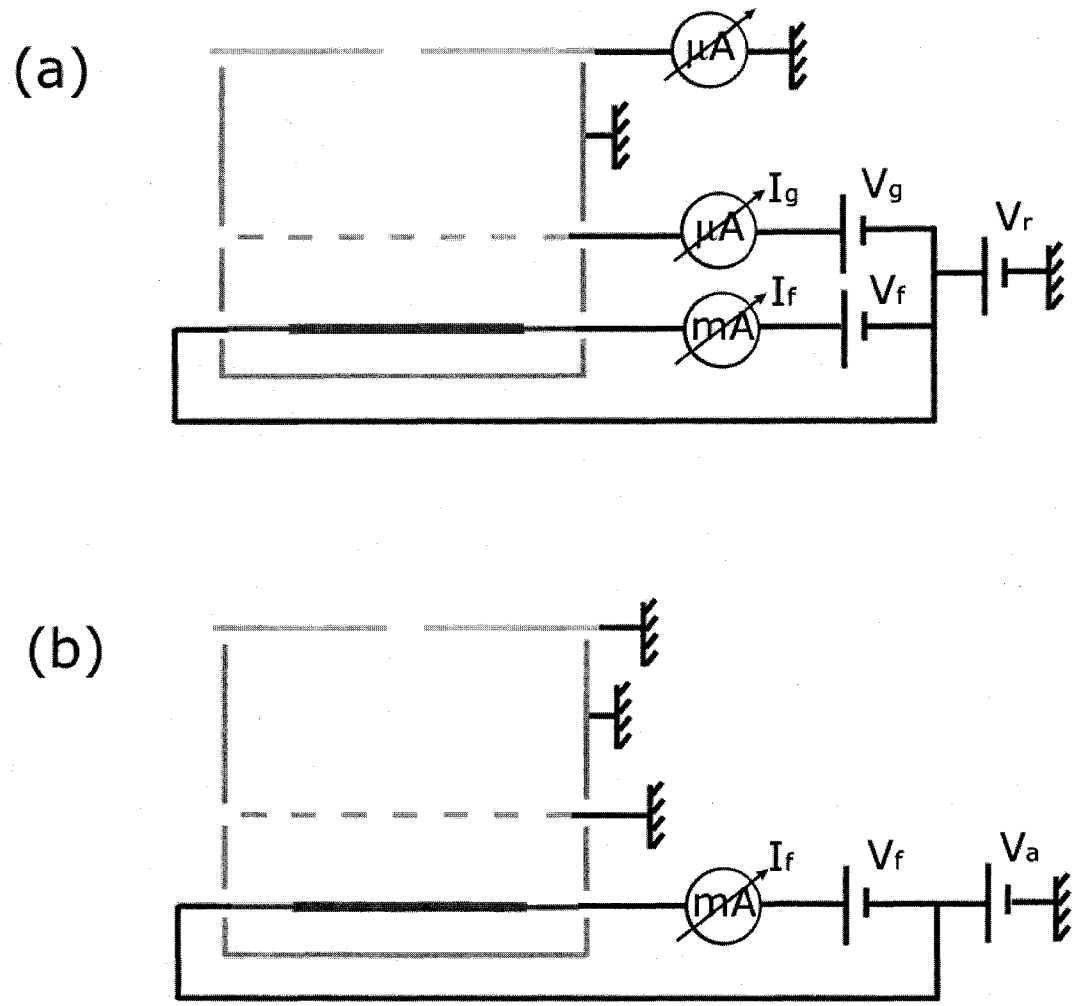

Fig. 2-10: Electrical HV connections for ion beam or electron beam source: (a) for the ion beam operation, and (b) for the electron beam operation mode. V_r is the repeller voltage, I_f and V_f are the filament current and voltage, V_g and I_g are grid HV and current, and V_a is the accelerating electron voltage.

to flash anneal the STM tip for 1 s to 2 s. This method is useful when the STM tip is unstable following a recent Ar^+ sputtering cycle. For electron beam operation mode, good parameters are I_f = 1.0 A and V_a = 100 V to 150 V. Longer annealing time or higher electron energy yielded stable but dull STM tips, probably because local melting of the tip

apex took place.

2.2.4 The UHV system

The sample holder resting on the cold reservoir is mounted by the way of the vibration isolation stage on the UHV chamber. The chamber is also equipped with a linear motion manipulator which allows one to move the sample to different positions in front of various instruments for preparation and characterization, ion gun, gas doser, various metal evaporators, low energy electron diffraction, Auger electron spectroscopy and scanning tunneling microscope position. The chamber also has a load-lock mechanism for sample exchange and pre-cleaning before introduction in the UHV chamber and a garage stage. The chamber is mounted on a rigid rectangular steel frame which rests directly on the floor via 1 inch rubber dampers. Due to the excellent damping performance of the in–vacuum damping stage, the need for air–spring legs, which we considered as an initial option, is not needed. The UHV system is equipped with a 480 l/s ion pump, a titanium sublimation pump (TSP), and a 400 l/s turbopump. Even if the STM is able to achieve atomic resolution with the turbopump running, for best resolution during STM operation the turbopump can be turned off after the gate valve is closed and the system is being pumped only with the Ion/TSP pump. The roughing pumps have been placed in a nearby room in order to minimize acoustic noise.

2.3 Experimental results

The instrument performance was observed on various compact metallic surfaces and atomically flat thin films grown onto them. Initial measurements were done on a single crystal (111) surface of Au, followed by extensive variable temperature studies on the (0001) surface of Ru and strained monolayer thick Ag films grown on Ru(0001) [85]. Atomically resolved

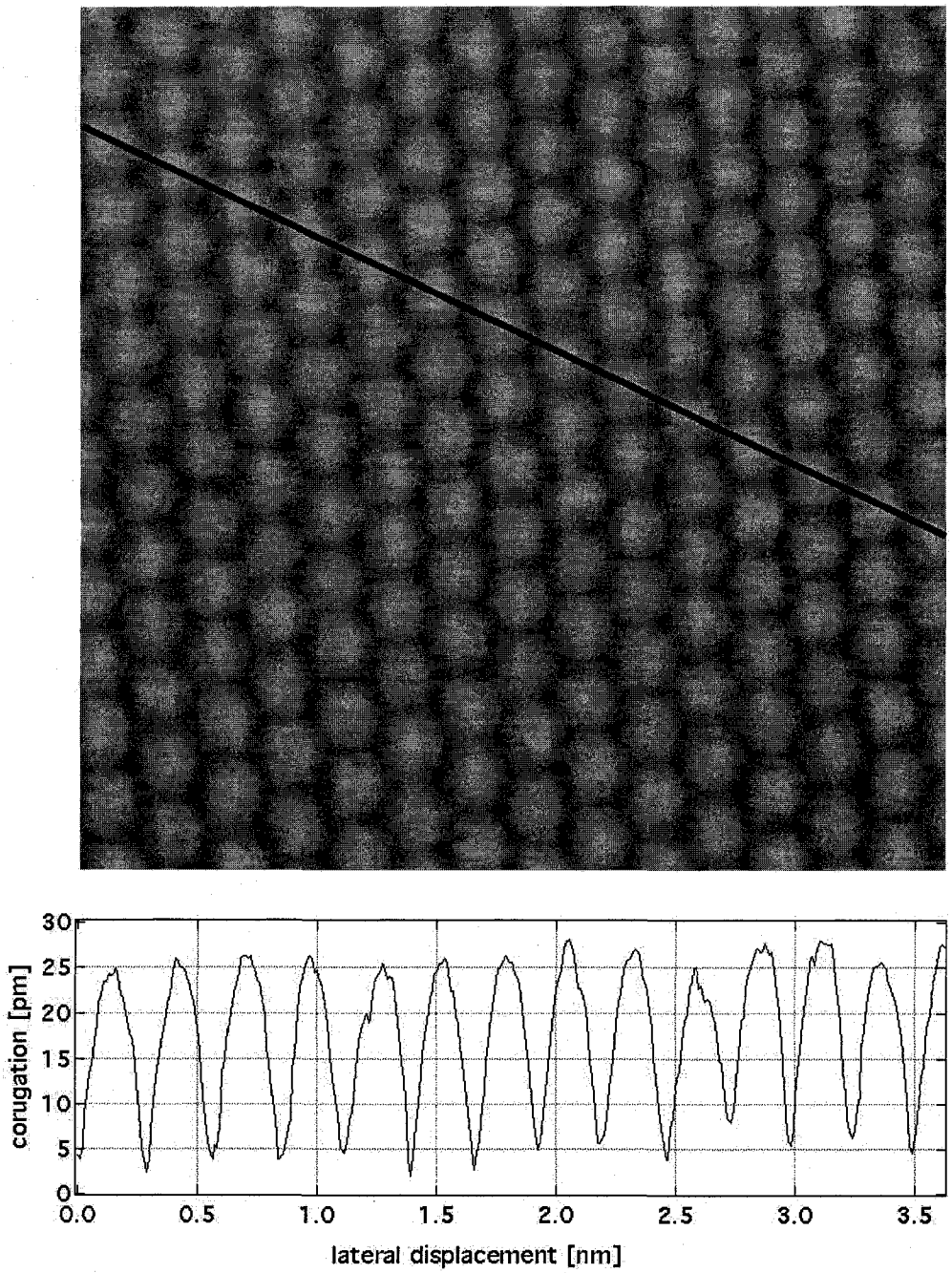

Fig. 2-11: Constant current image of Ru(0001) at 295 K (-10 mV sample bias, 6.6 nA tunneling current, and 33 Å scan range) and the line scan profile of the line marked on the image showing the apparent corrugation.

terraces and surface atomic steps of Ru(0001) have been used for instrument calibration and testing of the noise level. The Au(111) and one atomic layer thick Ag films on Ru(0001) have been used to test the ability of large scale atomically resolved imaging and fast STM imaging [85].

The surfaces of compact metallic interfaces due to their low corrugation can be used as test–systems for the STM's performance. In Fig. 2-11 we show a high resolution constant current image of Ru(0001) at 295 K and a line scan profile of the line marked in the image. The vertical resolution is about 2 pm peak to peak. Fig. 2-12 shows a high resolution constant current image of 1 atomic layer thick Ag film grown onto Ru(0001) at 110 K. The line profile shows a vertical resolution better than 2 pm peak to peak. Such values of the vertical resolution of the instrument are consistent with the electrical noise level of the piezodrive's HV amplifiers for the sensitivity of the scanner tube used at room temperature. Consistently, this noise level is attainable on all other measured surfaces at low and room temperatures since the STM head temperature is relatively independent on the sample temperature.

Strained metallic interfaces can form misfit dislocation networks with units cell sizes in the range of tens to hundreds of Ångstroms [29, 28]. Detailed analysis of such structures requires one to image with atomic resolution on the scale of the reconstruction. More important, the analysis of networks of misfit dislocation networks needs even larger scale imaging with atomic resolution. One of the goals of this instrument is to achieve such performance. I was able to investigate the misfit dislocation network of Au(111), the short herringbone (SHB) reconstruction and large herringbone reconstruction (LHB) of one atomic thick layer of Ag on Ru(0001) [49], and 2ML Ag / Ru(0001) [34] on the scale of few unit cell sizes. Fig. 2-13a shows the SHB network of Ag / Ru(0001) at 330 K and Fig. 2-13b shows the LHB

network at 280 K respectively.

The dynamical performance of this STM design is exemplified by the images in Fig. 2-14 which follow the time dependence of the positions of two threading dislocation cores like the ones seen in Fig. 2-13b. Each image is about 90 Å × 90 Å and were acquired in about 3 s. The vibrations of the threading dislocation cores is clearly resolved at the darker, linear regions which show changing positions from one scan line to the next.

2.4 Discussion

I have designed and constructed a variable temperature STM for large scale imaging which operates between 80 K and 700 K. Tests have shown that the instrument routinely achieves large scale, high resolution, and fast–scanning imaging of compact metallic surfaces. The vertical resolution of the STM is better than 2 pm and it is mostly due to the HV amplifier noise and the high sensitivity of the piezotube which was needed in order to achieve large scale imaging. This resolution compares very well with other systems, for example the lowest vertical resolutions reported of 1 pm are attainable with low temperature STM systems running around liquid Helium temperature (4 K) and below. Compared with those systems, the instrument I just presented has about 16 times the scanning range parallel to the surface. The in–vacuum vibration isolation system works very well such that no external vibration isolation is required. Also, turbopump vibrations are reasonable attenuated by the vibration isolation system. Along with the flange–on design, the in–vacuum only vibration isolation system will allow for the STM to be attached on a large variety of surface science chambers were other complementary investigation tools are available. The high–scanning speed of the STM head will allow with the use of a high speed STM electronics for even faster frame rate, potentially bringing it down by another order of magnitude thus higher

temporal resolutions could be achieved.

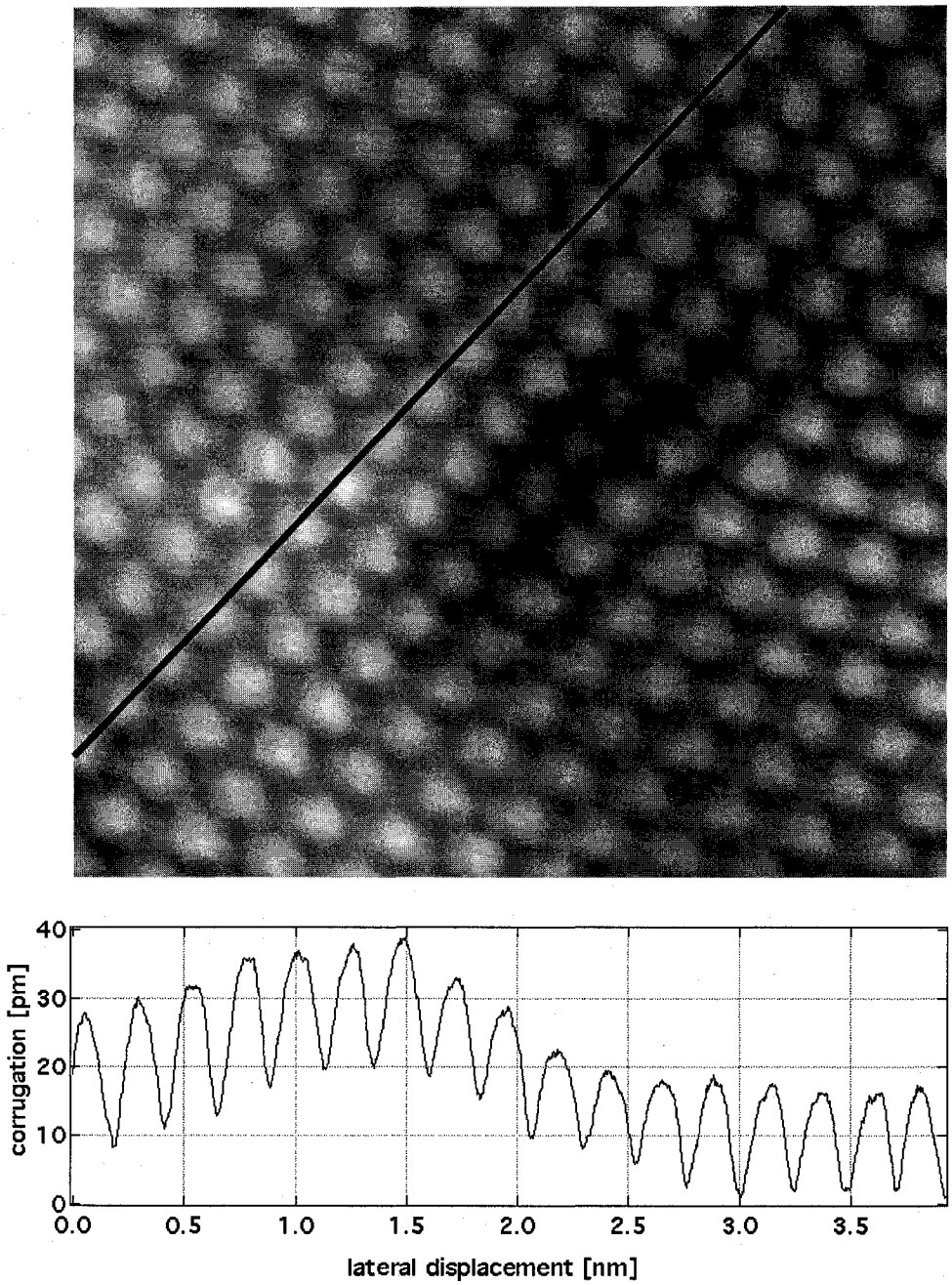

Fig. 2-12: Constant current image of the short herring bone reconstruction of one atomic layer Ag on Ru(0001) at 110 K (-30 mV sample bias, 6.7 nA tunneling current, and 33 Å scan range) and the line scan profile of the line marked on the image showing the apparent corrugation. The long range vertical modulation of the Ag film is due to the strain relaxation of the misfit dislocation network.

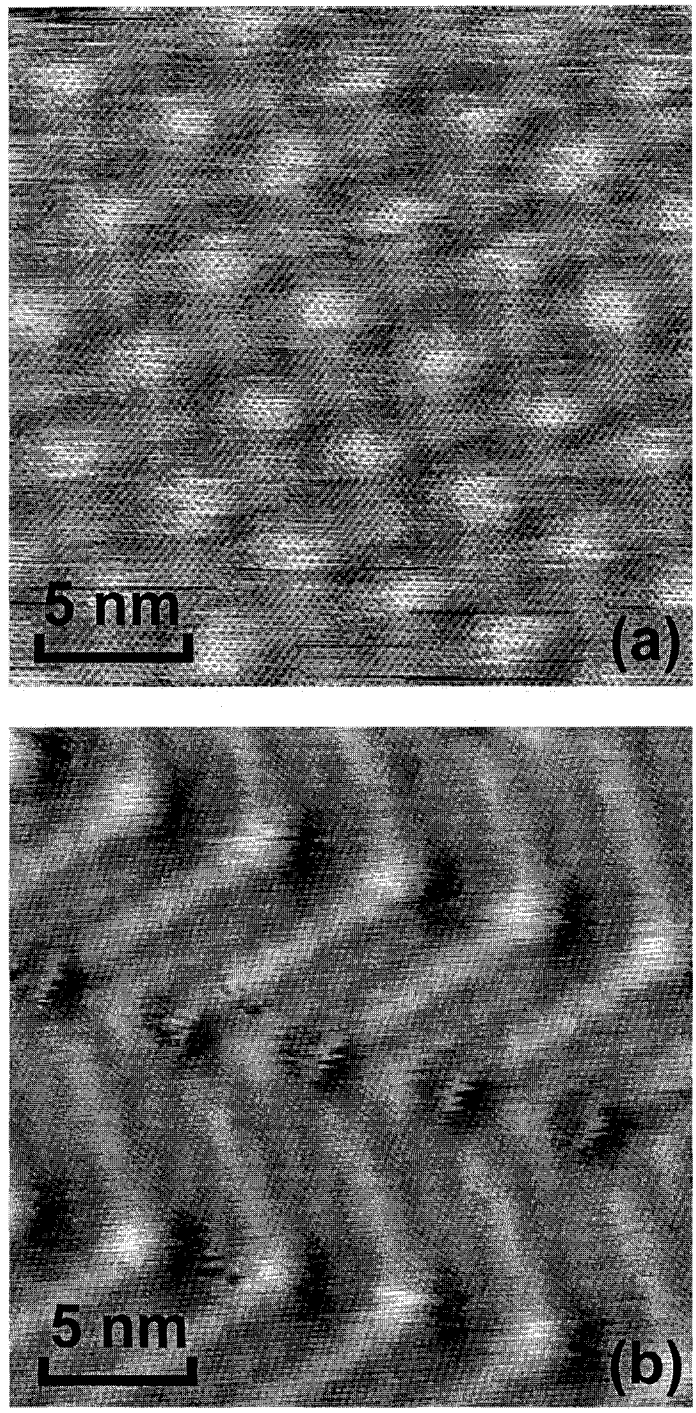

Fig. 2-13: Constant current image of 1 atomic layer thick Ag film on Ru(0001): (a) Short Herring Bone reconstruction at 330 K (-20 mV sample bias, 4.6 nA, and the overall Ag coverage is lower than 1ML normalized to Ru(0001) substrate); (b) Long Herring Bone reconstruction at 280 K (-170 mV sample bias, 19.7 nA, and the overall Ag coverage is larger than 1 ML normalized to Ru(0001) substrate).

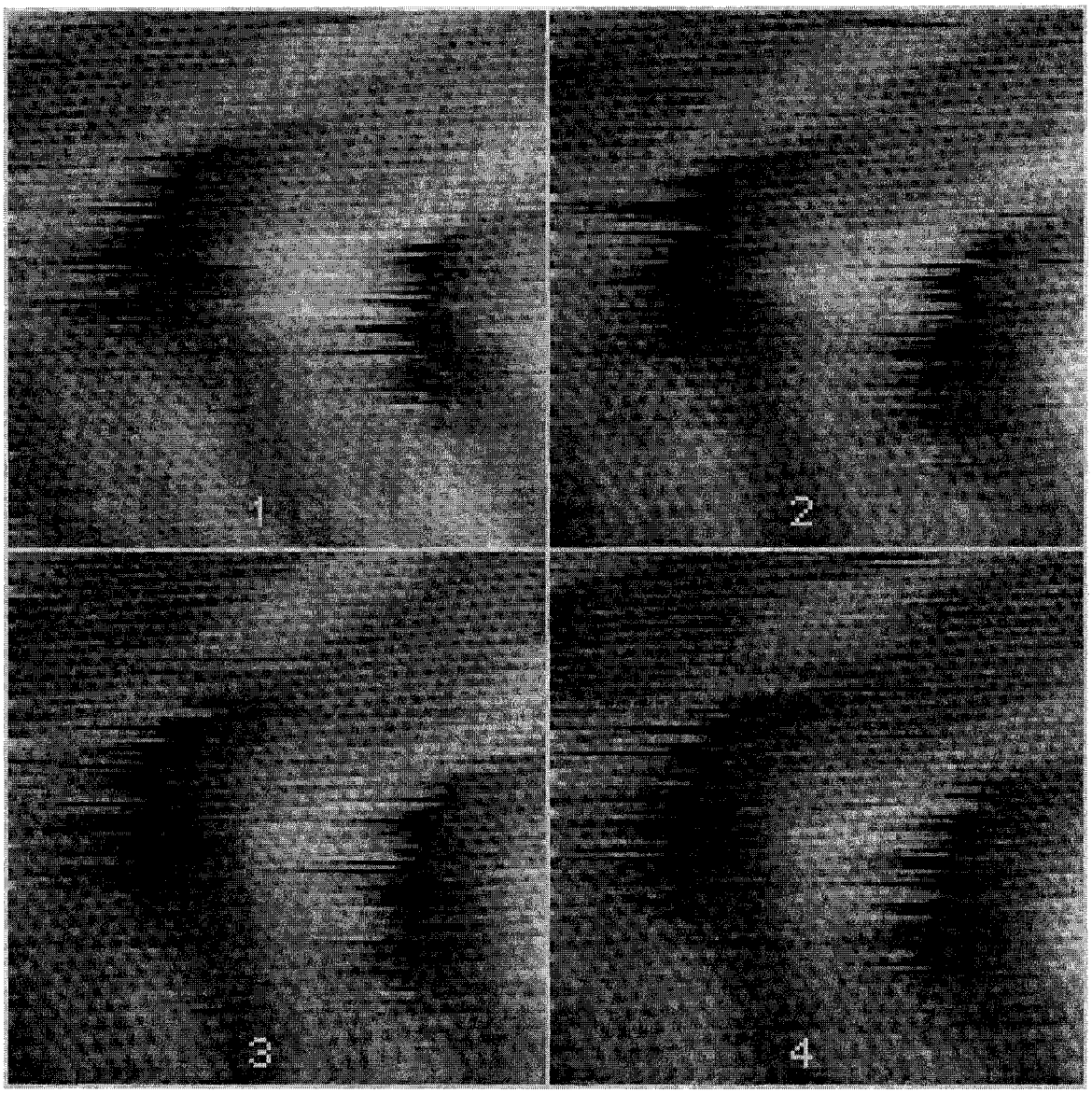

Fig. 2-14: Consecutive constant current images of one pair of threading dislocation cores of the long herring bone reconstruction of 1 atomic layer thick Ag film on Ru(0001) at 280 K (-170 mV sample bias, 19.6 nA). Scanning time for each image is 3 s.

Chapter 3

Self-Organized Nanotemplating on Metallic Misfit Dislocation Networks

3.1 Introduction

Ultra-thin metal films have been observed to form ordered arrays of dislocation structures to relieve the strain caused by the different lateral lattice spacing of the adsorbate film and substrate [29, 28, 49]. Such ordered misfit dislocation networks are particularly interesting as templates for self-assembly of arrays of nano-clusters [27, 30, 33] with novel properties. It is expected that these structures find application in higher density magnetic storage, more selective catalysis and higher sensitivity biochemical sensors, and, perhaps, quantum computing and photonics. However, the controlled fabrication of such nano-arrays with reproducible properties is a serious challenge, and surface science has to play a key role in the understanding of their formation and their characterization. The complexity of the problem resides in the large number of atoms involved in such reconstructions, unit cell sizes of the strained two–dimensional networks often containing a few hundreds to thousands of atoms. In order to understand these self-assembly processes, very large scale, atomically

resolved and variable temperature scanning tunneling microscopy (VT–STM) data need be linked via atomistic models with first–principles information about the system. I have therefore designed and home–built a VT–STM instrument capable of large scale, high speed, variable temperature atomically resolved STM imaging of compact metal surfaces [86]. The great potential of this template approach in strained thin films is that the feature sizes and symmetry are believed to be tunable by controlling the misfit [44, 45]. This can be achieved e.g. by adjusting the misfit between the ultra-thin film and substrate, or by controlling the coverage or temperature. Also, the chemistry of the adsorbates on these strained metallic interfaces can strongly affect the final equilibrium state of the multi-component systems.

3.2 2D misfit dislocation networks

In general, growth of a thin film on a dissimilar substrate results in a strained interface due to the lattice mismatch between the two materials. Strain is often partially relieved through the formation of well-ordered networks of misfit dislocations [29].

3.2.1 Au(111) misfit dislocation network; basic elements

The herringbone reconstruction of Au(111) is an example how an ordered misfit dislocation network can also form on a clean surface. Cleaving a Au crystal along the (111) crystallographic plane should leave a FCC terminated surface. Experimental observations [28] have shown, however, that terminating a Au crystal in a (111) surface leaves the top layer in compression by 4% with respect to the layers below due to the accommodation of additional Au atoms, resulting in three possible 120° rotated domains of a zig-zag like reconstruction pattern shown in Fig. 3-1a [46, 47]. The basic elements of such a system are: (i) Shockley partial dislocations consisting of Au atoms sitting on bridge sites along one of the threefold

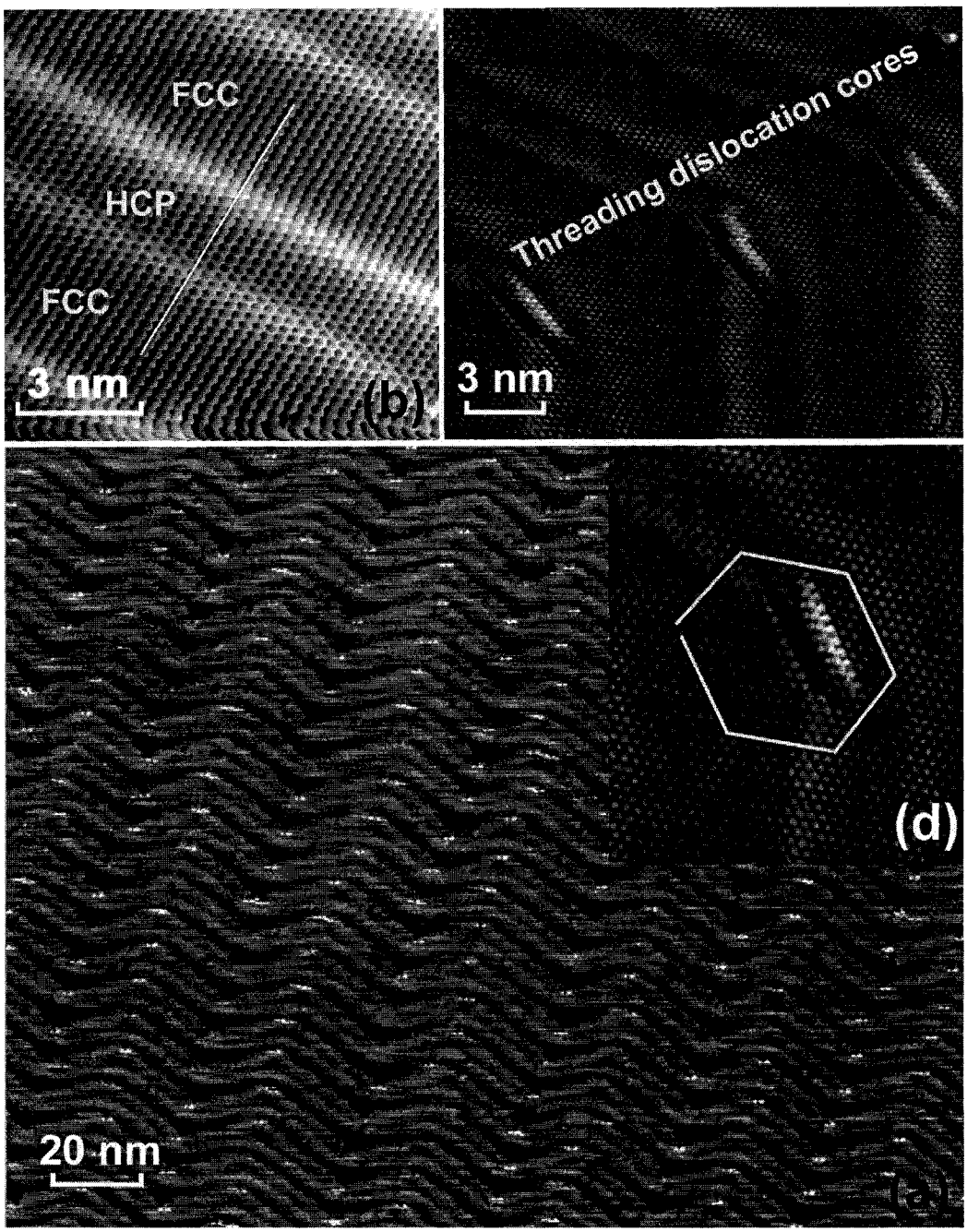

Fig. 3-1: Constant current image of Au(111): (a) large scale misfit dislocation network; (b) inset showing atomically resolved Shockley partial dislocations as bright stripes with alternated FCC-HCP-FCC areas bounded by atoms sitting on the bridge sites along $[11\bar{2}]$ direction; the white straight line show how the stacking of the Au atoms changes as passing across the Shockley partials; (c) threading dislocations cores formed where two Shockley partial dislocations meet, (d) Burgers circuit around a threading dislocation core showing 1 extra row of atoms.

symmetric $\sqrt{3}$, or $[11\bar{2}]$, directions, at the boundary of consecutive FCC and HCP stacking of the top layer Au atoms (Fig. 3-1b), and (ii) threading dislocations formed at the meeting point of two Shockley partial dislocations shown in Fig. 3-11c. The top Au atomic layer is in registry with the substrate in the $\sqrt{3}$ direction while it is compressed along the closed-packed directions where 23 Au atoms sit on top of 22 Au atoms of the substrate. The hexagonal symmetry of the nearest neighbors is maintained everywhere with the exception of the threading dislocation core sites, seen in Fig. 3-1d as the bright rows of atoms at the elbow sites, where a Burgers vector circuit shows the existence of an extra row of atoms. The rectangular unit cell size of the reconstruction is about 8.5 nm $\times$ 35 nm.

The only other known clean metal surface to reconstruct in a misfit dislocation network is the (111) surface of platinum, which exhibits a similar reconstruction [48]. Both these surfaces exhibit the reconstruction due to the misfit of the lattice spacing in the thin film and bulk substrate. Many semiconductor surfaces also reconstruct at room temperature; however, the presence of dangling bonds at the surface makes these systems chemically and structurally less stable.

3.2.2 Misfit dislocation networks of 1 ML Ag/Ru(0001)

The size and symmetry of the dislocation networks on single crystal metal surfaces cannot be altered. For viable template solutions we have to focus on systems where we can engineer unique dislocation networks, i.e. thin film interfaces of dissimilar materials with adjustable strain caused by lattice mismatch, coverage, and temperature.

An excellent model system to test the effect of the coverage and temperature on the misfit dislocation network is monolayer–thick Ag films on Ru(0001) [49, 87]. In contrast to the Au(111) misfit dislocation network, for a one atomic layer thick Ag film on Ru(0001)

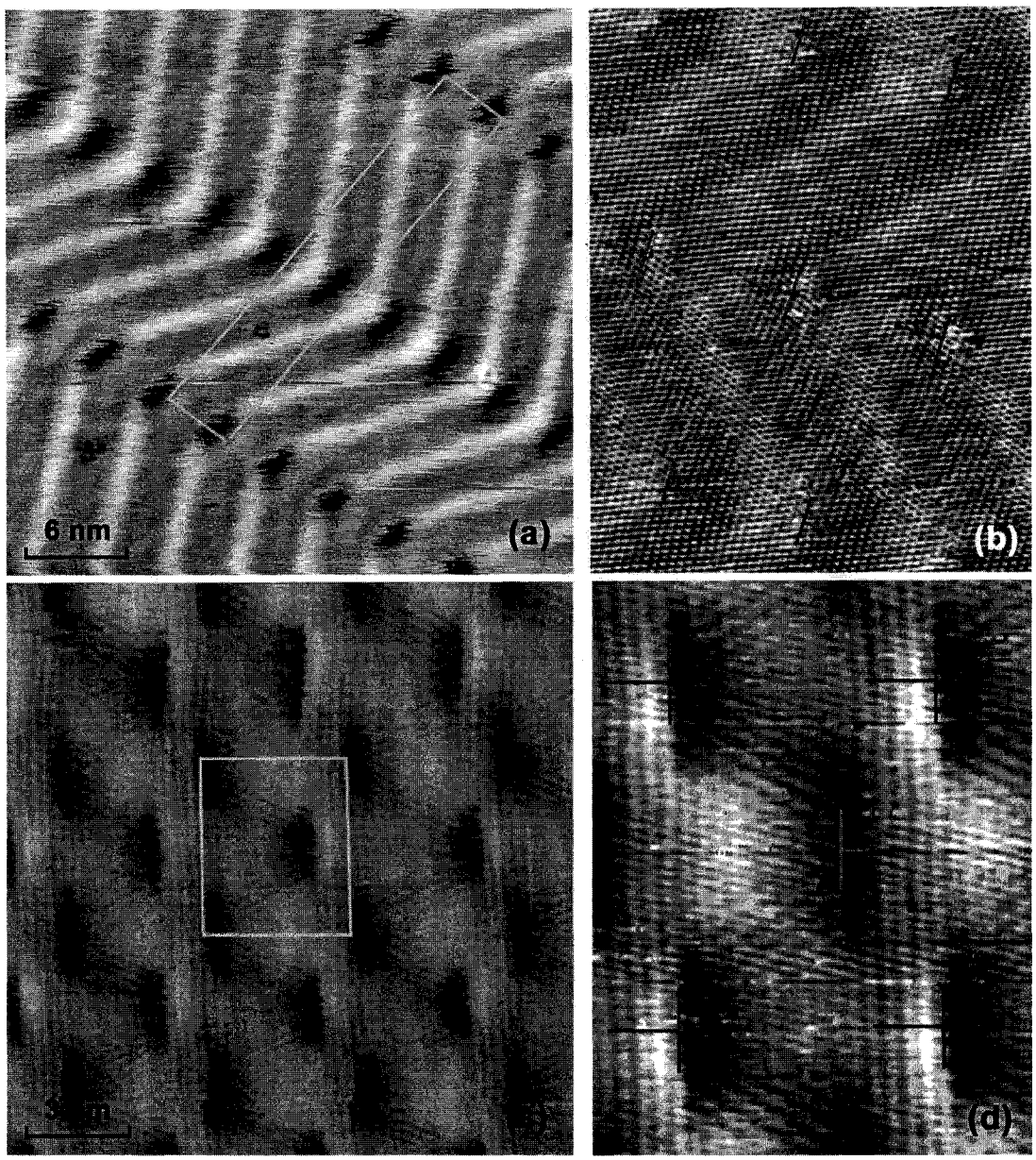

Fig. 3-2: Constant current STM images of the reconstructions of 1 atomic layer Ag film on Ru(0001): (a) large herringbone (LHB) network at 295 K and overall Ag coverage larger than 1 ML normalized to Ru(0001) substrate; (b) inset showing atomically resolved LHB – Shockley partial dislocations are running between consecutive, alternate orientations of the treading dislocation cores which are marked by red T's; (c) short herringbone (SHB) network at 110 K and overall Ag coverage less than 1 ML; (d) atomically resolved inset of the unit cell of the SHB network from (c).

the Ag adlayer is expanded relative to the surface layer of Ru(0001) due to a lower atom density in the Ag layer than in the Ru(0001) plane. The lattice spacing of bulk Ag is

about 7% larger than that of bulk Ru. For a coverage slightly larger than 1 ML, the misfit dislocation of one atomic layer thick Ag films on Ru(0001) has a unit cell size of $a' \times c' =$ 68(70) $\times$ 16(17) Ag atoms called long herringbone (LHB), shown in Fig. 3-2a and Fig. 3-2b, where the Shockley partial dislocations are running along $\sqrt{3}$ directions like in the case of Au(111).

At a coverage less than 1 monolayer, because the overall Ag film density is lower than for more than 1 ML – more space for Ag to relax, Ag films on Ru(0001) reconstruction changes into a misfit dislocation network with a unit cell size of 18(19)$\times$15(16) Ag atoms called short herringbone (SHB) as shown in STM data in Fig. 3-2c and Fig. 3-2d. The dislocation structure of SHB and LHB reconstructions is similar, with a rectangular unit cell but different lengths of Shockley partial dislocations running between threading dislocation cores. The LHB structure formed for 1.x ML Ag coverage is not stable at high temperatures. As the temperature is increased above 480 K, LHB transforms into SHB reconstruction [87]. The transition is reversible.

Misfit dislocation networks can be understood in the framework of a 2D Frenkel–Kontorova model [36, 37, 88, 89, 90], where one has to consider the potential landscape of the surface seen by an adatom and the inter–adatom potential. The interactions within the adsorbate film and with the surface is described by the hamiltonian

$$H = U_{sub} + U_{Ag-Ag} + KE. \tag{3.1}$$

If we neglect the kinetic energy term KE we have

$$H_{FK} = \sum_{\vec{r_i}} \sum_{\vec{g}} V_{\vec{g}} e^{i\vec{g}\cdot\vec{r_i}} + \frac{k}{2} \sum_{\vec{r_i}} \sum_{\vec{r_j} \neq \vec{r_i}} (|\vec{r_i} - \vec{r_j}| - b\, a_{Ru})^2, \tag{3.2}$$

where k is the elastic constant of the Ag film and $b = a_{Ag}/a_{Ru}$ is the lattice mismatch. This hamiltonian can be solved for appropriate boundary conditions and density of the adsorbate

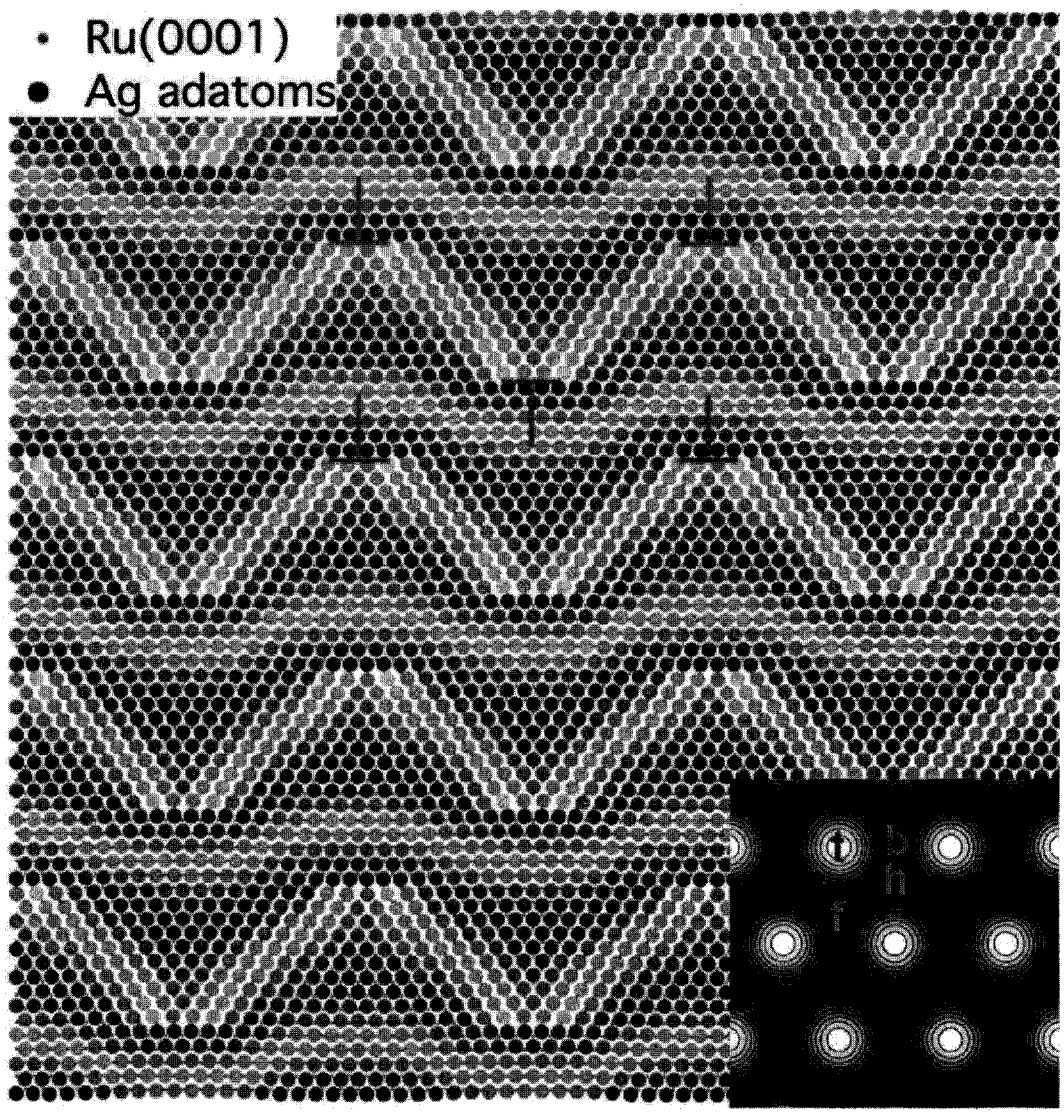

Fig. 3-3: 2D Frenkel-Kontorova model of the misfit dislocation network of < 1 ML Ag/Ru(0001), the short herringbone (SHB) structure; the inset shows the surface potential obtained from the first principles results of the binding energies of Ag on Ru(0001) at the high symmetry points: $E_t = 282$ meV (top), $E_b = 55$ meV (bridge), and $E_h = E_f = 0$ (HCP and FCC sites). Ag–Ag interaction parameters are the elastic constant of the Ag film, $k = 2000$ meV/Å^2 and the lattice mismatch $b = a_{Ag}/a_{Ru} = 1.14$. The gray level is proportional to the surface potential at the location of each Ag atom, and thus indicates its relative height.

layer to obtain the ground state solution. The result of such a simulation is shown in Fig. 3-3, which closely describes the low temperature STM measurement in Fig. 3-2c. The substrate potential landscape shown in the inset of Fig. 3-3 is obtained by symmetry arguments from

the binding energies of a Ag atom on high symmetry sites of Ru(0001), from first–principle calculations [91].

3.2.3 Misfit dislocation networks of 2 ML Ag/Ru(0001)

We have seen how coverage and temperature can change the size of the unit cell of the misfit dislocation network for the case of 1 atomic layer thick Ag films on Ru(0001) while the rectangular symmetry of the unit cell of the reconstruction was maintained. In the case of 2 atomic layer thick Ag films on Ru(0001) the reconstruction is having a trigonal symmetry shown by the STM image in Fig. 3-4. The unit cell of the reconstruction runs between the centers of neighboring trigons in the $\sqrt{3}$ directions. The unit cell size is about $13\sqrt{3}$ nearest neighbor distances of the Ag layer. A key feature is the absence of threading dislocations on the top layer, the darker, linear regions in the STM images corresponding to vertical displacements at the threading dislocations in the first Ag layer. Thus the strain is accommodated in the first Ag layer [34] .

3.3 Growth mechanisms of 2D nano–cluster arrays on misfit dislocation networks

The availability of three parameters – lattice misfit, coverage and temperature – in controlling the misfit dislocation network symmetry and characteristic size creates opportunities for the growth of two dimensional arrays of clusters with various specific sizes, from few nanometers to few tens of nanometers, onto such strained surfaces. The misfit dislocation network can play a passive role as in the case of adsorbates nucleating at specific sites or regions without changing its structure, or they can actively interact with the adsorbates, thus generating a completely new symmetry and periodicity of the multi phase system. In

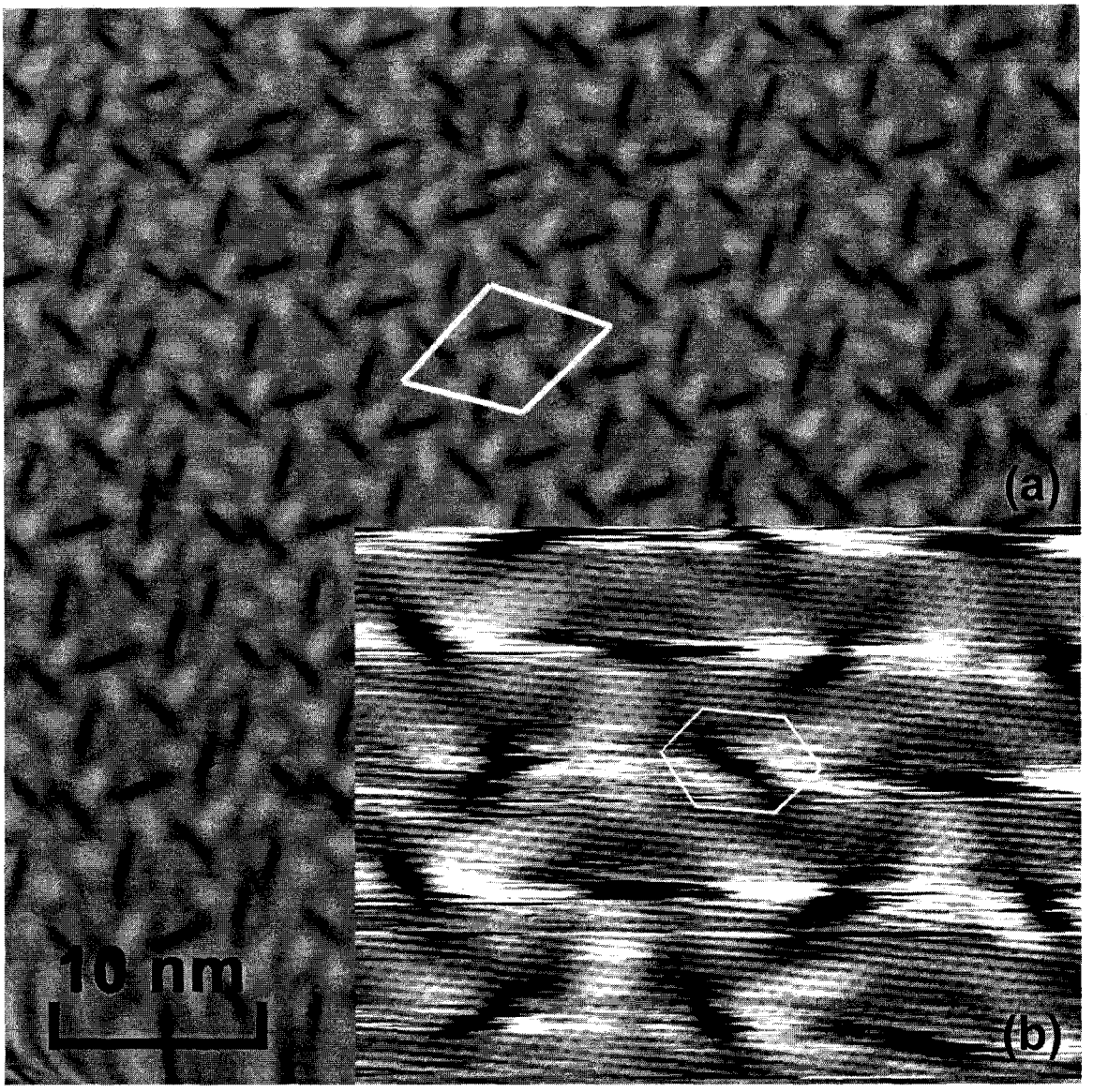

Fig. 3-4: Constant current STM images of the trigon reconstruction of 2 atomic layer Ag/Ru(0001): (a) large scale image with the primitive unit cell of the superstructure marked with white lines; (b) atomically resolved image showing that the symmetry of the top layer is hexagonal everywhere. The closed Burgers vector circuit shows no threading dislocation is present at the darker regions.

the following I will show how different growth processes can lead to diverse 2D cluster–array sizes and symmetries.

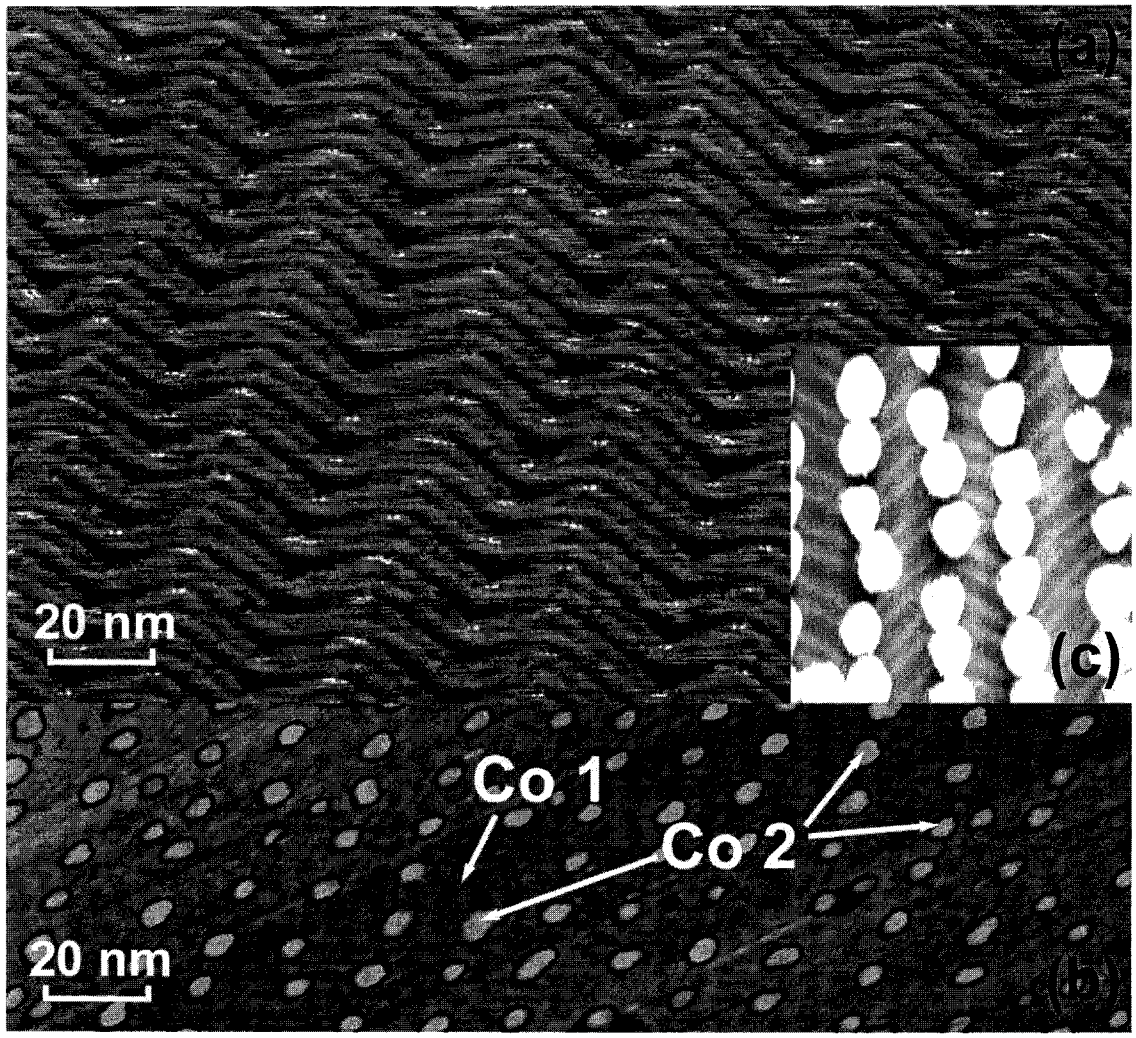

Fig. 3-5: Selective adsorbtion of Co on Au(111): (a) misfit dislocation network of Au(111). (b) Co clusters grown on Au(111); Co nucleates mostly in 2 atomic layer thick clusters of few tens of atoms at the threading dislocation sites of Au(111), Co 2, with some clusters being only one atomic layer high, Co 1; (c) enhanced contrast showing the location of the nucleation of Co clusters at the threading dislocation cores; Au(111) is unaffected by Co, as seen by the existence of the Shockley partial dislocations. All STM data taken at 295 K.

3.3.1 Nucleation of ad-clusters at the threading dislocation cores

An example for the passive role of the misfit dislocation network in the growth process of the adsorbates is Co cluster growth on Au(111) [92, 93]. In this case, Au(111) serves as a template on which Co atoms nucleate at the threading dislocation sites, leaving the

reconstructed surface of Au(111) relatively undistorted as seen by the existence of Shockley partial dislocations in Fig. 3-5c. The symmetry and Co cluster spacing is thus following the symmetry and characteristic length scale of the substrate as seen in Fig. 3-5a and Fig. 3-5b. Most Co clusters have been observed to grow two atomic layers high and are seen as yellow clusters in Fig. 3-5b. One atomic layer height clusters are growing between them if Co coverage becomes higher than about 0.2 ML. Similar growth modes have also been observed for Fe [94] and Ni [95, 96], Mo and Ru adsorbed on Au(111).

3.3.2 Adsorbate induced strain relaxation of misfit dislocation networks

Deposition of molecular sulfur from an electrochemical cell [97] onto LHB and SHB reconstructed surfaces of Ag/Ru(0001) at room temperature generates a well–ordered array of sulfur filled Ag vacancies islands [35, 36, 37]. The three–component system composed of S, 1 atomic layer Ag and Ru(0001) forms a well ordered two-dimensional array of uniformly spaced S clusters embedded into the Ag film as shown in Fig. 3-6. The cluster array shows a triangular lattice with an average distance between clusters of about 4.5 nm.

I performed detailed STM studies of the growth process as a function of S coverage for SHB of Ag/Ru(0001) and found a two stage process. At low S coverage, individual vacancies with a fixed size are formed, their density increases proportionally with the sulfur coverage until an almost complete array of vacancies is formed. After S coverage exceeds the threshold values of $\sim$18 mML, the S-filled vacancy islands start growing in size. An intriguing aspect is that saturation density of the Ag vacancy islands is exactly 1/2 of the surface density of the threading dislocation of SHB of Ag/Ru(0001). Another key finding is the restructuring of the Ag film occurring after the S etching process: (i) a change of the symmetry of the unit cell size and (ii) the absence of threading dislocations (TD) in the

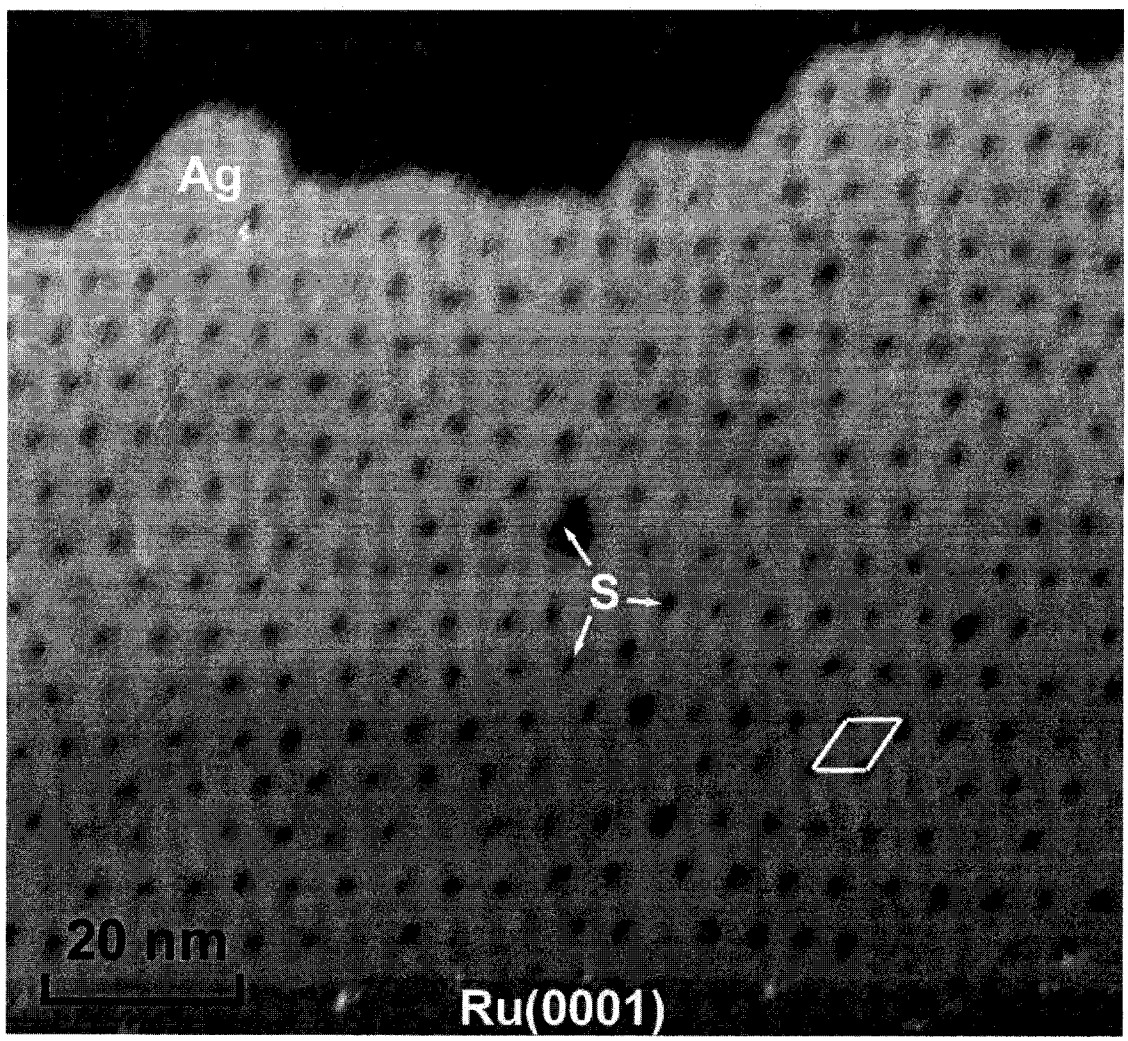

Fig. 3-6: S etching induced restructuring of the 1 atomic layer of Ag/Ru(0001). A new triangular symmetry of the superstructure is formed with S-filled vacancy islands 50 Å apart.

Ag film shown by the absence of a non zero Burgers vector (Fig. 3-7). Inside a unit cell there are two equivalent positions that can be occupied by the Ag vacancy island, the blue and yellow dots marked in Fig. 3-8, thus two hexagonal equivalent lattices can be formed following the S etching restructuring process. Such a mechanism naturally generates the new symmetry and also explains the other experimental observations: (i) the conservation of the unit cell area of 21.4 nm^2 for Ag/Ru(0001) vs. 21.6 nm^2 for S/Ag/Ru(0001), and (ii) the 2 to 1 ratio of TD's and Ag vacancies [98].

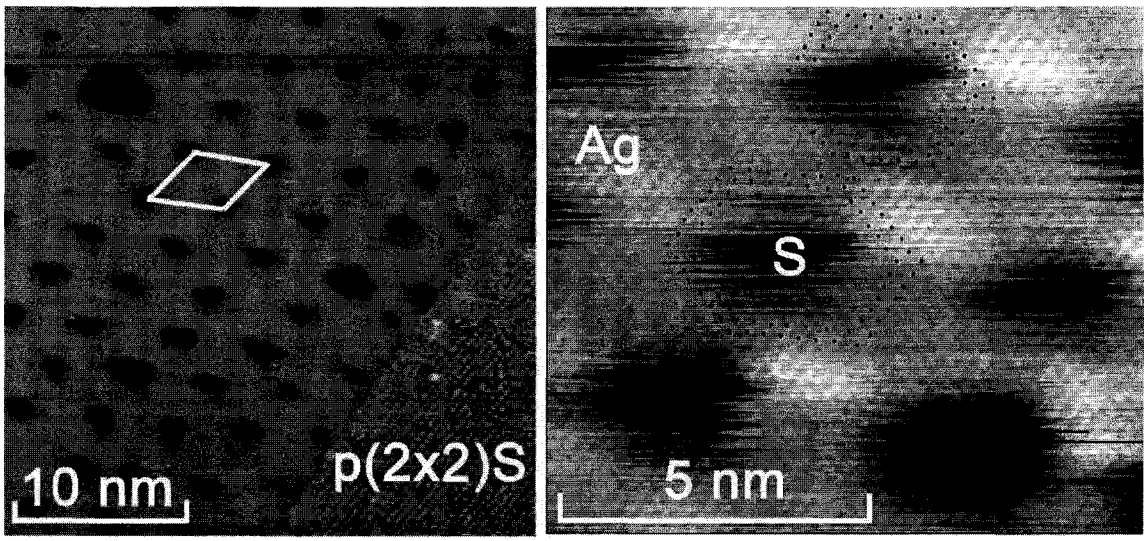

Fig. 3-7: S etching induced restructuring of the SHB of Ag/Ru(0001) (T = 295 K): (right) no threading dislocations are left in the Ag film after S etching; (left) new triangular symmetry of the superstructure with S-filled vacancy islands 50 Å apart.

The striking transformation of both misfit dislocation networks of Ag into a similar final structure requires the rearrangement of large numbers of atoms and also different mechanisms through which the strain is relieved. In the case of S adsorbed on LHB misfit dislocation network, K. Thürmer *et al.* [36] have shown how the strain relaxation mechanism involved in the formation of S filled Ag vacancies array can be explained in two steps. The first step involves the formation of S filled Ag vacancy islands at the threading dislocation core followed by the creation of adjacent triangular patches of Ag film with alternating FCC and HCP stacking. The second step involves creation of S filled Ag vacancies at their corners and followed by climb and annihilation of dislocations. In the case of S etching SHB, my experiments show that the mechanism involves a threading dislocation pair annihilation process followed by a glide of Shockley partial dislocations [98]. While S etching of LHB networks involves a reshuffling of a large number of atoms, in the case of S self–assembly

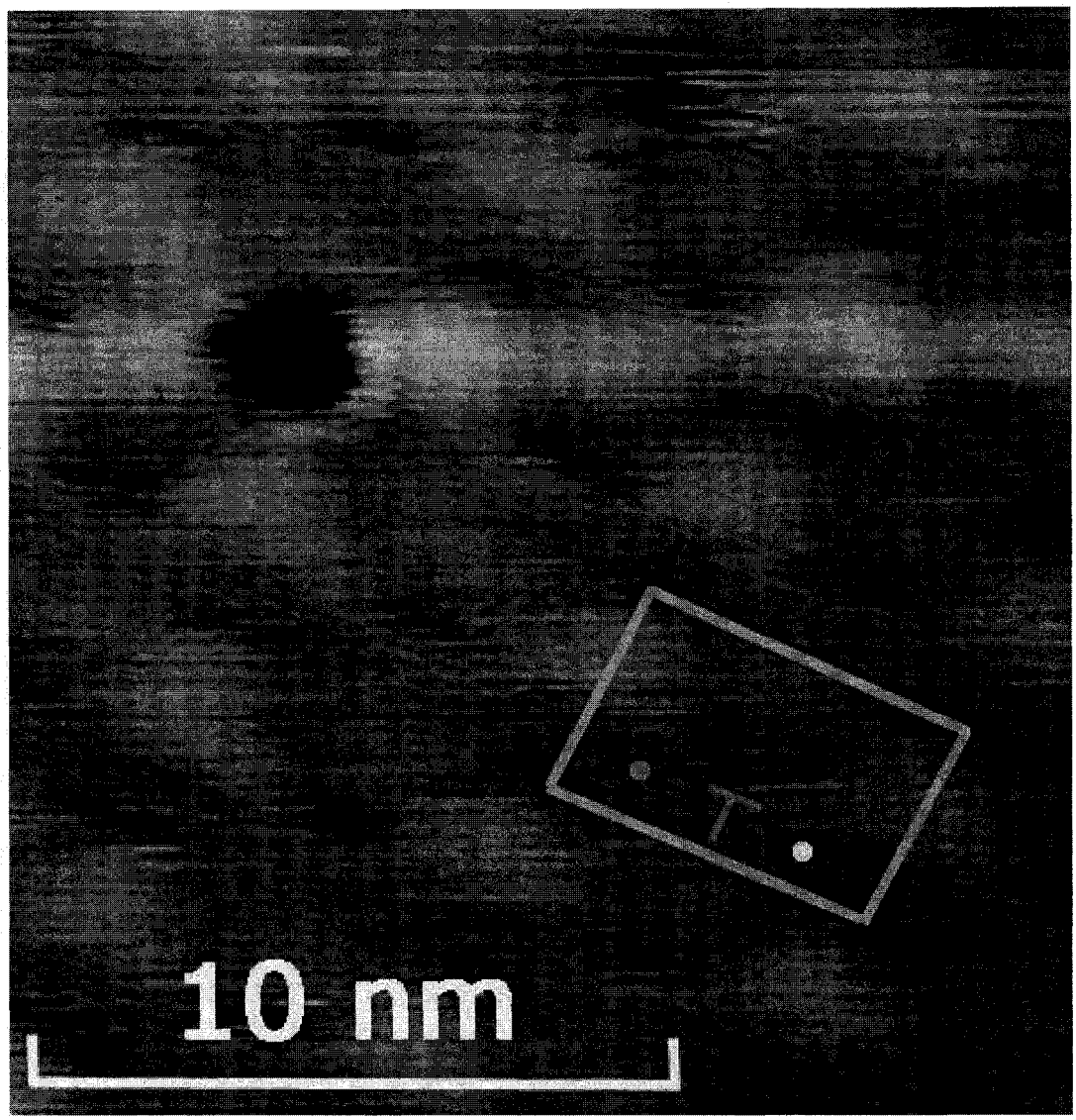

Fig. 3-8: STM image at 150 K of the initial S etching of SHB of Ag/Ru(0001) process showing two S filled Ag vacancy islands. There are two equivalent etching sites per primitive unit cell which are marked with blue and yellow dots, each of the S filled vacancies in the image residing on one of them.

on SHB networks, the self–assembly process is a local one involving only atoms in a SHB primitive unit cell.

Another example of chemical induced restructuring of a misfit dislocation network is S adsorbed on two atomic height Cu films on Ru(0001) [99, 100]. While nucleation of metallic adatoms on misfit dislocation networks usually generates circular shaped clusters,

S adsorbed on the stripe misfit dislocation of 2 ML Cu/Ru(0001) generates linear shaped S clusters of seven S atoms. They are forming the sides of equilateral triangles sitting at the threading dislocation sites of Cu, with a trigon like symmetry, shown in Fig. 3-9.

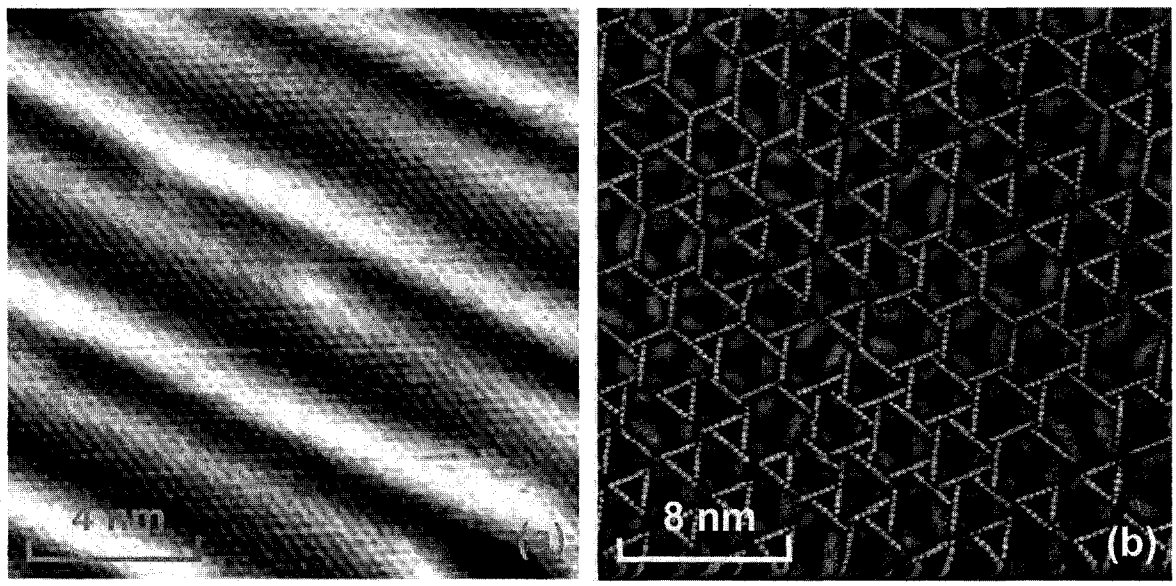

Fig. 3-9: Sulfur induced reconstruction (b) of the stripe misfit dislocation network of 2 ML Cu/Ru(0001) (a). S atoms are seen as linear bright arrays with an overall threefold symmetry (b). STM data at 295 K.

3.3.3 Limited diffusion nucleation

These strained metallic interfaces can also be used to selectively adsorb and nucleate organic molecules such as methanethiol on the FCC sites between the Shockley partial dislocations (Fig. 3-10). Pattern in methanethiol self–assembled monolayers (SAMs) [101, 102, 103] forms as a 2D imprint of ordered Co cluster–array grown on the herringbone pattern of Au(111). This cluster–array and dislocation pattern imprinting process can be applied to a wide variety of sulfur-containing molecular films. This method enables the patterning of

SAMs and ultimately the ordering of desired nanoelements such as CNTs and proteins.

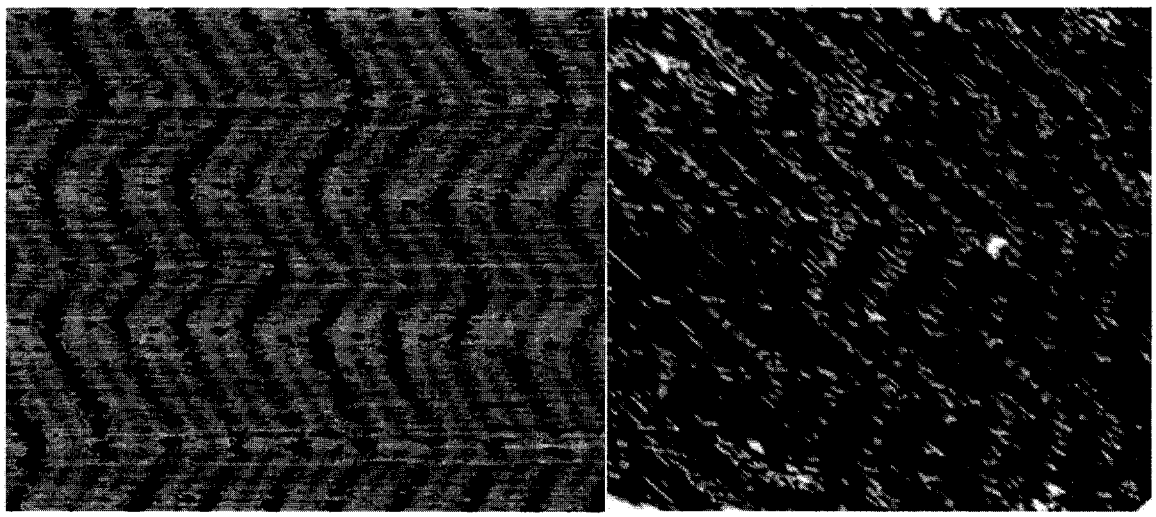

Fig. 3-10: Selective nucleation of CH_3SH molecules on the FCC sites of the misfit dislocation network of Au(111) at 150 K. Left STM image is taken in negative contrast mode with the nucleated islands of CH_3SH showing darker than Au(111); right STM image is in positive contrast mode showing CH_3SH clusters brighter than Au(111).

3.4 Conclusions

Well–ordered misfit dislocation networks of thin metal films are a viable candidate for growth of two–dimensional ordered nanocluster arrays with specific symmetries, feature size and lattice spacings. Such bottom up processes can be very complex, involving collective effects from large numbers of atoms. Understanding of these self–assembly processes requires detailed experimental information at the atomic level of large ensembles of hundreds to thousands of atoms and thus large scale VT–STM imaging is an essential tool for such studies. Large scale STM imaging can provide the information regarding structural arrangements of atoms in the reconstructed strained metallic surfaces thus assuring

enough information to be used in 2D–FK models. Also, dynamical data can provide an experimental measure of the long range stress forces which can be related via 2D–FK with inter–atomic potentials.

A detailed description of a complex self–assembly process on strained metallic interfaces is described in the following chapter.

Chapter 4

Self–Assembly of 2D Nanocluster Arrays via Dislocation Pair Annihilation and Glide

4.1 Introduction

Strain accommodation in metallic interfaces can lead to highly ordered misfit dislocation networks [29, 28, 46, 48] that can be used as a bottom up patterning method for growing ordered cluster arrays with specific size and density. In order to understand these self-assembly processes, high resolution atomically resolved structural and dynamical VT-STM information needs to be linked via atomistic models with first–principles information about the system. Here I show how in the case of S adsorbed on less than 1 monolayer (ML) reconstructed Ag films on Ru(0001) [35], the complex process in which the self assembly occurs, involving a rearrangement of many atoms towards a final equilibrium state, is driven by strain relaxation via a dislocation pair annihilation and glide process.

An excellent model system is monolayer thick Ag film on Ru(0001) [49, 87]. Hwang

et al. have observed how, due to 7% lattice mismatch between the bulk nearest–neighbor spacing of Ag and Ru, monolayer thick Ag films on Ru(0001) form two types of misfit dislocation networks, at lower than 1 ML Ag films on Ru(0001) will reconstruct into a short herringbone (SHB) pattern with a rectangular unit cell size of about 6 nm × 4 nm while at slightly more than 1 ML Ag coverage it forms a large herringbone (LHB) pattern with a rectangular unit cell of about 20 nm × 4 nm.

Deposition of sulfur onto monolayer–thick Ag/Ru(0001) generates an ordered array of S filled Ag vacancy islands, Fig. 4-1b, for both SHB, Fig. 4-1a, and LHB [37] reconstructions. Even if the initial misfit dislocation networks of Ag are so different, in both cases the three component system reaches the same final equilibrium state, thus suggesting different paths of the self–assembly processes. I show how, for the SHB case, the self–assembly follows a two step process, first by a dislocation pair annihilations, and then by a glide of dislocations. This is a process path complementary to the one described for the LHB case [36].

4.2 Experimental procedures for high purity, ultra thin Ag film growth on Ru(0001) and S cluster adsorption

4.2.1 Cleaning of the Ru(0001) single crystal

The experiment was performed in the home built UHV–VT–STM apparatus described earlier, at a base pressure of 1×10^{-10} Torr. I have used a Ru single–crystal which was cut along the (0001) plane such that the average atomic terrace width is of about 500 nm. Cleaning of the Ru(0001) surface requires removal of the carbon, which usually is the main contaminant for this material. While heating the sample, carbon atoms diffuse to the surface, creating patches of graphene sheets. An initial 500 eV Ar^+, short sputtering cycle was

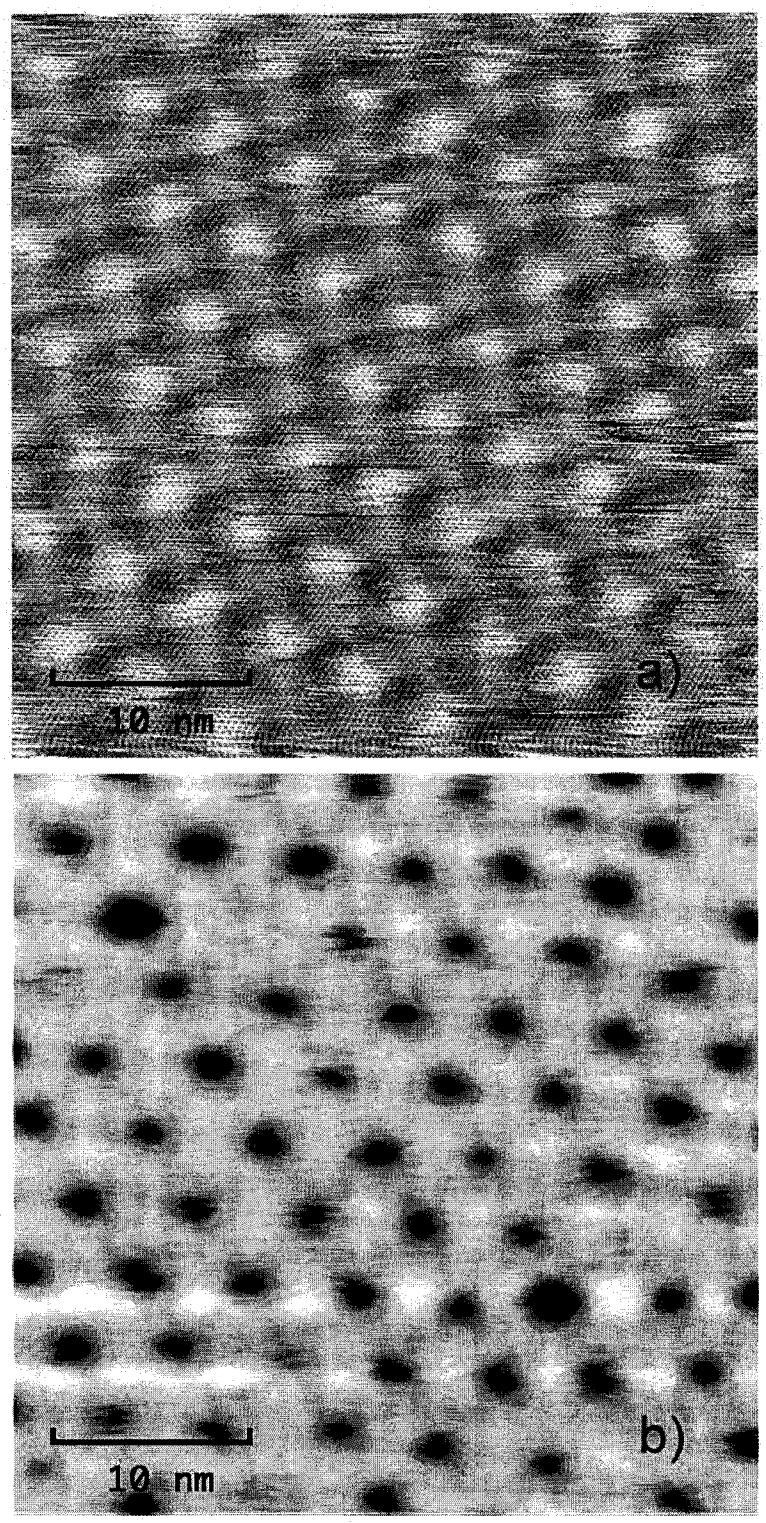

Fig. 4-1: Constant current STM images: a) SHB reconstruction of Ag/Ru(0001), b) the final S etched SHB structure of Ag/Ru(0001); both images at 295 K.

needed to break bonds in the top graphene sheet, thus making the initial oxidation faster. Cleaning was performed by repeated cycles of 10 Langmuir oxygen exposure at close to room temperature followed by flash annealing at more than 1900 K and at pressures better than 5×10^{-8} Torr. More than 2000 cleaning cycles were needed in order to deplete the bulk crystal vicinal to the sample surface of the contaminating carbon. At the end of these cleaning cycles, no Auger electron spectroscopy (AES) carbon signal could be detected. Also, low energy electron diffraction (LEED) showed very sharp first order diffraction spots and the STM images shown clean, cluster free, large and atomically flat terraces of the Ru(0001) surface. Before each new experiment, the Ru(0001) sample was cleaned by doing 10 to 15 cleaning cycles of 10 L oxygen followed by flash annealing at about 2000 K in oxygen partial pressures better than 5×10^{-9} Torr.

4.2.2 Growth of ultra thin Ag films on Ru(0001)

The Ag films were then grown by physical vapor deposition (PVD) method from a home built evaporative Ag cell onto a freshly cleaned Ru(0001) surface while maintaining the sample temperature at around 450 K. The Ag evaporator cell consists of a high purity (4N5) tungsten filament with a diameter of 6 mil shaped as a basket in which a high purity (5N) Ag pellet was mounted. The W basket is mounted on the Cu electrodes of an electrical feed–through inside of a St.–St. 304 cylinder with a circular aperture at the end and an externally and manually actuated shutter. After the Ag evaporator is placed for the first time in the UHV chamber, an initial preparation procedure needs to be followed in order to obtain reliable and stable Ag evaporation rates, and contaminant–free Ag films onto Ru(0001). The first stage in this preparation is to thoroughly degas the Ag source by running it incrementally at higher and higher power until no pressure burst was observed

any longer, and followed by longer degassing, for more that 24 hours, at about 80% of the maximum power, until the pressure recovered in the main UHV chamber. The next step involves the surface melting of the Ag pellet such that, at the end, Ag wets the W filament, thus insuring a stable position of the Ag pellet in the basket, therefore a stable resistance of the evaporator. Melting of the Ag pellet can be observed visually if a line of sight viewport is available, in which case the rounding of the edges of the Ag pellet during melting can be easily spotted or, if there is no way to directly see the Ag pellet, a jump in the W filament voltage at fixed current can be observed and that usually is related with a wetting of the W filament. This is needed for reproducible Ag evaporation rates since the control over the current running through the W filament needs to have a precision and stability down to few mA, which corresponds to power stability better than 0.5%. At the end, a calibration of the Ag source is performed by depositing Ag onto clean Ru(0001) and inspecting with the STM the coverage obtained for a given filament power and exposure time. Ag coverage can be easily determined with STM since Ag films on Ru(0001) grow in step flow mode (Fig. 4-2) at room temperature and above. In this way, low Ag deposition rates down to 1 ML/min can be obtained, with the overall Ag coverage controlled by the deposition time.

4.2.3 Electrochemical S_2 source and S coverage calibration

In the following experiments, molecular sulfur was provided by an electrochemical cell [97] with an active area composed of a layered structure of $Ag|AgI|Ag_2S|Pt$. The whole active area of the cell is heated via a high purity (4N5) tungsten filament at temperatures up to 530 K. The Ag ions in the cell become mobile enough above 430 K. Thus, under a small bias voltage of about –0.3 V on the Pt electrode, the following global reaction takes place $2Ag_2S \rightarrow 4Ag + S_2$, releasing molecular S gas into the UHV chamber.

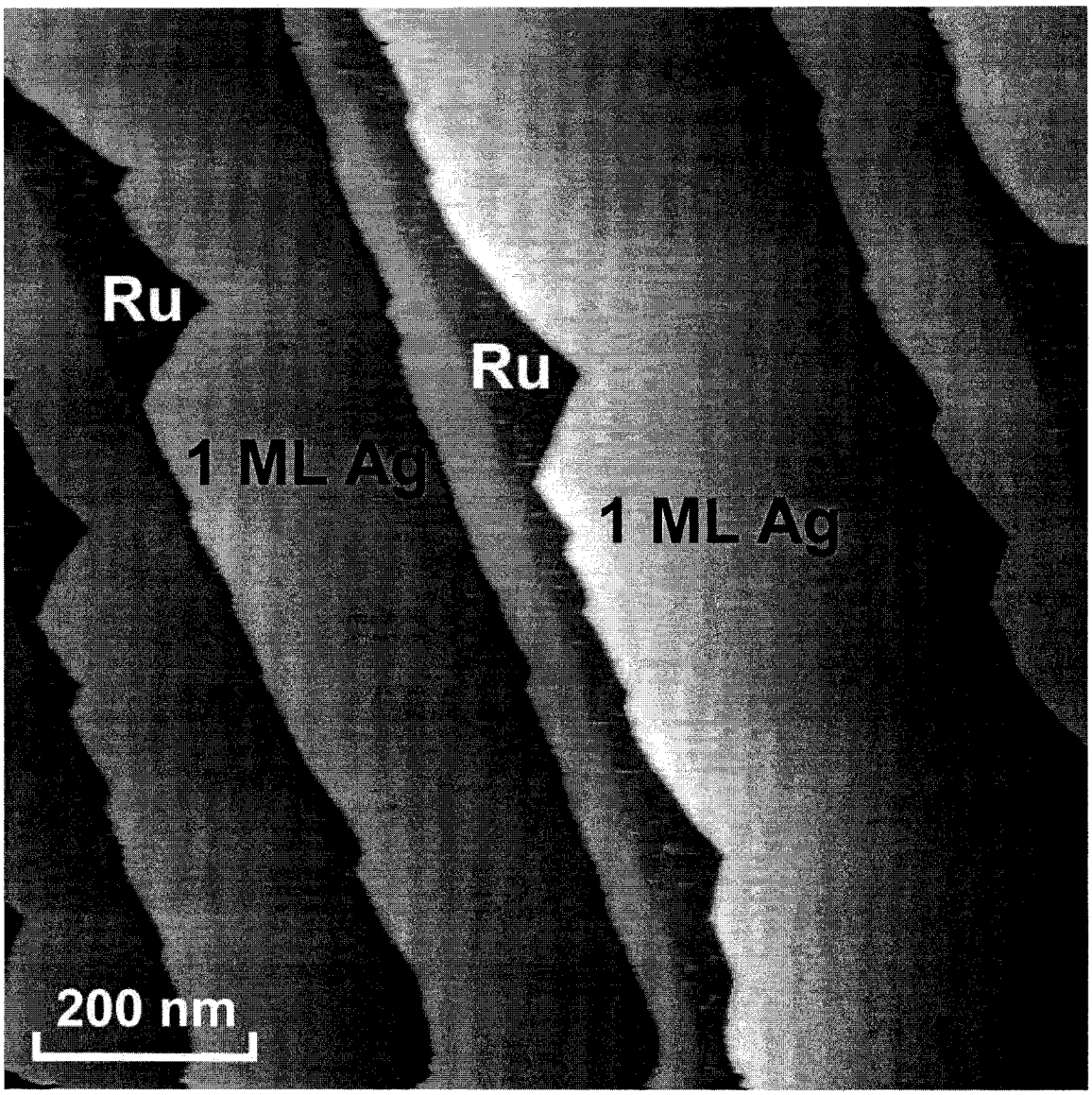

Fig. 4-2: Large scale STM image of the step flow growth of one atomic layer thick Ag films on Ru(0001). Ag film is seen as brighter areas on the darker Ru(0001) substrate growing from the terrace edge of Ru(0001) substrate. Ag was deposited at 1 ML/min while the sample was at 450 K. STM data acquired at 300 K.

S exposures from the electrochemical cell on clean Ru(0001) sample or freshly prepared Ag films were done at room temperature and monitored with a mass spectrometer by following the masses at 32 and 64 a.m.u. One of the challenges of the investigation of the

self–assembly process of S clusters grown onto one atomic layer Ag films on Ru(0001) is the precise control of S coverage. Resolutions down to 10^{-3} ML of S normalized to Ru(0001) surface are needed ant that is well beyond the standard coverage determination method, AES, which provides a coverage resolution, usually of about 1% of a monolayer. Such a S coverage resolution was obtained by calibrating the S exposure, measured as a time integral of the partial pressures of 32 and 64 a.m.u. monitored with a mass spectrometer, against the S/Ru(0001) phase diagram [104] monitored by LEED images for a fixed geometry of the S_2 cell, Ru(0001) sample, and mass spectrometer, and for a fixed sample temperature.

For this purpose I wrote a Labview application that fully controls the residual gas analyzer on the chamber (Stanford Research Systems RGA–300 – a mass spectrometer measuring up to 300 a.m.u.) based on the Labview drivers for that instrument provided by the Labview and SRS companies.

From the kinetic theory of gases, the rate r of arrival of atoms or molecules at a given surface in the vacuum chamber is proportional to the atomic or molecular density n and the mean free speed of the molecules $< v >$ [105]:

$$r = \frac{1}{4} n < v >, \tag{4.1}$$

where for the Maxwell–Boltzmann distribution of velocities at temperature T for a gas of molecules of mass m, the average speed of the molecules is given by

$$< v > = \int_0^{+\infty} v\, f(v)\, dv = \sqrt{\frac{8 k_B T}{\pi\, m}}, \tag{4.2}$$

with k_B being the Boltzmann constant. The arrival rate of molecules for an ideal gas ($P = n k_B T$) results to be depending only on the temperature and pressure

$$r = \left[\frac{1}{2\pi m k_B T}\right]^{1/2} P. \tag{4.3}$$

The mass spectrometer measures the partial pressures in the vacuum chamber of various atomic and molecular species therefore it is possible to monitor the time evolution of S_2 and S and calculate the total S exposure of a freshly cleaned Ru(0001) sample as:

$$S\ exposure = \frac{3.51 \times 10^{22}}{L}\left[\frac{2}{(M_{S_2}T)^{1/2}}\int_{t_0}^{t_1} P_{S_2}(t)dt + \frac{1}{(M_S T)^{1/2}}\int_{t_0}^{t_1} P_S(t)dt\right], \quad (4.4)$$

where the partial pressures P_{S_2} and P_S are measured in Torr, the masses are $M_{S_2} = 64\ a.m.u.$ for S_2, and $M_S = 32\ a.m.u.$ for S, the temperature is T = 295 K, and $L = 1.58 \times 10^{15}\ atoms/cm^2$ is the atomic density of hexagonal Ru(0001) surface. Even if the electrochemical sulfur cell is releasing mostly molecular sulfur, the mass spectrometer ionizer cracks a significant number of S_2 molecules, thus the need to take into account both molecular and atomic S contributions. Since the mass at 32 a.m.u. corresponds also to O_2, a background subtraction method was applied by measuring the levels of molecular oxygen in the vacuum chamber before S exposure. The traces of molecular oxygen are due to the cleaning procedure of Ru(0001), which involves repeated exposures of its surface to a few Langmuir of O_2 followed by flash annealing.

The calibration of the S exposure, which is measured based on equation 4.4, was performed by comparing the LEED patterns for various exposures with the known, experimentally determined, phase diagram of S on Ru(0001) [104]. The transition from $p(2 \times 2)$ (Fig. 4-3b) to mixed $p(2 \times 2)$ and $(\sqrt{3} \times \sqrt{3})R30°$ (Fig. 4-3c) could be precisely obtained by incrementally increasing the S exposure on Ru(0001). This transition corresponds to a 0.25 ML S coverage normalized to Ru(0001) surface. Also, in the mixed phase region, the S exposure for the highest intensity LEED spots for both $p(2 \times 2)$ and $(\sqrt{3} \times \sqrt{3})R30°$ was chosen as a second point in the S exposure calibration and it corresponds to 0.3 ML S on Ru(0001). In all those S exposures, the Ru(0001) sample temperature was kept at 295 K.

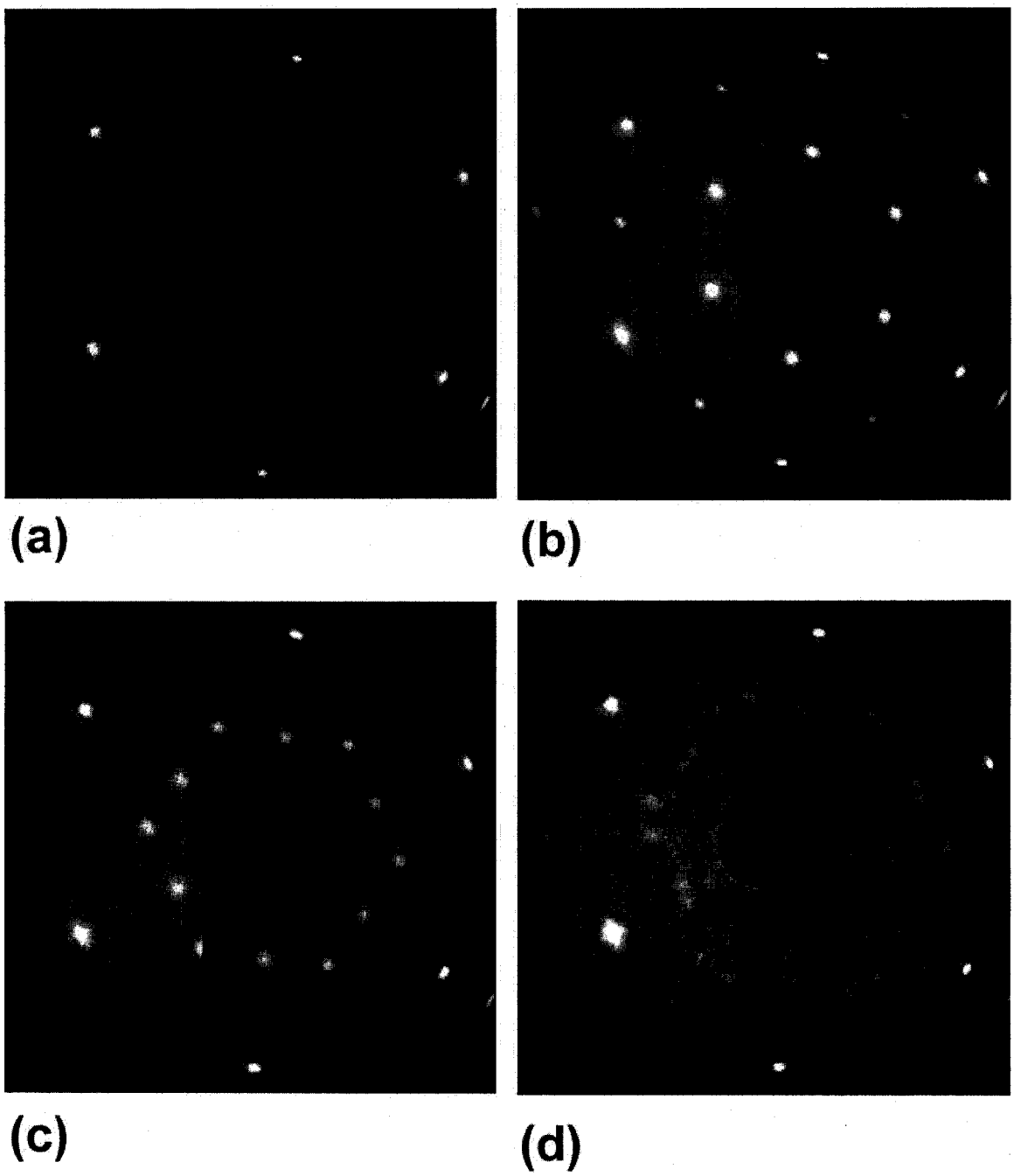

Fig. 4-3: LEED pattern of some of the various S phases on Ru(0001) surface: (a) clean Ru(0001), (b) $p(2 \times 2)$ S on Ru(0001), (c) mixed phase $p(2 \times 2)$ and $(\sqrt{3} \times \sqrt{3})R30°$ of S on Ru(0001), (d) striped domain wall of S on Ru(0001). All LEED data at 295 K and energy of the incident electrons of 57.5 eV.

4.3 Experimental investigation of the self–assembly of S filled Ag vacancy islands on SHB of Ag on Ru(0001)

4.3.1 Phase diagram of S filled Ag vacancy islands grown on SHB of Ag on Ru(0001)

Having the ability of precisely measuring the S coverage, I was able to experimentally map the phase diagram of S filled Ag vacancy islands as a function of S coverage. The experiments started with about 0.5 ML Ag films grown onto Ru(0001), thus forming a short herringbone misfit dislocation network on which, at room temperature (approx. 295 K), various S exposures have been performed with the S coverage determined based on the mass spectrometer calibration described in the previous section. Based on multiple STM images acquired at room temperature, an average surface density of the S filled Ag vacancies could be measured as a function of S coverage. Also, the surface area of the S filled Ag vacancy islands could be measured.

In order for this procedure to work independently of the STM data set used, a threshold technique was used. First, a measurement of the top–bottom distance (or bright–dark vertical distance) was performed. In the next step the threshold for establishing the perimeter of the S filled Ag vacancy was set for all data sets analyzed at 0.9 of the top–bottom distance. This step is justified due to the fact that the topographic STM images contain artifacts due to the finite dimension of the apex of the STM tip. Even for very sharp tips like those used in these experiments, which basically assured that most of the contributions to the tunneling current came from one atom sitting at the apex of the STM tip, the feature sizes of the S vacancies are very small, of the order of few atomic distances. The following step involved the creation of a 2 bit color image, where one color (black for example) was

assigned to z values below the threshold value, corresponding to the S filled vacancy islands, and the other color (white for this example) was assigned to all other areas. In the last step, the area of each island of black pixels was measured, the result being then plotted in a histogram which was then fitted with a Gaussian distribution. The mean value of the fit

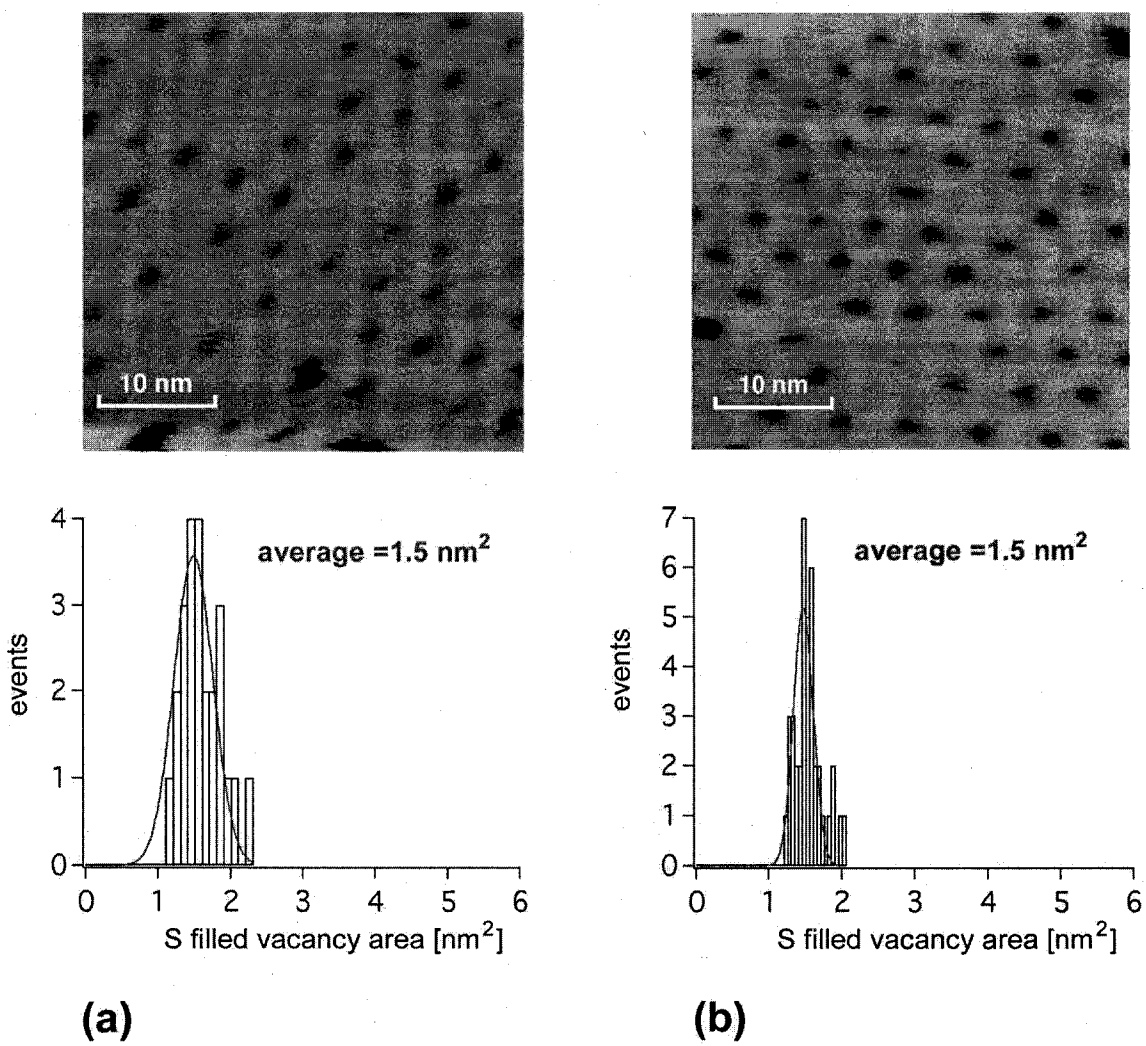

Fig. 4-4: Dilute phase of S filled Ag vacancy islands grown on SHB of Ag on Ru(0001): (a) for S coverage of 2.8 $\times 10^{-3}$ ML the average size of the S filled Ag vacancy islands is 1.5 nm^2; (b) the S coverage is 13.7 $\times 10^{-3}$ ML and the S filled Ag vacancy islands have an average also of 1.5 nm^2. All STM data were taken at 295 K and the S_2 was deposited at the same temperature.

therefore gave the average size of the S filled vacancies for a given S coverage.

S filled Ag vacancies grow (or self–assemble) on the SHB of Ag/Ru(0001) in a two stage process. At low S coverage, individual vacancy islands with a fixed size are formed, and their density is increasing with the sulfur coverage until an almost complete array of vacancy islands is formed. Examples of STM data for this regime, along with the statistics for the S filled Ag vacancy islands sizes are shown in Fig. 4-4.

As the S coverage increases beyond the point when a complete array of S filled Ag vacancy islands is formed, the size of islands starts growing, as seen in the examples presented in Fig. 4-5.

Corroborating the results from various STM data sets taken for different values of the S coverage, the evolution of S filled Ag vacancy islands surface density and size is plotted in Fig. 4-6. Several important observations can be made. First, after S coverage exceeds the threshold values of ~18 mML, the S-filled vacancy islands start growing in size. This is the threshold coverage between the dilute and solid phases. Only when the S coverage increases above the transition value from dilute to solid phase does the average size of the S filled Ag vacancy islands increase. In the solid phase, the surface density of S filled vacancies is constant and has a value of exactly half the surface density of the threading dislocation cores of the SHB network of the Ag film on Ru(0001), which is about 6 $\times 10^{-3}$ ML (Fig. 4-6a). This fact suggests that two threading dislocation cores are somehow replaced by a S filled Ag vacancy. From Fig. 4-6a we see that for a S coverage of about 3 $\times 10^{-3}$ ML, the S filled Ag vacancy islands take about 50% of the total number of vacancy islands in the solid phase, which have a density of 3 $\times 10^{-3}$ ML, resulting in a ratio of 2 S atoms per S filled Ag vacancy island in dilute phase. This last result, combined with the fact that the electrochemical cell produces mostly molecules of S_2 means that each S_2 molecule

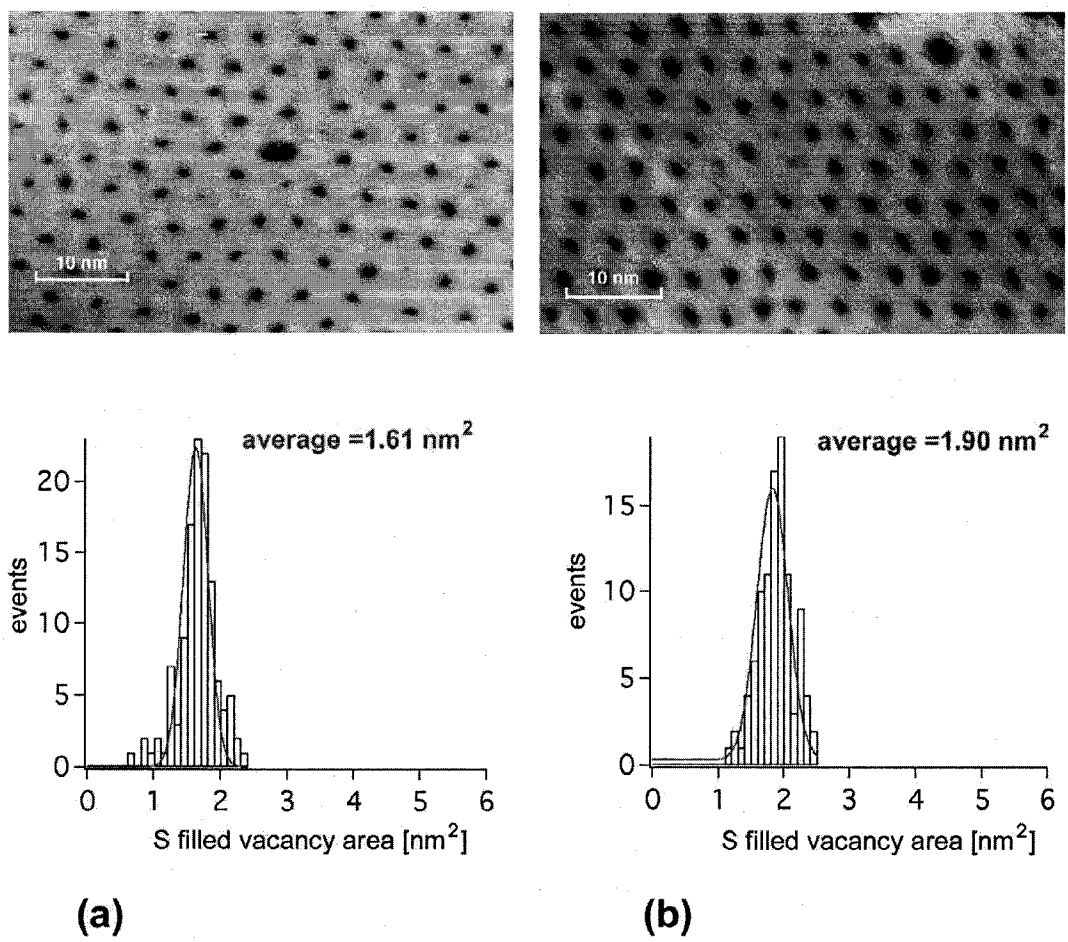

Fig. 4-5: Solid phase of S filled Ag vacancy islands grown on SHB of Ag on Ru(0001): (a) for S coverage of 21.0 $\times 10^{-3}$ ML the average size of the S filled Ag vacancies is 1.61 nm^2; (b) the S coverage is 41.5 $\times 10^{-3}$ ML and the S filled Ag vacancies have an average size of 1.90 nm^2. All STM data were taken at 295 K and the S_2 was deposited at the same temperature.

once reaching the Ag surface triggers the creation of a Ag vacancy island and becomes trapped in it (Fig. 4-7). Also, in the same regime, the average size of S filled Ag vacancies is independent of S coverage and it has a value centered around 1.5 nm^2 (Fig. 4-6b). This vacancy island area is much larger than the footprint of 2 S atoms on Ru(0001) which, for a $p(2 \times 2)$ phase, would cover about 0.46 nm^2. We therefore have to conclude that the number of S atoms per Ag vacancy does not relate directly, via a static structural model,

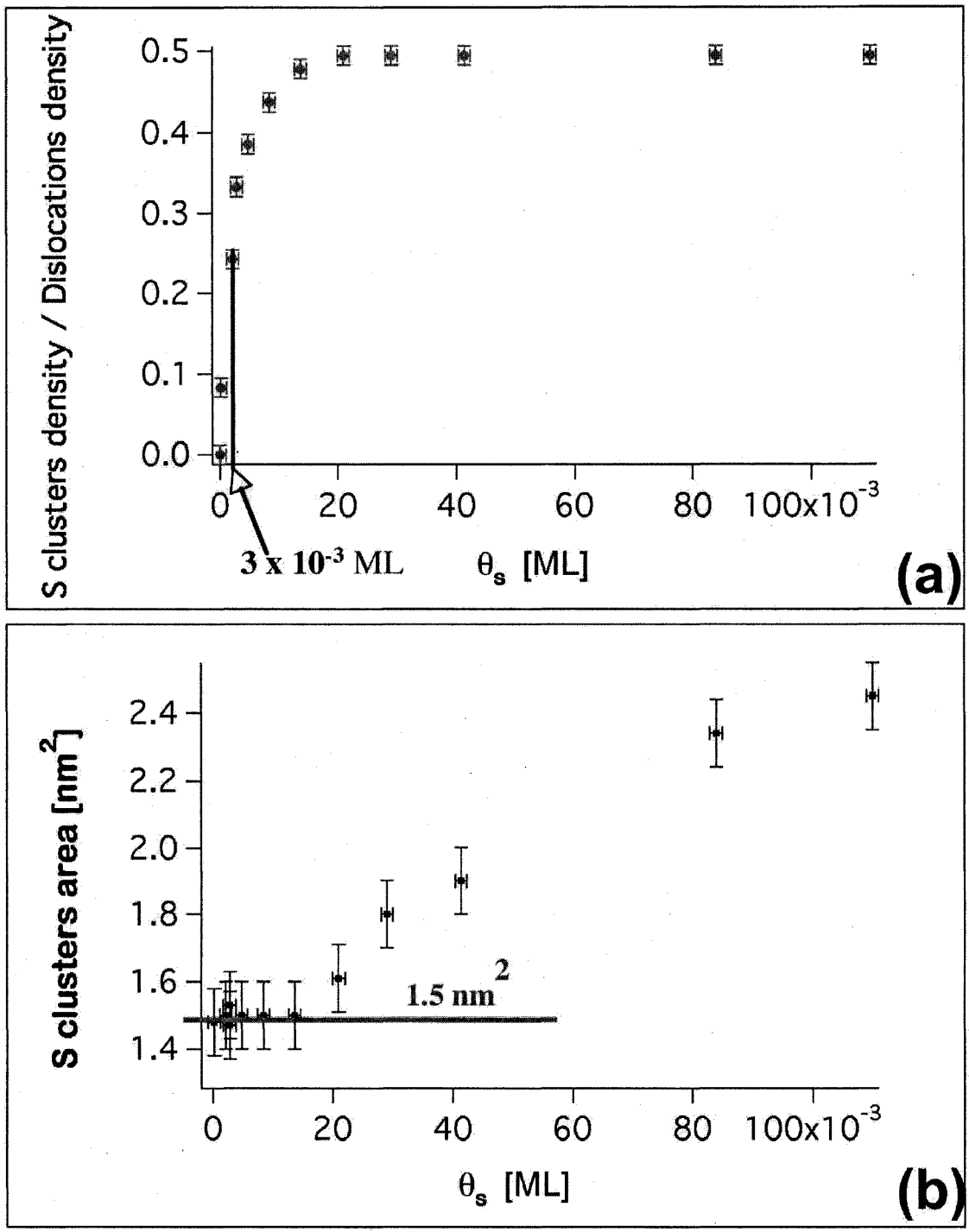

Fig. 4-6: S-filled Ag vacancy island growth as a function of S coverage: (a) the ratio of vacancies islands surface density vs. threading dislocation surface density, (b) S-filled Ag vacancies islands' size dependence on S coverage.

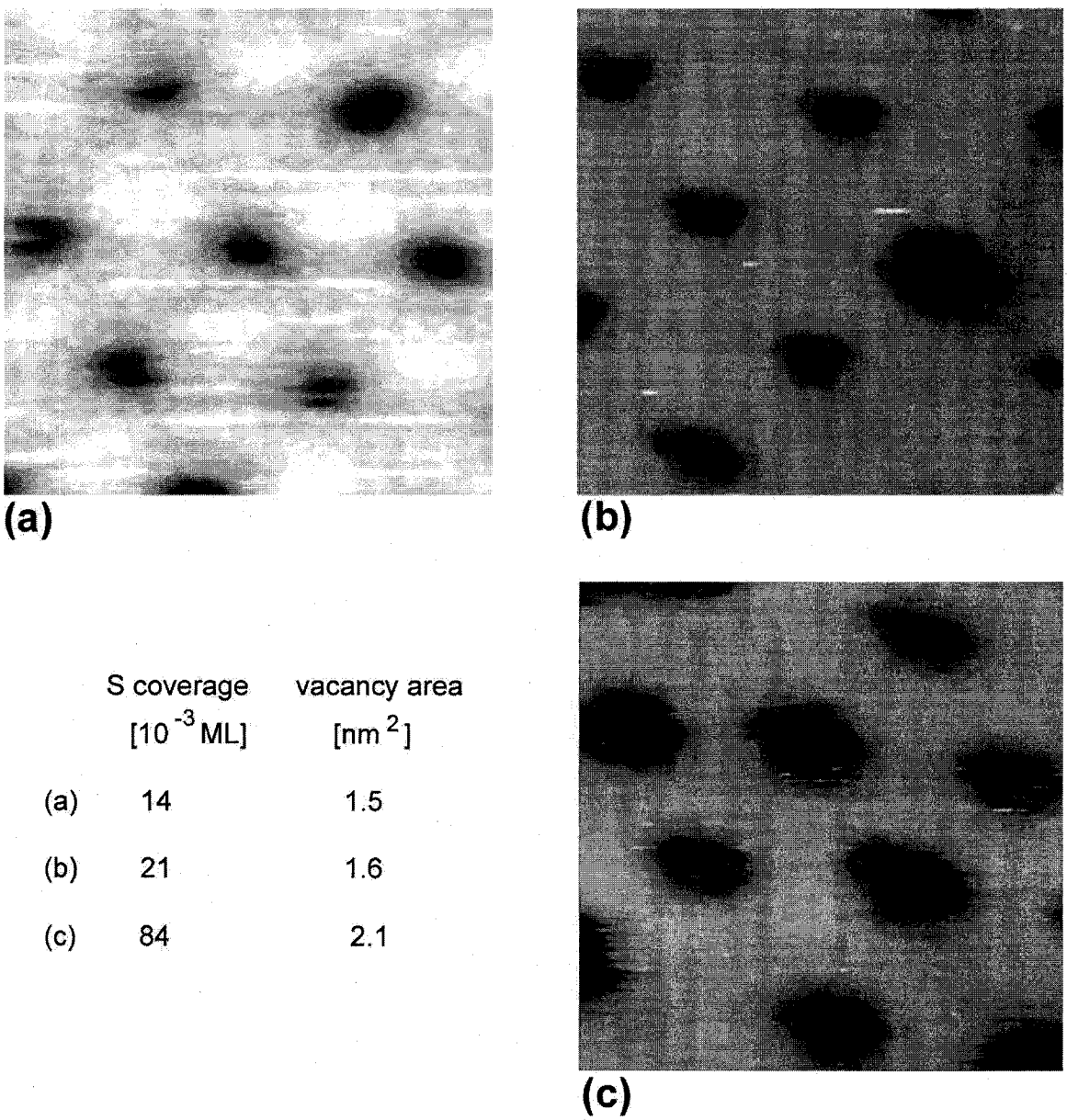

Fig. 4-7: STM images of S filled Ag vacancy islands (darker areas) for three S coverage values: (a) a cluster of vacancy islands at 14 $\times 10^{-3}$ ML corresponding to the dilute phase, (b) at 21 $\times 10^{-3}$ ML it is right above the transition coverage from dilute to solid phase, (c) at 84 $\times 10^{-3}$ ML it shows increased sizes of the vacancy islands in the solid phase. The last image shows the $p(2 \times 2)$ structure of the S atoms trapped in the Ag vacancy island. The inset table gives the coverage and vacancy size for each image. All STM images have been acquired at 295 K and they are 13 $\times$ 13 nm^2.

with the area size of the Ag vacancy in the dilute phase.

4.3.2 Short herringbone misfit dislocation network of 1 atomic layer Ag on Ru(0001)

A detailed knowledge of both initial and final state of the process is mandatory for an atomistic model describing the self–assembly process. Due to the large unit cell size of misfit dislocation networks of metal surfaces or metallic thin films grown on metal surfaces, a pure first–principles approach to describe the process through which hundreds to thousands of atoms are rearranging their configurations in order to minimize their global energy is so far impossible to implement. An alternative approach is to use high resolution scanning probe microscopy structural and dynamical information about the self–assembly process as guidance for building a less complex physical model based on first–principles interaction parameters. In the case of S clusters self–assembling on the SHB misfit dislocation network of 1 atomic layer high Ag films grown on Ru(0001), the starting point is a detailed atomically resolved structural description of the SHB reconstruction.

Fig. 4-8 shows atomically resolved STM images of SHB of Ag/Ru(0001) at 295 K (1) and 110 K (2). The overall corrugation at 295 K looks different than at 110 K mainly due to the dynamics of SHB misfit dislocation network at temperatures close and above room temperature. A careful mapping of the threading dislocation (TD) cores has been carried out on a larger image than shown and I found that the dimensions $a \times b$ of the rectangular unit cell shown in Fig. 4-8a are peaked at 18(19) $\times$ 15(16) Ag atoms. Investigation of the same structure at 110 K, where it is more stable during the time of STM imaging, shows the misfit dislocation network as an array of Shockley partial dislocations terminated in pairs at the threading dislocation core shown by the dark rows of atoms (Fig. 4-8b). A

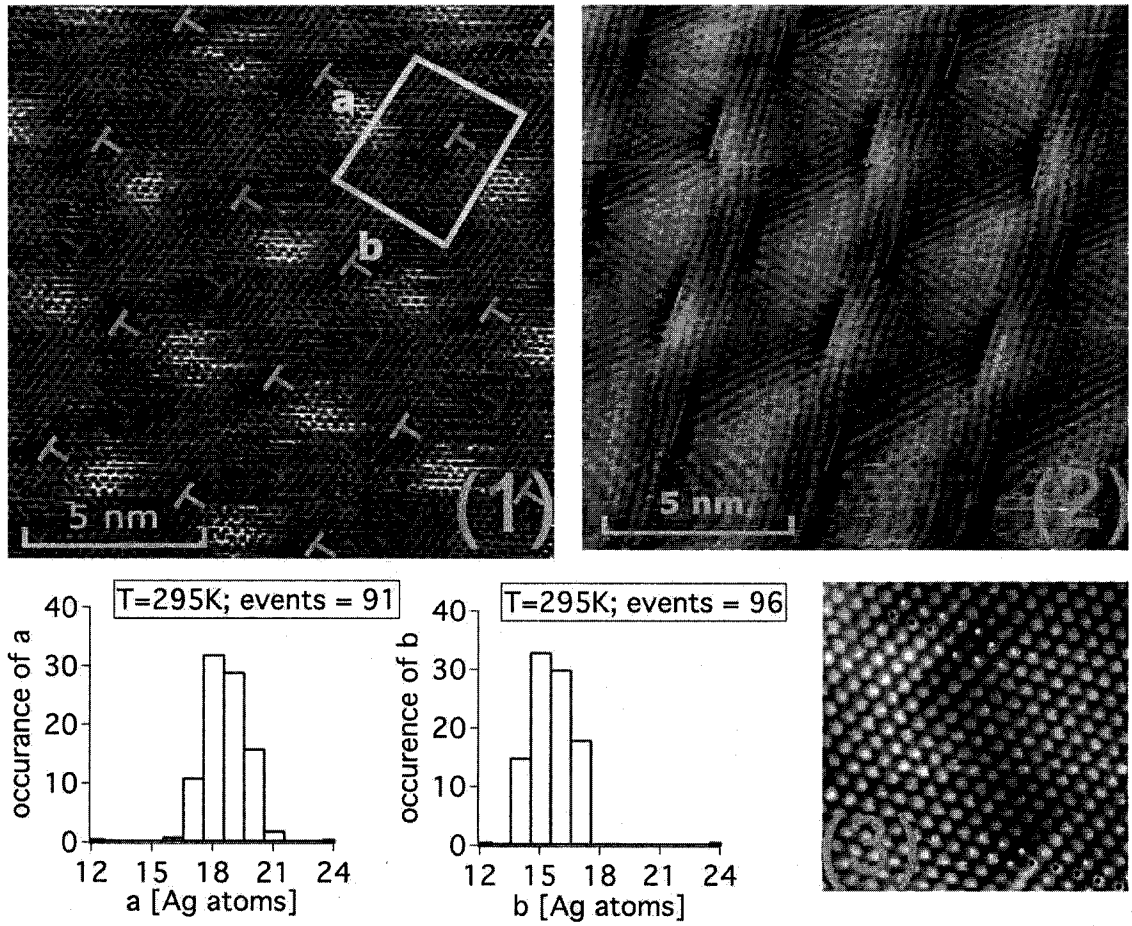

Fig. 4-8: Constant current image of 1 atomic layer thick Ag film on Ru(0001); the overall Ag coverage is less than 1 ML normalized to Ru(0001) substrate: (1) at 295 K (–20 mV sample bias, 4.6 nA), (2) at 110 K (–43 mV sample bias, 7.6 nA); red and blue T's are marking the threading dislocation (TD) positions, (3) is an inset of a pair of TD's at 110 K, the histograms show the distributions of the unit cell sizes a and b which have been measured from larger STM images.

higher resolution inset is shown in Fig. 4-8c with the extra rows of atoms marked by red and blue lines of dots. The unit cell size is found for the low temperature data to be again 18(19) × 15(16) Ag atoms.

The SHB Ag structure as seen from STM data (Fig. 4-8) is a misfit dislocation network

characterized by (a) a striped type dislocation pattern, with individual Shockley partial dislocations (yellow lines in Fig. 4-9) marking the separation between alternating FCC and HCP stacking areas of the Ag atoms on the Ru(0001) substrate, and (b) edge dislocations, whose line directions thread perpendicular to the substrate through the film, hence named

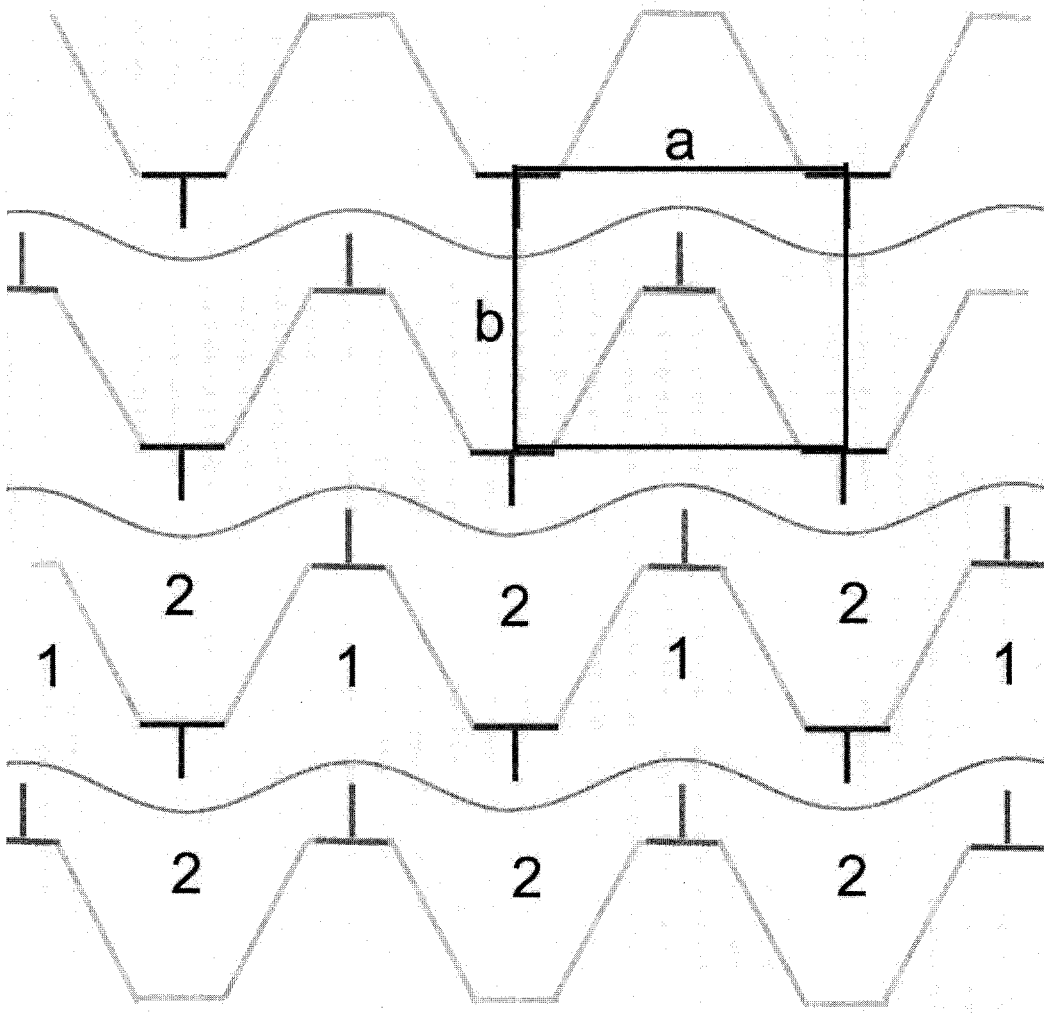

Fig. 4-9: Schematics of Ag/Ru(0001) SHB misfit dislocation network. Yellow zig–zags represent one set of Schockley partial dislocations with the threading dislocations located at the "elbow" (red and green T's). The second set of Shockley partial dislocations are shown as orange lines. The unit cell of the reconstruction is shown in blue.

threading dislocations, which are located at the meeting area of two Shockley partial dislocations (red and green T's in Fig. 4-9). These threading dislocations are seen in the STM image taken at low temperature (Fig. 4-8.2) as darker atomic rows of Ag atoms at the "elbow" of this zig–zag pattern. The second set of Shockley partial dislocations, which is marked with orange curved lines in Fig. 4-9, does not align along a fixed lattice direction. Any of the two consecutive Shockley partial (yellow and orange lines) bound Ag film areas with similar stacking geometry, FCC or HCP as shown by the areas marked with 1's and 2's in Fig. 4-9. Compared with Au(111) or LHB of Ag on Ru(0001) misfit dislocation networks, the SHB network does not have fixed width of the FCC or HCP areas. It is important to note that STM corrugation measurements cannot give a direct assignment of the areas marked with 1's for example to a FCC or HCP stacking. As I will show in the theoretical section of this chapter, the yellow Shockley partial dislocation lines are running along the compact directions of the Ru(0001) substrate, different than in the case of Au(111) or LHB where the preferred direction is $[11\bar{2}]$. Along the longer side of the unit cell of the reconstruction seen in STM data of Fig. 4-8, the Ag film adopts the lattice spacing of the Ru(0001) substrate, but along the shorter unit cell direction, 15 (16) Ag atoms are stretched along 16 (17) Ru(0001) atoms.

Large scale STM images show that the SHB network is well ordered on large Ru(0001) terraces with large–size domains running in one of the possible three symmetrical directions.

4.3.3 Self–assembly process of S filled Ag vacancy islands on Ru(0001) observed by STM

Now that we have STM based structural information about the initial state of the Ag SHB system, the next step is to describe the final state after formation of a complete and ordered

array of S filled Ag vacancy islands along with the dynamical growth process which will shed some light on the complexity of the self–assembly process.

STM data presented in Fig. 4-10 offers structural insight into the final state of S induced reconstruction. At a S coverage close to the transition from the dilute phase of S filled Ag vacancy islands to the solid phase, when a complete Ag vacancy island array forms, the rectangular symmetry of the initial SHB network of Ag changes to a triangular symmetry, with Ag vacancy islands about 5 nm apart, as seen in left image of Fig. 4-10. This distance corresponds to 18 or 19 Ru atoms in a compact direction of the (0001) surface. Such a symmetry change requires a large scale reorganization of the Ag film, its atoms reshuffling in a process towards a final global minimum energy of the two component system on Ru(0001). The fact that the same final arrangement of S filled Ag vacancy islands is reached for S

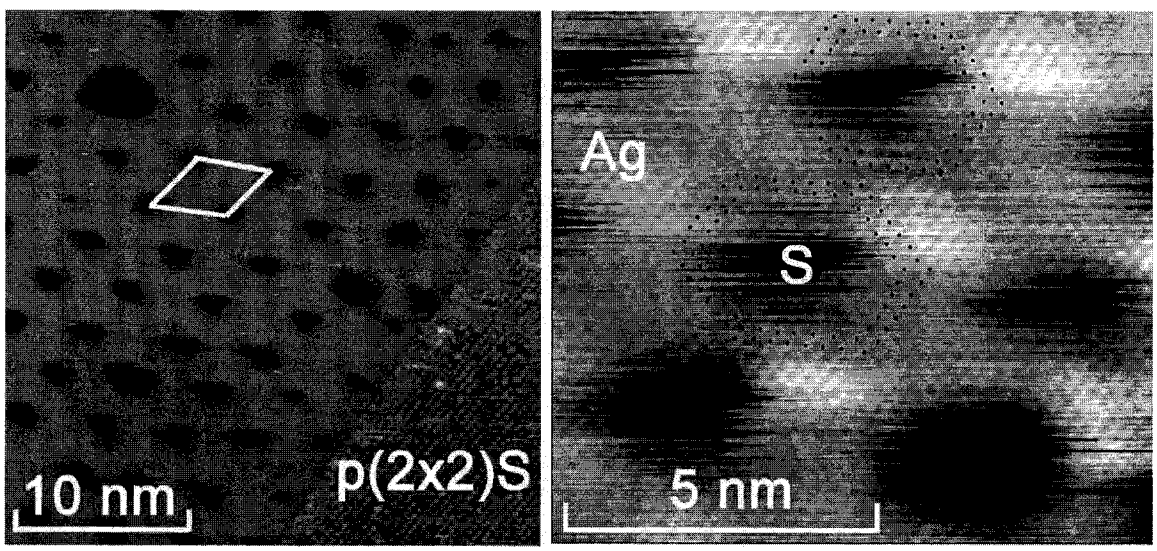

Fig. 4-10: S etching induced restructuring of the SHB of Ag/Ru(0001) ($T = 295$ K): (right) no threading dislocations are left in the Ag film after the S filled Ag vacancy island array is formed at a S coverage of 18 $\times 10^{-3}$ ML, (left) new triangular symmetry of the superstructure with S–filled Ag vacancy islands 50 Å apart; S coverage is 21 $\times 10^{-3}$ ML.

adsorbed on both SHB and LHB networks unambiguously proves that the final state is an equilibrium phase. High resolution, atomically resolved STM data of the solid S cluster phase, like the right image shown in Fig. 4-10, reveal the atomic arrangement of the Ag film around the S filled vacancy islands. In the same figure I marked for clarity the positions of Ag atoms along hexagonal circuits around two of the S filled vacancy islands. In this way, experimentally it is seen that there are no threading dislocations left in the Ag film, another indication that many Ag atoms moved in the self–organization process. Moreover, the same image shows a three–fold symmetry of the long range corrugation of the Ag film around any of the Ag vacancy islands. This long range corrugation is the same as the long range corrugation across the Shockley partial dislocations seen by STM on the SHB of Ag (Fig. 4-8), which corresponds to the height difference between FCC and HCP stacking regions

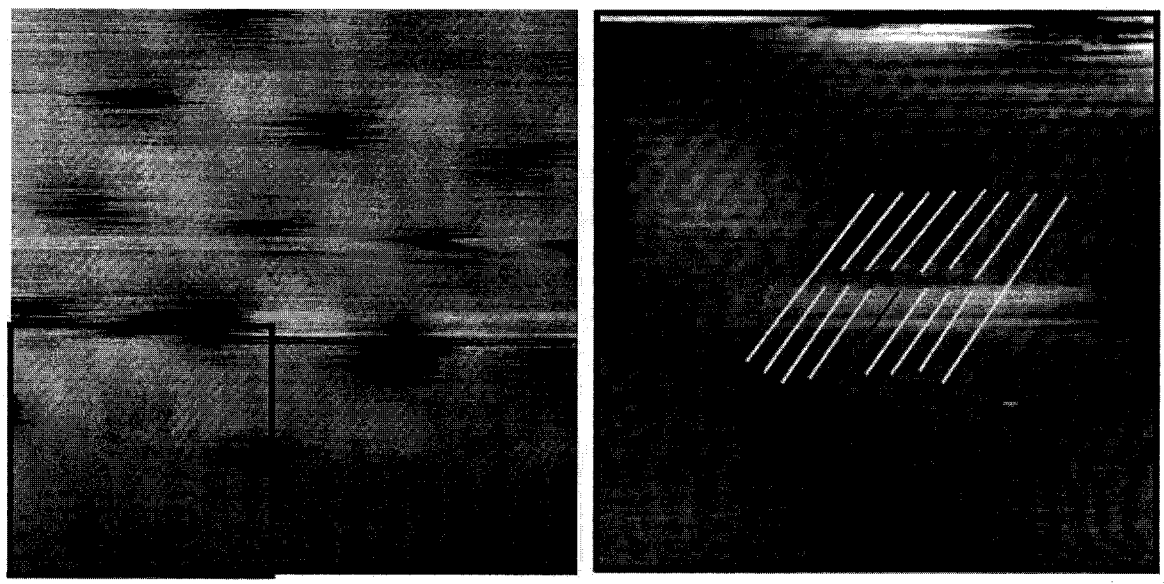

Fig. 4-11: Atomically resolved STM image of the Ag film around Ag vacancy islands in the dilute phase regime. Right image is an inset from the left showing the presence of an extra row of atoms marked with the red line – a TD site – surrounded by S filled Ag vacancy islands. Left image is 17 × 17 nm^2.

(Fig. 4-9).

Since the final state, when a complete array of vacancy islands is formed, is so different from the initial state represented by the SHB network of Ag, and since the number of atoms per unit cell is about 300, one might ask if the self–organizing process is a local one or not. Inter–atomic interactions seem not to be effective in mediating such a long range order due to their short range. Thus, one might ask what type of forces are driving the self–assembly process. One way of testing the range of interactions responsible is to look at intermediary situations of the process, when the density of Ag vacancy islands did not reach saturation yet. From the phase diagram shown earlier, if the S coverage is below the threshold value of about 18 $\times 10^{-3}$ ML, S filled Ag vacancy islands do not yet form a complete array (dilute phase). In such a case, atomically resolved STM data, like the one in Fig. 4-11, show that the rearrangement of Ag atoms is a process acting on the length scale of one unit cell of the Ag reconstruction since the Ag film in the vicinity of five surrounding vacancy islands still carries the initial threading dislocation core. This is clear evidence that the interaction mediating the self–assembly process is of an effective type and has a range of at most the size of one unit cell of the SHB reconstruction. This length scale argument indicates that the final equilibrium state is mostly dictated by relaxations in the Ag film, with S atoms trapped in the Ag vacancy islands not having much effect past their neighboring area. Since the binding energy of S on Ru(0001) of about 2 eV [36] is one order of magnitude larger than the binding energy of Ag on Ru(0001) [36], S will preferably bind on Ru. Moreover, from LEED studies [104] of the phases of S on Ru(0001) and lattice gas simulations it is known that the diffusion barrier of S on Ru(0001) is very small, of the order of a few meV; thus, the mobility of isolated (2D gas like) S atoms is very high on Ru(0001) at room temperature. Therefore, we have here a case where S binds on Ru(0001) and then it is

trapped in the Ag vacancy and easily carried around by the relaxation process of the Ag film alone. From the phase diagram we know that the size of the Ag vacancy islands in dilute phase is independent of S coverage. Also, the size of the Ag vacancy island is a few times larger than the $p(2 \times 2)$ footprint of the average number of two sulfur atoms per vacancy only supports the fact that S atoms once adsorbed onto the Ru(0001) and trapped in the Ag vacancy are in a gas like phase. From the phase diagram of S/Ru(0001) as studied by LEED [104], $p(2 \times 2)$ is the only ordered (solid) structure that S forms below 0.25 ML coverage and at room temperature or below.

An intriguing aspect of the already discussed phase diagram – Fig. 4-6 (top) – is that Ag vacancy islands saturation density is exactly half the surface density of the threading dislocations of SHB of Ag/Ru(0001). This fact, along with the disappearance of the threading dislocations in the Ag film (Fig. 4-10), can happen if a pair of nearest neighbor threading dislocations of different orientations in the SHB film annihilate each other. Indeed, two dislocations with two opposing Burgers vectors will cancel each other [106].

A clear observation of the formation of Ag vacancy islands comes from STM data acquired at very low S coverage (1×10^{-3} ML) and low temperature (110 K). For such a low S coverage, isolated Ag vacancy islands are formed randomly on the Ag film. The dynamical processes of Ag vacancy island diffusion is slowed down at low temperature, thus preventing Ag vacancy islands clustering together. A snapshot of the nanometer sized features frozen in time, shown in Fig. 4-12, displays the main features of S filled Ag vacancy island creation. Indeed, the STM picture tells the story of dislocation annihilation yielding to the formation of the triangular lattices of Ag vacancy islands:

(a) Two S filled Ag vacancy islands seen as dark features.

(b) Blue and green T's pinpoint the positions of the threading dislocations, the two

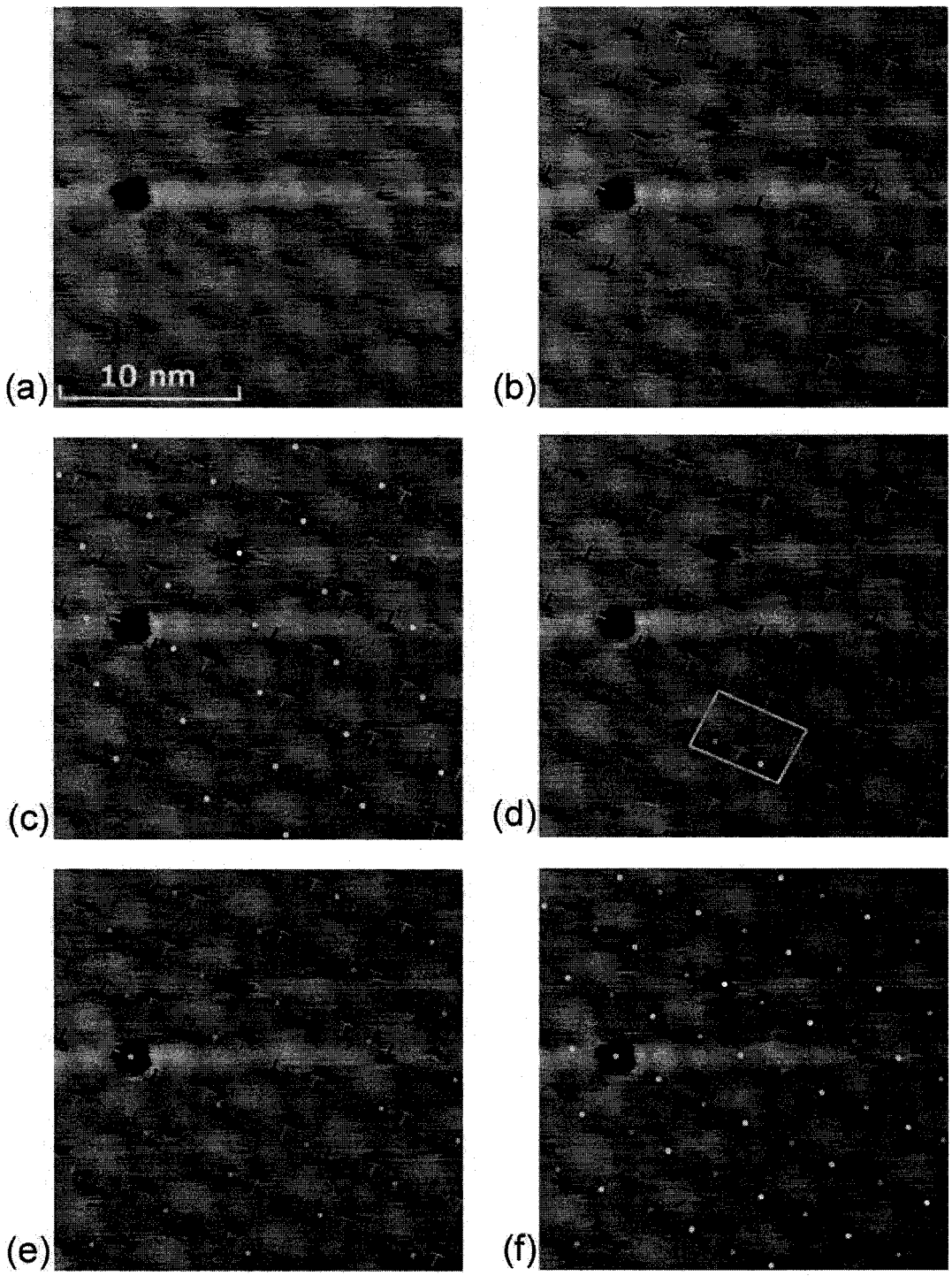

Fig. 4-12: 110 K STM data of SHB of Ag with two S filled Ag vacancy islands seen as dark features (about 1×10^{-3} ML of S). Dislocation annihilation yields to the formation of the triangular lattices of Ag vacancy islands marked with blue and yellow dots – see text for an explanation of the process.

extra pairs of T's around the two S-filled vacancy islands mark the extrapolated positions of the TD pairs on the unetched Ag film.

(c) The Ag vacancy island at the top of the image is located at the median distance between two neighboring and opposite TD's. A triangular array marked by yellow dots can be formed via a TD pair annihilation process.

(d) Blue and yellow dots mark two equivalent locations of a Ag vacancy island after S etching.

(e) The lower S filled Ag vacancy island rests on the triangular array of blue dots.

(f) Two triangular and complementary networks of blue and yellow dots can be extrapolated from the TD pair dislocation annihilation mechanism.

Until this moment we have found that the final state of the S/SHB of Ag/Ru(0001) is an ordered array of S filled vacancy islands with a triangular symmetry, different from the initial rectangular symmetry of SHB of Ag/Ru(0001). Also we have seen how the initial stages of creation of S filled Ag vacancy islands take place, with the possibility of having two intermixing arrays of S filled Ag vacancy islands (yellow and blue dots triangular lattices in Fig. 4-12f). The long range observed order of the islands can be reached only if the mobility of Ag vacancy islands is high enough at room temperature when S_2 deposition takes place. In this way, a vacancy island once randomly formed on one of the two possible triangular lattices can switch between the two lattices.

Indeed, a sequence of dynamical STM images taken at 295 K and low S coverage show that in the dilute phase, the Ag vacancy islands are hopping between neighboring etching positions. An example of such data is shown in Fig. 4-13. The islands diffuse randomly one dimensionally along the threading dislocation core lines, jumping between neighboring positions on the blue and yellow lattices (shown in Fig. 4-12) which are aligned along the

long side of the unit cell size shown in Fig. 4-9.

4.4 Theoretical model of the self–assembly of S filled Ag vacancy islands on the SHB network

4.4.1 Two–dimensional Frenkel–Kontorova model

Such networks of misfit dislocations can be understood in the framework of a two dimensional Frenkel–Kontorova model [36, 37, 88, 89, 90] where one has to consider the potential landscape of the surface seen by an adatom (U_{sub}) and the inter–adatom potential (U_{Ag-Ag}). The interactions within the adsorbate film and with the surface are then described by the Hamiltonian

$$H = U_{sub} + U_{Ag-Ag} + KE. \tag{4.5}$$

If we neglect the kinetic energy term, KE, we obtain the two dimensional Frenkel–Kontorova (2D–FK) Hamiltonian

$$H_{FK} = \sum_{\vec{r_i}} \sum_{\vec{g}} V_{\vec{g}} e^{i\vec{g}\cdot\vec{r_i}} + \frac{k}{2} \sum_{\vec{r_i}} \sum_{\vec{r_j} \neq \vec{r_i}} (|\vec{r_i} - \vec{r_j}| - b\, a_{Ru})^2, \tag{4.6}$$

where $\vec{r_i}$, $\vec{r_j}$ represent the atomic positions of adsorbate film, $V_{\vec{g}}$ are the coefficients of the surface potential expansion over $\vec{g}$, which are sets of reciprocal vectors of the substrate, k is the elastic constant of the Ag film, and $b = a_{Ag}/a_{Ru}$ is the lattice mismatch between Ag bulk lattice, a_{Ag}, and Ru bulk lattice, a_{Ru}.

The 2D–FK model requires a continuous surface potential seen by adatoms, the first term in Equation 4.6. The inputs for the surface potential calculation are the binding energies of Ag adatoms at high symmetry positions on the Ru(0001) surface. From first–principles

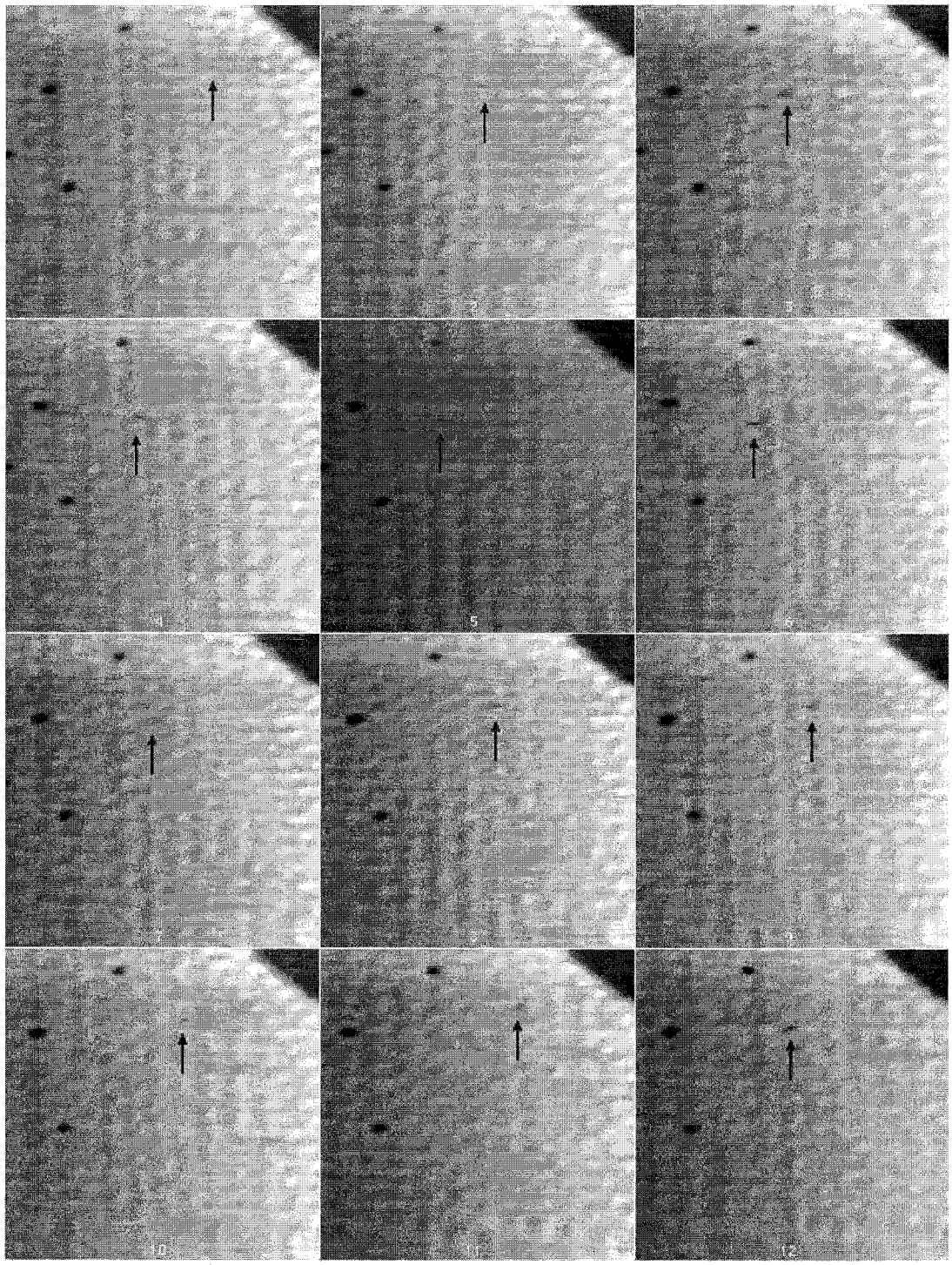

Fig. 4-13: Sequence of STM images showing the dynamics of S filled Ag vacancy islands. Each image was taken at 10 s apart at room temperature. The red arrow indicate the position of the mobile Ag vacancy which hops randomly parallel to the TD core direction.

calculations [91] we know the following binding energies:

$$\begin{aligned} E_t &= 282 \text{ meV for "on top" positions,} \\ E_b &= 55 \text{ meV for "bridge" positions, and} \\ E_h = E_f &= 0 \text{ for Ag atoms bond on FCC and HCP sites.} \end{aligned} \tag{4.7}$$

The order of magnitude of the elastic constant in the Ag–Ag film is given by the bulk elastic constant.

In order to use the symmetry of Ru(0001) in the process of computing the surface potential, I choose to expand it in the base of the reciprocal vectors

$$(\vec{A_1}, \vec{A_2}) = (\frac{4\pi}{\sqrt{3}a_{Ru}} \left[\frac{\sqrt{3}}{2}\hat{x} - \frac{1}{2}\hat{y} \right], \frac{4\pi}{\sqrt{3}a_{Ru}}\hat{y}) \tag{4.8}$$

and

$$(\vec{C_1}, \vec{C_2}) = (\frac{4\pi}{a_{Ru}}\hat{x}, \frac{4\pi}{a_{Ru}} \left[-\frac{1}{2}\hat{x} + \frac{\sqrt{3}}{2}\hat{y} \right]) \tag{4.9}$$

corresponding to the families of planes in the real space defined by the direction normal to the surface and the following surface vectors

$$(\vec{a_1}, \vec{a_2}) = (a_{Ru}\hat{x}, \frac{1}{2}a_{Ru}\hat{x} + \frac{\sqrt{3}}{2}a_{Ru}\hat{y}) \tag{4.10}$$

and

$$(\vec{c_1}, \vec{c_2}) = (\frac{1}{2}a_{Ru}\hat{x} + \frac{1}{2\sqrt{3}}a_{Ru}\hat{y}, \frac{\sqrt{3}}{2}a_{Ru}\hat{y}) \tag{4.11}$$

which are drawn in Fig. 4-14.

I can now express the surface potential as:

$$U_{sub}(\vec{r}) = V_0 + \sum_{\{\vec{g_1}\}} V_{g_1} e^{i\vec{g_1}\cdot\vec{r}} + \sum_{\{\vec{g_2}\}} V_{g_2} e^{i\vec{g_2}\cdot\vec{r}} \tag{4.12}$$

where I have used the notations:

$$\{\vec{g_1}\} = \{\vec{A_1}, \vec{A_2}, -\vec{A_1}, -\vec{A_2}, \vec{A_1} + \vec{A_2}, -\vec{A_1} - \vec{A_2}\} \tag{4.13}$$

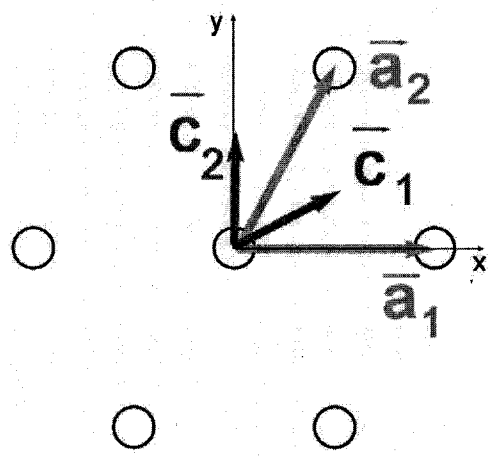

Fig. 4-14: Ru(0001) surface schematics with the real lattice vector pairs ($\vec{a_1}$, $\vec{a_2}$) and ($\vec{c_1}$, $\vec{c_2}$) corresponding to the reciprocal vectors ($\vec{A}_1$, $\vec{A}_2$) and ($\vec{C}_1$, $\vec{C}_2$) used for surface potential expansion.

and

$$\{\vec{g_2}\} = \{\vec{C}_1, \vec{C}_2, -\vec{C}_1, -\vec{C}_2, \vec{C}_1 + \vec{C}_2, -\vec{C}_1 - \vec{C}_2\}. \tag{4.14}$$

For a Ag adatom sitting in the "on top" position

$$\vec{r}_t = 0, \tag{4.15}$$

therefore

$$U_{sub}(\vec{r}_t) = V_0 + 6V_{g_1} + 6V_{g_2} = E_t. \tag{4.16}$$

For a Ag atom sitting in a bridge site

$$\vec{r}_b = \frac{1}{2}\vec{a_1} = \frac{1}{2}a_{Ru}\hat{x}; \tag{4.17}$$

hence, the surface potential energy at that location is

$$U_{sub}(\vec{r}_b) = V_0 - 2V_{g_1} - 2V_{g_2} = E_b. \tag{4.18}$$

In the same way, for an atom sitting in a FCC location

$$\vec{r}_{FCC} = \frac{a_{Ru}}{\sqrt{3}}\hat{y}, \tag{4.19}$$

the surface energy is

$$U_{sub}(\vec{r}_{FCC}) = V_0 - 3V_{g_1} + 6V_{g_2} = E_{FCC} = E_{HCP}. \tag{4.20}$$

Solving the Equations 4.16, 4.18, and 4.20 for V_0, V_{g_1} and V_{g_2} we obtain the coefficients of surface potential expansion:

$$V_0 = \frac{1}{4}E_t + \frac{3}{4}E_b; \tag{4.21}$$

$$V_{g_1} = \frac{1}{9}E_t - \frac{1}{9}E_{FCC}; \tag{4.22}$$

$$V_{g_2} = \frac{1}{72}E_t - \frac{1}{8}E_b + \frac{1}{9}E_{FCC}. \tag{4.23}$$

For an arbitrary position on the surface, $\vec{r} = r_x\hat{x} + r_y\hat{y}$, the potential landscape of the surface is given by the following relation:

$$\begin{aligned} U_{sub}(\vec{r}) = V_0 &+ 2V_{g_1}\cos\left[\frac{4\pi}{\sqrt{3}a_{Ru}}\left(\frac{\sqrt{3}}{2}r_x - \frac{1}{2}r_y\right)\right] + 2V_{g_1}\cos\left[\frac{4\pi}{\sqrt{3}a_{Ru}}r_y\right] \\ &+2V_{g_1}\cos\left[\frac{4\pi}{\sqrt{3}a_{Ru}}\left(\frac{\sqrt{3}}{2}r_x + \frac{1}{2}r_y\right)\right] + 2V_{g_2}\cos\left[\frac{4\pi}{a_{Ru}}r_x\right] \\ &+2V_{g_2}\cos\left[\frac{4\pi}{a_{Ru}}\left(-\frac{1}{2}r_x + \frac{\sqrt{3}}{2}r_y\right)\right] + 2V_{g_2}\cos\left[\frac{4\pi}{a_{Ru}}\left(\frac{1}{2}r_x + \frac{\sqrt{3}}{2}r_y\right)\right]. \end{aligned} \tag{4.24}$$

The surface potential calculated with Equation 4.24 is shown in Fig. 4-15, with the expansion coefficients V_0, V_{g_1}, and V_{g_2} computed from Equations 4.21, 4.22, and 4.22 for the first principles values of the binding energy of Ag on the high symmetry points of Ru(0001), $E_t = 282$ meV, $E_b = 55$ meV, and $E_{FCC} = E_{HCP} = 0$ [91].

The total energy of the 2D–FK model system (Equation 4.6 with the first term calculated from Equation 4.24) can be minimized numerically for appropriate boundary conditions, density of the adsorbate layer, and strength of the Ag–Ag interaction, k, to obtain the ground state solution. The numerical algorithms I wrote to solve this problem, start by generating a pseudomorphic adlayer on Ru(0001) then apply the periodic boundary conditions as described in the next paragraphs and minimizes the total energy of the adlayer

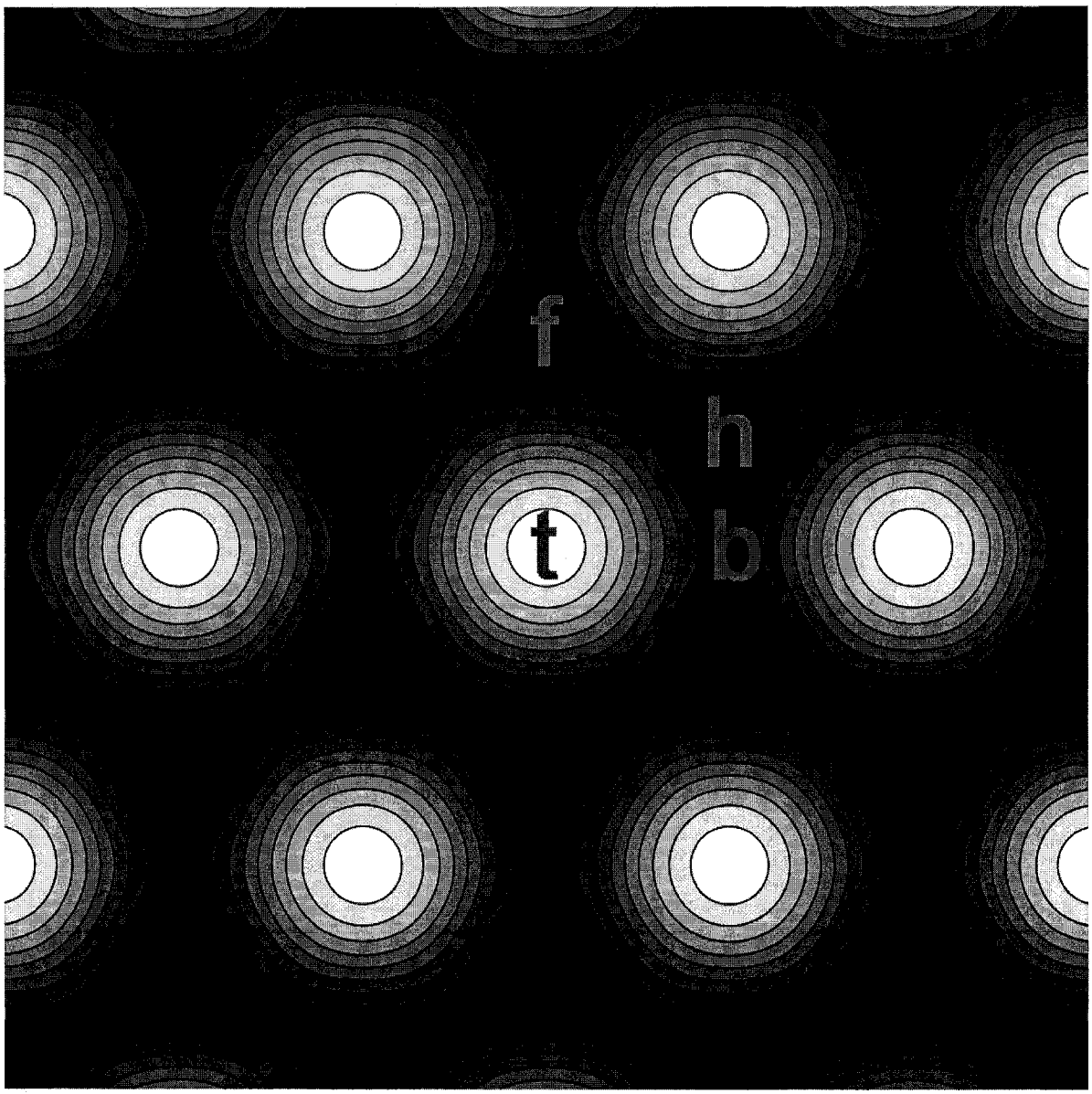

Fig. 4-15: Plot of the surface potential calculated with Eqn. 4.24. First principles values of the binding energies of Ag on Ru(0001) at the high symmetry points marked in the picture; $E_t = 282$ meV (top), $E_b = 55$ meV (bridge), and $E_h = E_f = 0$ (HCP and FCC sites) have been used [91].

film by employing a global minimization method. I used both the steepest descent and Monte Carlo method to find the minimum energy configuration to compare the results for consistency. Once both minimization methods produced similar results for identical input

parameters and geometry henceforth the analytic method was used.

4.4.2 SHB reconstruction

Experimentally we have already seen what are the main features of SHB reconstruction. Stripe type features with alternating FCC and HCP stacking which join forming a Shockley partial dislocation are running along compact directions of the Ru(0001) surface. When two of these partial dislocations meet, a screw dislocation, perpendicular to the surface, is formed. We also know from experiment that the SHB dislocation network has rectangular symmetry, with a unit cell of 18 (19) $\times$ 15(16) Ag atoms. Based on this experimental input, the 2D–FK model generates the SHB network by starting with a pseudomorphic Ag film, followed by removing atoms as shown in Fig. 4-16 for a unit cell size of 18 $\times$ 15 Ag atoms. The places from which Ag atoms are removed are going to be the locations of the Shockley partial dislocations and at the "elbow" sites they are going to form the cores of the threading dislocations. The following step is to reform the atomic bonds between the Ag atoms around the locations where atoms have been removed followed by the last step of energy minimization of the whole system. This bond formation process rebuilds a hexagonal lattice of bonds everywhere with the exception of the "elbows" locations where at least two of the Ag atoms will be able to accommodate only 5 nearest neighbors bonds.

The result of such a simulation is shown in Fig. 4-17 which closely describes the low temperature STM measurement in Fig. 4-8b. The interaction parameters used as an input are the ones obtained from first–principles calculation for the surface potential, with their values given by the relations 4.7.

A measure of the overall relaxation in the process of formation of the misfit dislocation network is the average energy gain per adatom defined with respect to the pseudomorphic

film

$$\Delta E_{1\times1} = E_{1\times1\ pseudomorphic} - E_{1\times1\ SHB}. \tag{4.25}$$

Thus, for the Ag–Ag interaction parameters $k = 2000$ meV/Å^2 and $b = a_{Ag}/a_{Ru} = 1.14$ used to generate the SHB structure of Fig. 4-17, $\Delta E_{1\times1}$ obtained is about 255 meV. This value is quite large, especially when compared with the "on top" binding energy of one Ag atom on Ru(0001) which is $E_t = 282$ meV.

At close inspection of the SHB network (Fig. 4-18), we see that there are two types of Shockley partial dislocations. The yellow line shows the orientation of the first Shockley

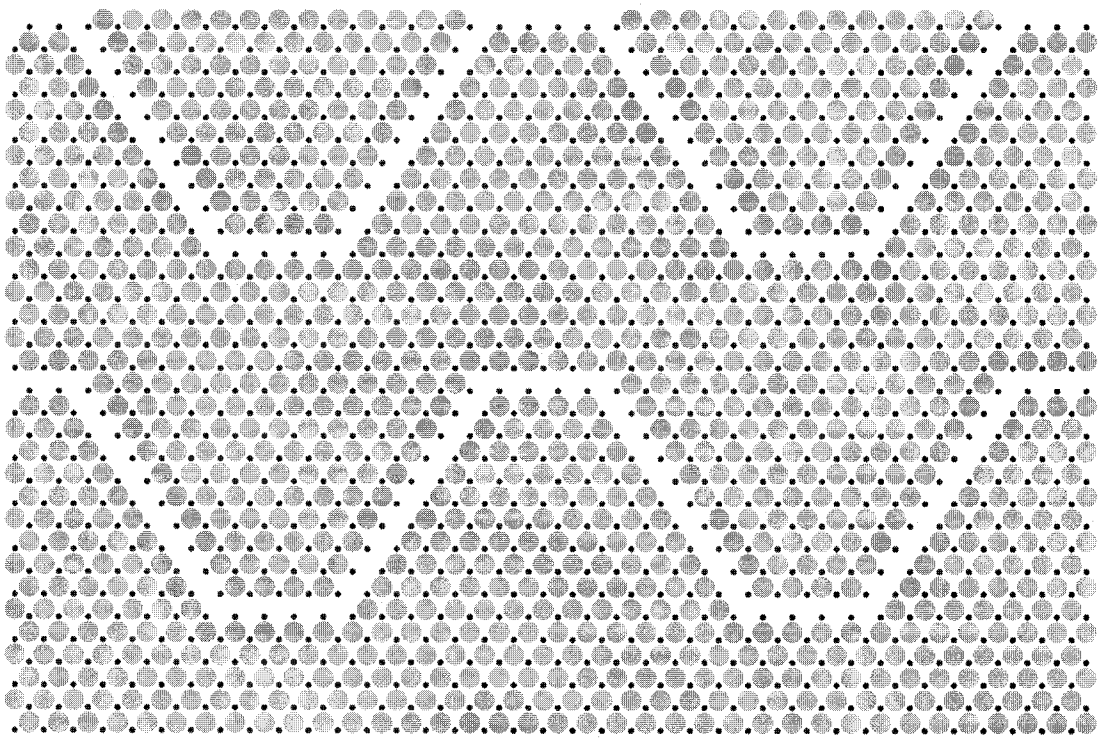

Fig. 4-16: Periodic conditions generating the SHB misfit dislocation network with the unit cell size of the reconstruction of 18 × 15 Ag atoms. Red dots mark the positions of the underlying Ru(0001) substrate while the blue dots show the locations of pseudomorphic Ag atoms.

partial dislocation line which follows the direction between two threading dislocation cores. It fills the line of removed Ag atoms in Fig. 4-16. The stripe type area marked with the red rectangle 3, shows that Ag atoms have two different stacking positions, "a" and "b", (FCC or HCP stacking), the transition gradually taking place from one stacking to the other as moving perpendicular to the yellow dislocation line. The second type of Shockley partial

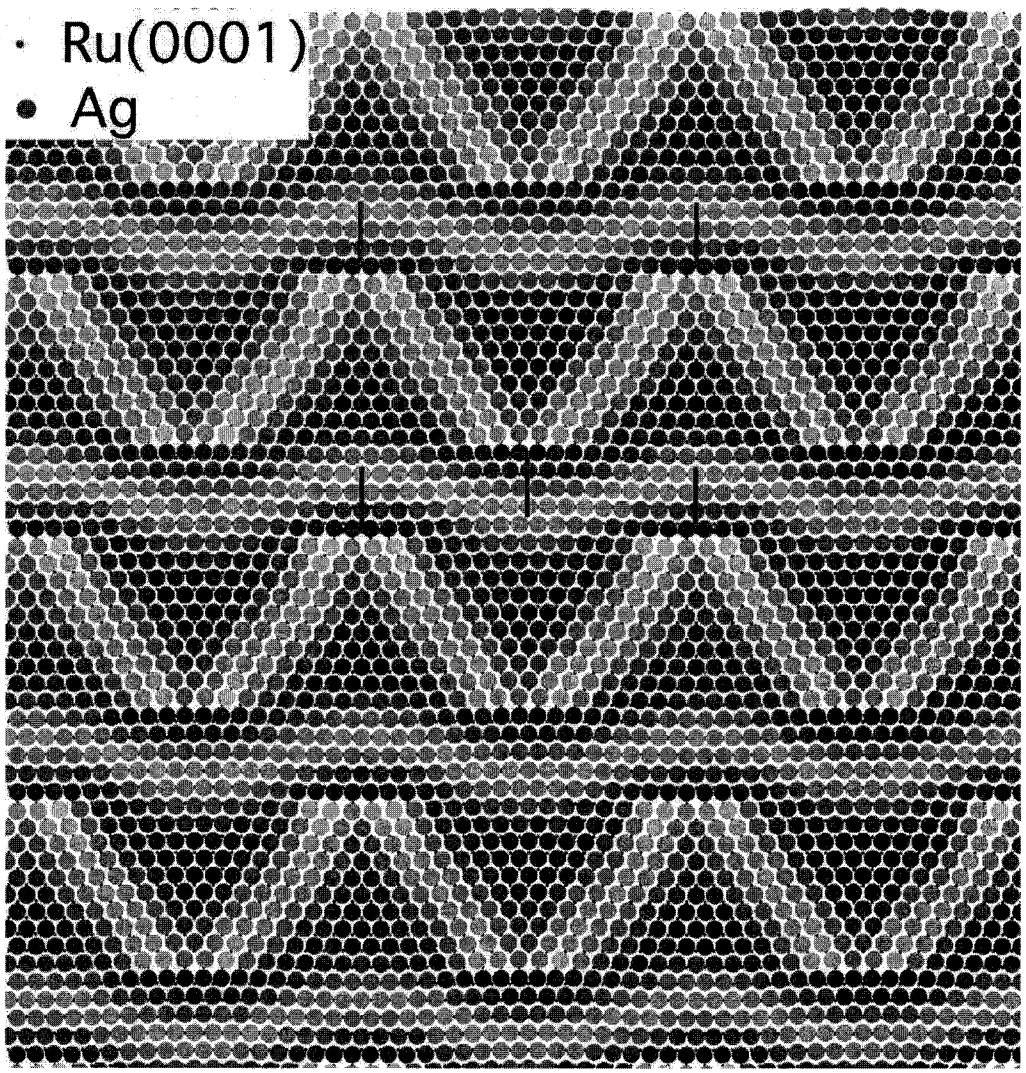

Fig. 4-17: 2D Frenkel–Kontorova model of the misfit dislocation network of the SHB structure. Red T's mark the locations of the threading dislocation cores in one unit cell. Ag–Ag interaction parameters are the elastic constant of the Ag film, $k = 2000$ meV/Å^2 and the lattice mismatch $b = a_{Ag}/a_{Ru} = 1.14$.

dislocation is marked with the orange line. It does not follow a specific orientation, but wiggles between the threading dislocation cores, this being very specific to the SHB network. Also, in the same Fig. 4-18 we see that there are two types of threading dislocation cores, each circled with a red Burgers vector circuit. The difference between these two threading cores is the different stacking at the core line, represented by the whiter, horizontally expanded line of Ag atoms. Thus, the first TD core has a "a" type stacking while the second

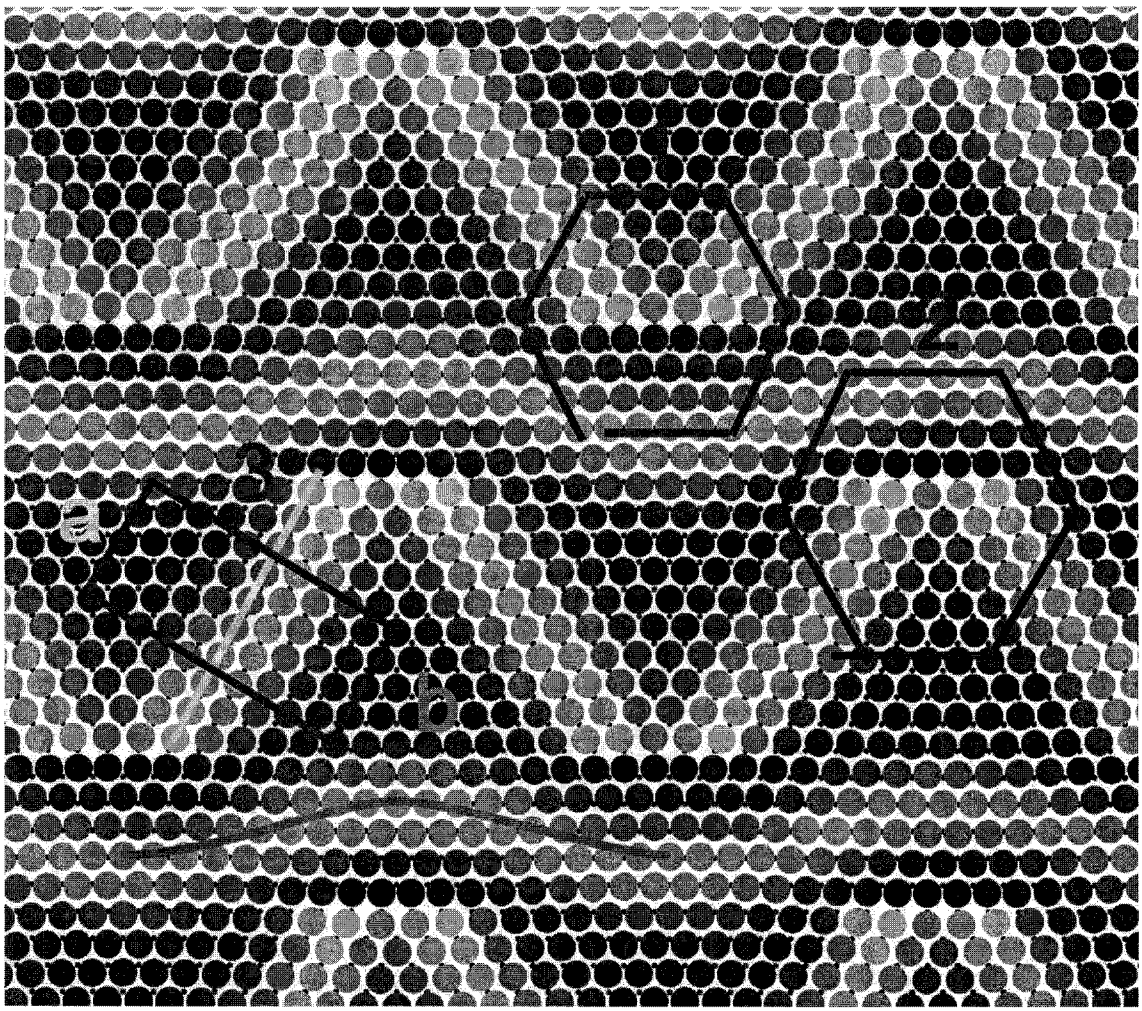

Fig. 4-18: Atomic structure of the SHB misfit dislocation network. Burgers vector circuits are shown around the two different threading dislocation cores 1 and 2. The yellow and the orange curves show the location of two different Shockley partial dislocation lines. "a" and "b" mark the two different stacking geometries of the Ag film.

core has a "b" type stacking.

4.4.3 Ag vacancy island creation

The initial stages of the self–assembly process are seen experimentally as the creation of isolated S filled Ag vacancy islands with a characteristic 1.5 nm^2 area. Also, these isolated vacancy islands are very mobile at room temperature; they are randomly moving in a one dimensional fashion on the SHB network as seen in Fig. 4-13. The hopping direction is parallel to the longer side of the rectangular unit cell of the SHB network, along the nearest neighbor positions resulted from the annihilation of pairs of threading dislocation cores.

In the 2D–FK model, such a Ag vacancy island formation is shown in Fig. 4-19 for the SHB misfit dislocation network presented in Fig. 4-17. The numerical procedure to generate these vacancy islands goes through the following steps: (a) a SHB network is created followed by (b) the removal of Ag atoms to create a vacancy in the Ag film and then (c) the system is relaxed to the minimum global energy.

In order to significantly lower the overall energy of the Ag structure, a certain number of Ag atoms need to be removed around the suggested experimental etching position, at the median distance between a pair of threading dislocations. The average energy gain per Ag atom is defined as

$$\Delta E_{1S\ 1\times1} = E_{1\times1\ SHB} - E_{1\times1\ 1S\ island}, \tag{4.26}$$

where $E_{1\times1\ 1S\ island}$ is the average energy per Ag atom in the SHB unit cell surrounding the Ag vacancy island. Thus, for the results shown in Fig. 4-19, $\Delta E_{1S\ 1\times1} = 50$ meV.

An inspection of Fig. 4-19 shows why this is the case. In order to lift off a pair of threading dislocations as indicated by experiment, a large enough Ag vacancy island must be created such that the island completely removes the extra row of 5 Ag atoms marked

with the red line in the figure. In that area, along the wiggled Shockley partial dislocation, the Ag film is in a compressed state, the average distance between two neighboring Ag atoms being smaller than in any other regions of the Ag film. Interestingly, creating a Ag vacancy island stretching enough to remove the extra 5 atoms results in a Ag vacancy island area of 1.44 nm^2, very close to the experimental value of 1.5 nm^2.

The diffusion of the Ag vacancy island to the nearest position marked with "a" in Fig. 4-19 is easier than the diffusion to the "b" marked position since in the first case, the local density of Ag atoms around the vacancy island does not change, the movement being just a glide of the vacancy with a conservation of the local number of bonds.

4.4.4 Ag vacancy islands array formation

The experimental data shows that S filled Ag vacancy islands grow in clusters of nearest neighbor vacancy islands and as the S coverage increases, a complete array of vacancy islands form. The process of clustering of two or more Ag vacancy islands implies that a lowering of the total energy of the system takes place.

The question then is whether the 2D–FK model can account for this fact. Fig. 4-20 shows the result of the 2D–FK elastic model for the creation of a second Ag vacancy islands in the proximity of the first one. The average energy gain per Ag atom in the process of forming a second Ag vacancy island at a nearest neighbor position with respect to the first Ag vacancy island is defined as

$$\Delta E_{2S\ 1\times1} = E_{1\times1\ 1S\ island} - E_{1\times1\ 1+1S\ island}, \tag{4.27}$$

where $E_{1\times1\ 1+1S\ island}$ is the average energy per Ag atom in the unit cell surrounding the first Ag vacancy island after the creation of the second neighboring vacancy island.

For the results shown in Fig. 4-20, $E_{1\times1\ 1+1S\ island} = 26$ meV. The 2D–FK elastic model

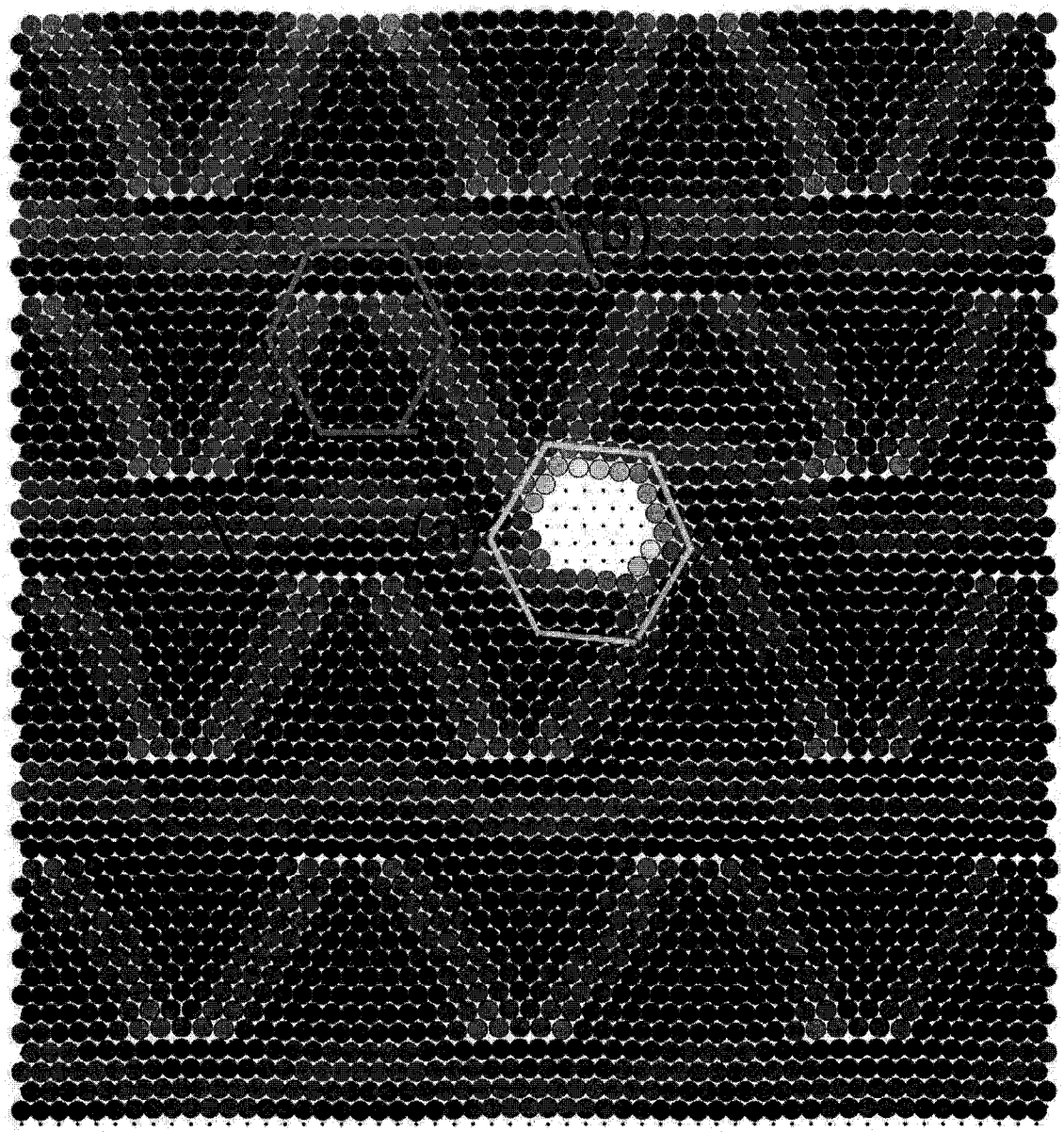

Fig. 4-19: 2D FK model of the creation of one S filled Ag vacancy island for the interaction parameters employed to generate Fig. 4-17. The size of the vacancy shown is given by the minimum number of removed Ag atoms required to lift off the threading dislocation; the yellow Burger circuit is closed showing no extra row of atoms as seen in the green Burger circuit.

does give a reduction of the total energy in the system composed of two neighboring islands. The corrugation around these two Ag vacancy islands does not look very symmetrical and I assume this comes from the fact that the 2D–FK elastic model does not allow for Ag

bonds to break and reform, which would allow for greater flexibility in reaching the most equilibrated state.

A sequence describing the steps through which the self–assembly process of S filled Ag vacancy islands on the SHB network evolves from separated individual vacancy islands to an complete and ordered array is shown in Fig. 4-21. At very low S coverage, isolated vacancy islands form Fig. 4-21a. As new vacancy islands are formed, they diffuse across the Ag film, and when they meet, they form more stable configurations (Fig. 4-21b and Fig. 4-21c). In this process, Shockley partial dislocations between the vacancy islands arrange such that

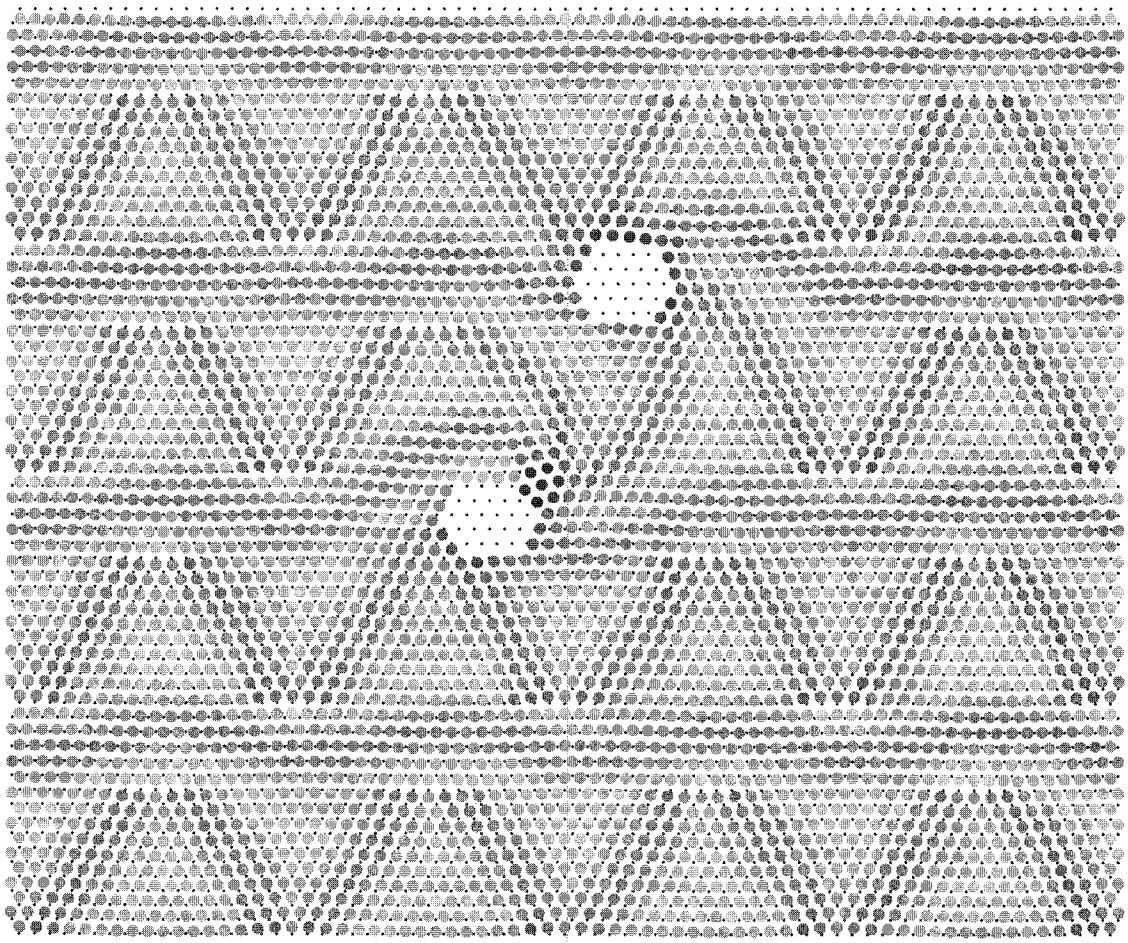

Fig. 4-20: 2D FK model of the creation of two Ag vacancy islands for the interaction parameters employed to generate Fig. 4-17.

they form triangles with the vacancy islands located at their corners. This self–assembly process continues with the growth of ordered clusters of vacancy islands (dilute phase) until a complete array of vacancy islands is formed (solid phase) as represented in Fig. 4-21c.

Such a mechanism generates naturally the new symmetry and also fulfills the other experimental observations, (i) the conservation of the unit cell area of 21.4 nm^2 for Ag/Ru(0001) vs. 21.6 nm^2 for S/Ag/Ru(0001), (ii) the 2 to 1 ratio of TD's and Ag vacancies, and (iii) the area of the S-filled vacancy island of 1.44 nm^2 in the FK model vs. 1.5 nm^2 from STM data.

4.5 Conclusions

The uniqueness of this process is that it merges experimental and theoretical models, showing unambiguously that the relaxation in the strained metallic Ag film, triggered by S_2 adsorption, is the driving force of the self–assembly. A detailed description of the self–assembly process as seen by experiment can be explained via an atomistic model based on first–principles interaction parameters. After S_2 adsorbtion creates a S filled Ag vacancy island, the relaxation of the SHB network of Ag proceeds via a threading dislocation pair annihilation process. Independently formed Ag vacancy islands are then diffusing along the surface and when they meet they form ordered clusters of vacancy islands. As the S coverage increases, the clusters of Ag vacancy islands grow until a complete and ordered array of vacancy islands is formed. The only requirements for this process are that the adsorbed specie (S) is immiscible in the surface layer with the thin strained metal film (Ag) and has a stronger binding energy on the supporting surface (Ru(0001)) than on the thin metallic film. As such, I expect this self–assembly mechanism to be a general one, applicable to systems fulfilling these conditions.

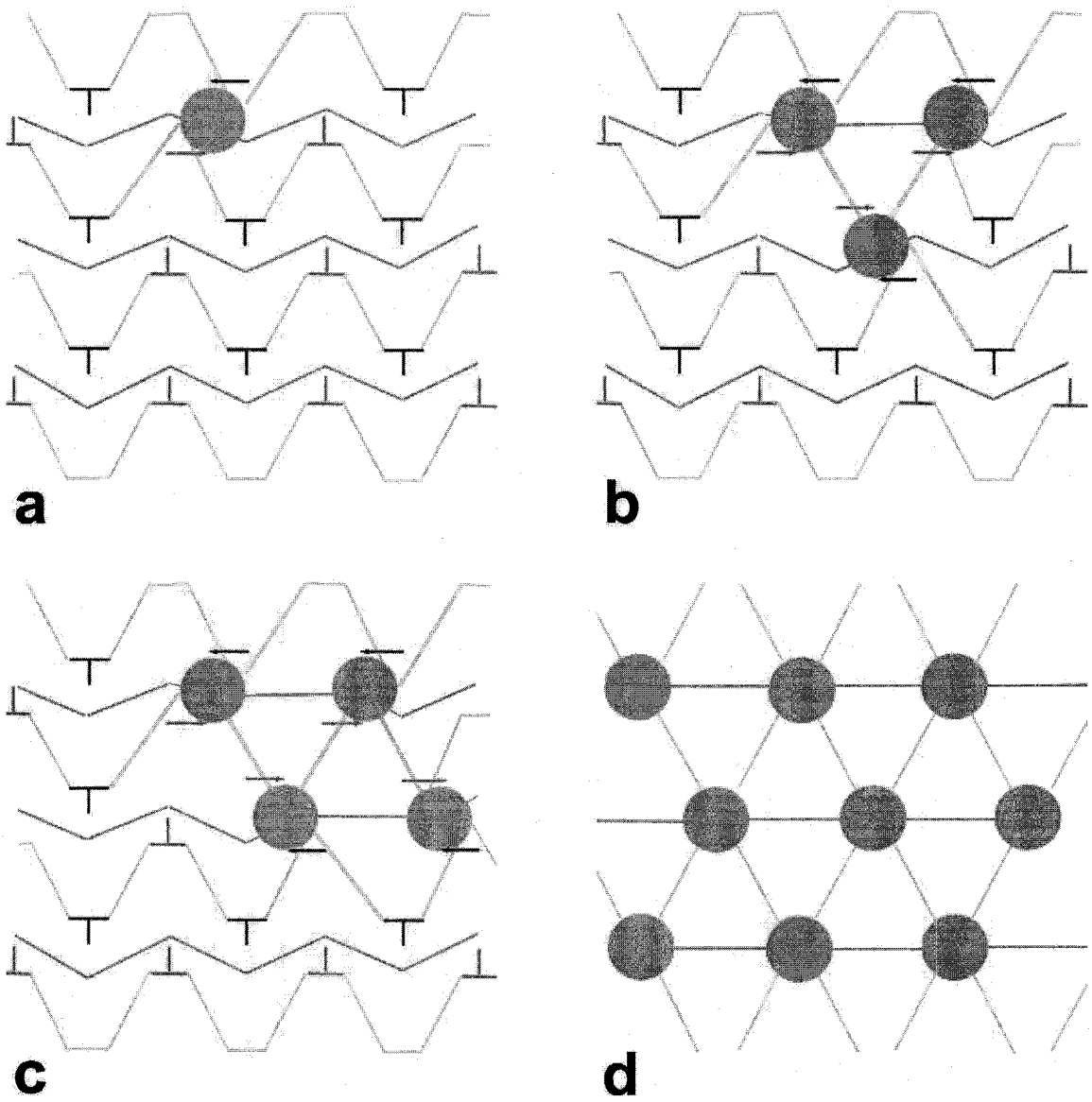

Fig. 4-21: Glide of Shockley partial dislocations resulting in the formation of a hexagonal pattern of S filled Ag vacancy islands.

Chapter 5

Acoustic Surface Plasmon on Be(0001)

5.1 Introduction

Nearly two-dimensional metallic systems formed in charge inversion layers [64] and artificial layered materials [65, 72] permit the existence of low-energy collective excitations [63, 66], so-called 2D plasmons, which are not found in a three-dimensional metal. These excitations have caused considerable interest because their low energy allows them to participate in many dynamical processes involving electrons and phonons [72] and as possible candidates to mediate the attractive interaction responsible for the formation of Cooper pairs in high T_c superconductors [73]. Metals often support electronic states that are confined to the surface forming a nearly 2D electron density layer. However, it was argued that these systems could not support low-energy collective excitations because these would be screened out by the underlying bulk electrons [67]. In fact, metallic surfaces should only support the conventional surface plasmons [53], modes with energies of a few eV, depending only on the electron density, with important applications in surface-plasmon resonance microscopy [59, 107], photonics and sub-wavelength optics [61, 62, 60], but no relevance to the low-energy dynamics. Here we show that, in contrast to this well-established belief, a low-

energy collective excitation mode can be found on bare metal surfaces. The mode has an acoustic (linear) dispersion, different from the $q_{\|}^{1/2}$ dispersion of a 2D plasmon, and was observed on Be(0001) using angle-resolved electron energy loss spectroscopy. First-principles calculations show that it is caused by the coexistence of a partially occupied quasi 2D surface-state band with the underlying 3D bulk electron continuum and that the non-local character of the dielectric function prevents it from being screened out by the 3D states. Its dispersion is mainly determined by the surface-state Fermi velocity, v_F^{2D}, and follows closely the upper edge of the continuum for electron-hole pair excitations within the surface-state band. While for Be(0001) a high value of v_F^{2D} warrants plasmon's excitation at higher than 1 eV, thus facilitating its observation, the mode as such has a very general character. The acoustic plasmon reported here should be present on many metal surfaces, profoundly affecting their electron and phonon dynamics. Furthermore, the new mode with its acoustic dispersion can allow confinement of light on small surface areas and in a broad frequency range thus being relevant for sub–wavelength optics and photonics applications.

5.2 Experimental procedures and measurements

5.2.1 EELS measurements

I performed the experiment in the group of Prof. Mario Rocca, University of Genoa, Italy with an ultra high vacuum apparatus at a base pressure of about 2×10^{-10} mbar equipped with an angle-resolved high resolution electron energy loss (EEL) spectrometer [108]. In most of the measurements the energy resolution was set to about 16 meV.

The single crystal Be sample was cut and mechanically polished along the (0001) plane. It was cleaned through repeated 0.5 to 1 keV Ne^+ sputtering cycles with the sample at

450 °C followed by annealing periods at 500 °C until the amount of oxygen on the surface was below the sensitivity threshold of Auger electron spectroscopy and a fairly sharp low energy electron diffraction pattern was obtained. At this stage EEL spectra still showed the presence of oxygen on the sample, characterized by losses at 80 and 120 meV. Further cleaning resulted in a reduction of the oxygen loss intensity until reaching the threshold of about 0.3% of the elastic peak in specular geometry when further improvement was no longer possible. The detected trace amounts of oxygen, estimated to be around 2% of a monolayer, did not increase significantly after hours of measurements.

All experiments were performed at room temperature. Fig. 5-2 shows typical angle-resolved EEL spectra taken along the $\bar{\Gamma}$-$\bar{M}$ direction (Figure 5-1) and for positive values of the momentum transfer parallel to the surface, $q_{\|}$ (Figure 5-3). A broad peak is observed to disperse as a function of $q_{\|}$ with another non-dispersing loss peak due to traces of oxygen contaminants. The energy loss of the dispersing peak was determined via a multi peak fitting procedure. The corresponding $q_{\|}$ was then calculated from energy and momentum conservation.

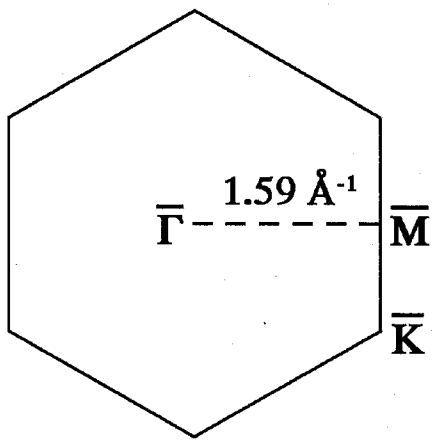

Figure 5-1: Surface Brillouin zone of Be(0001).

5.2.2 Extraction of the experimental dispersion

The conservation of energy and momentum for incident and scattered electrons was used in order to extract the dispersion of the reported acoustic surface plasmon (ASP). From the kinematics of the scattering process we have for the electron momentum transfer parallel to the surface:

$$q_{\parallel} = \frac{\sqrt{2m}}{\hbar}\left(\sqrt{E_i}\sin\theta_i - \sqrt{E_i - E_{loss}}\sin\theta_s\right), \tag{5.1}$$

where E_i ($E_s = E_i - E_{loss}$) and θ_i (θ_s) are the incident (scattered) energy and angle of the incident (scattered) electron, and the energy loss for the ASP, E_{loss}, is taken from individual electron energy loss (EEL) spectra.

In order to obtain E_{loss} from the experimental data, a deconvolution of various energy losses is needed, especially at low excitation energy where the overlapping of the peaks prevents one from measuring it directly.

For example, Figure 5-4 shows the convolution (green line) of the fit functions along with the EEL spectrum corresponding to $E_i = 7.26$ eV, $\theta_i = 66.8°$, and $\theta_s = 63.3°$ (black line). The elastic peak and the Rayleigh wave peak [109] are fitted with Lorentzian functions while for the fit of the oxygen loss at 120 meV and the ASP mode (main Figure 5-4) a Lorentzian and a broad Gaussian function have been used. The overall quality of the fit was used to estimate the error bars of E_{loss} by mildly changing the parameters of the Gaussian used to fit the ASP mode and the width of the Lorentzian used for oxygen loss while keeping all other fit functions at their best fit parameters. In this way an error bar of ± 50 meV or less was found.

The finite angular acceptance of the instrument α translates in a finite integration

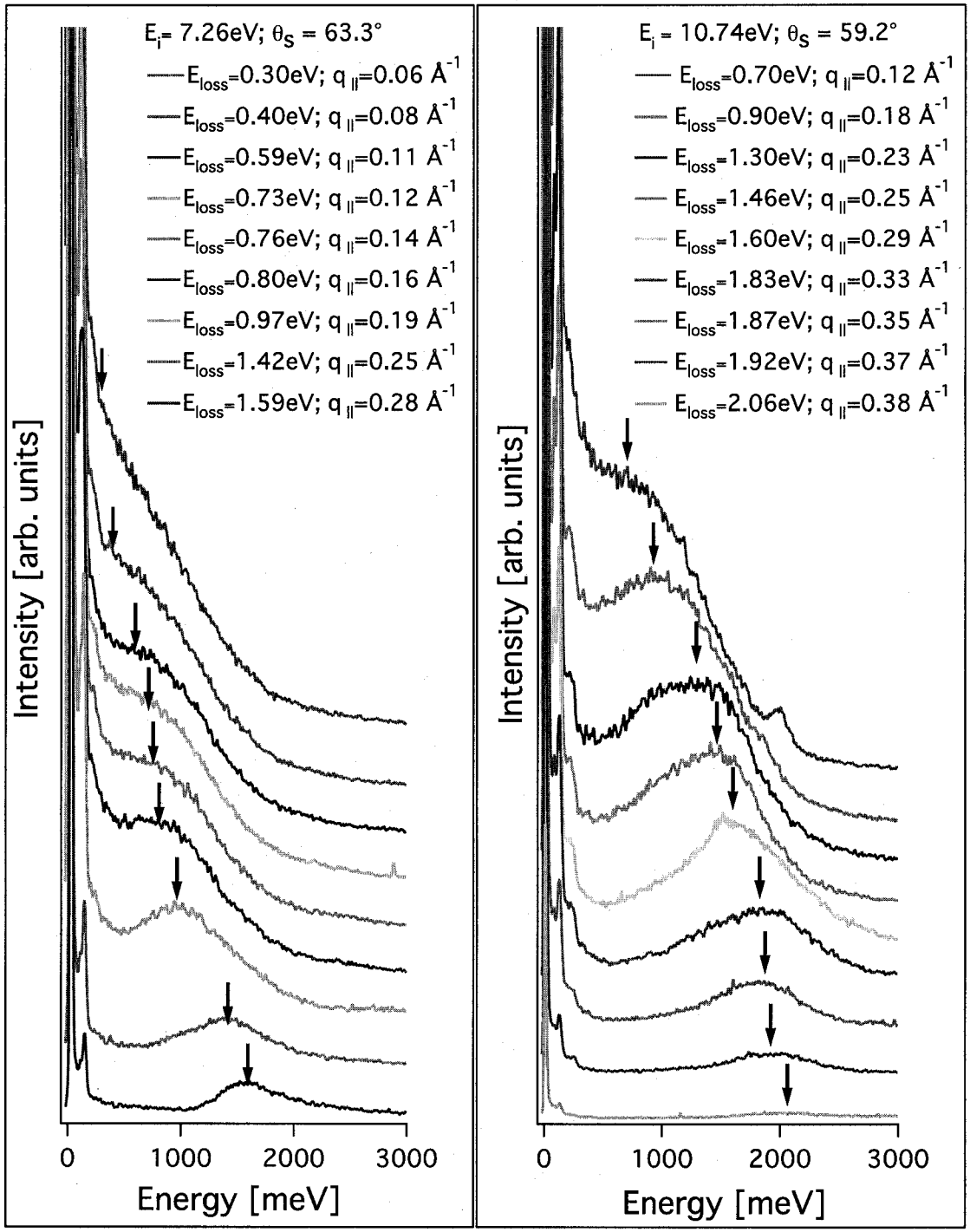

Figure 5-2: Families of Angle-Resolved EEL spectra taken at room temperature in the $\bar{\Gamma}$-$\bar{M}$ direction for two electron incident energies E_i and emergent scattering angles θ_s. The instrument employed a fixed analyzer angle θ_s with a variable incident electron beam angle θ_i[108]. Each spectrum corresponds to a different electron momentum transfer component parallel to the surface $q_{\|}$. The spectra have been evenly spaced vertically for clarity. The additional, non dispersing, low frequency loss is due to the residual oxygen contamination. The arrows mark the position of the maxima obtained via the fitting procedure described in the text.

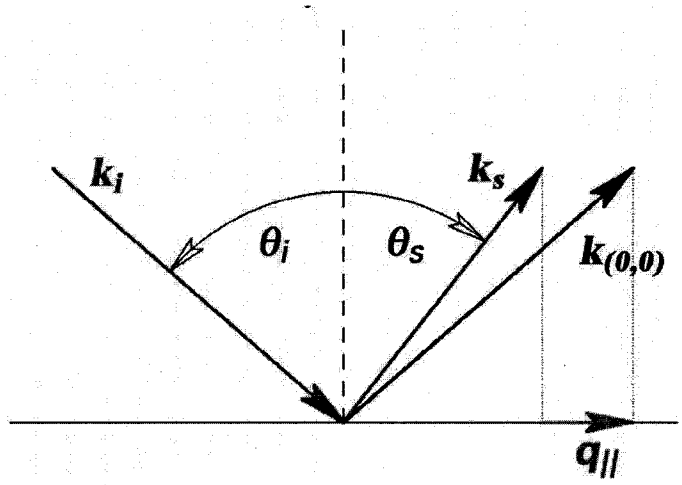

Figure 5-3: EEL measurements scattering geometry.

window over momentum space [58]

$$\Delta q_{\|} = \frac{\sqrt{2m}}{\hbar}\left(\sqrt{E_i}\cos\theta_i + \sqrt{E_i - E_{loss}}\cos\theta_s\right)\alpha, \tag{5.2}$$

which limits the experimental accuracy of $q_{\|}$. The last relation was used to compute the error bars of the momentum transfer parallel to the surface for an angular acceptance of the instrument of 6°. The broad shape of the measured ASP mode is a conjugate effect of the angular acceptance of the instrument, the acoustic behavior of the ASP dispersion and the fact that an EEL spectrometer collects electrons in an energy range corresponding to the crossing of the scan line and the dispersion line as shown in the inset in Fig. 5-4.

The inset figure shows the theoretical dispersion (red line) overlapping with the energy–momentum range of electrons collected by the EEL spectrometer (black lines) corresponding to the spectrum shown in the figure and the integration window over momentum space determined by the angular acceptance of the electron optics (6° FWHM). Integration over momentum and energy loss are linked by the dispersion of the ASP mode. The measured width of the latter is thus only marginally due to its intrinsic damping. The triangular shaped loss at small momentum transfers bears the same origin and is a signature for

the acoustic nature of the loss. This fit procedure determines then only the highest loss probability, corresponding to inelastic electrons entering the analyzer at small angles around the central trajectory.

The so determined experimental dispersion is shown in Fig. 5-5. It is clearly not affected by changes in the scattering geometry and/or in incident energy of the electron beam. In the long-wavelength limit, the energy of the new mode is found to approach zero linearly for vanishing values of the momentum component parallel to the surface. These data clearly show the acoustic character of this excitation within the limits of the experimental errors. In this experiment I have probed the surface at low $q_{\|}$ values of the first surface Brillouin zone (Fig. 5-1 and Fig. 5-5).

I have tried to probe the new acoustic excitation for positive and negative $q_{\|}$. All the data shown are for positive momentum transfer. In the negative momentum transfer spectra there is no well defined energy loss and that is presumably related to the narrow dipole lobe resulting in a low excitation probability [58].

5.2.3 Oxygen influence on the Acoustic Surface Plasmon

We have checked the effect of oxygen contamination on the Be acoustic surface plasmon and on its dispersion by recording EEL spectra for different oxygen exposures. As shown in the left panel of Figure 5-6, under the experimental conditions corresponding to the data reported in the paper, the EEL spectra show two losses at 80 meV and 120 meV assigned to vibrational modes of oxygen on Be(0001) [110]. Their intensity reads approximately 0.3% of the elastic peak height when measuring in-specular, at an impact energy of 7.07 eV and 64° incidence. The corresponding Be ASP loss region shows a maximum at 1.48 eV for $q_{\|} = 0.22$ Å^{-1} (right panel of Figure 5-6, blue curve, after smoothing the raw data

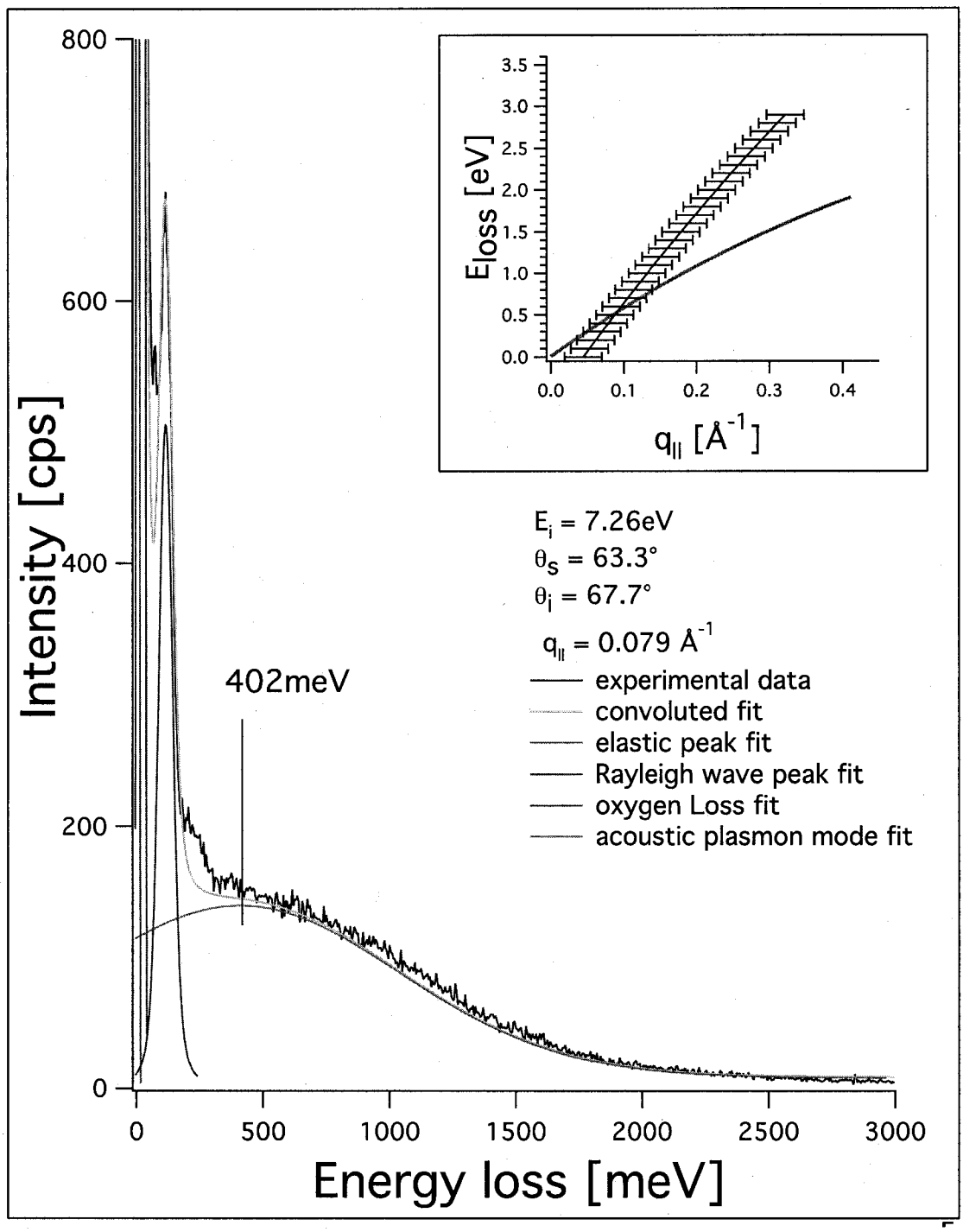

Figure 5-4: Extraction of the energy loss of the ASP mode, E_{loss}, from experimental EEL spectra. A four peak fit was used to find ASP maxima from the convoluted experimental data of the elastic peak, the loss corresponding to the Rayleigh wave [109], the oxygen loss at 120 meV, and the broader ASP loss.

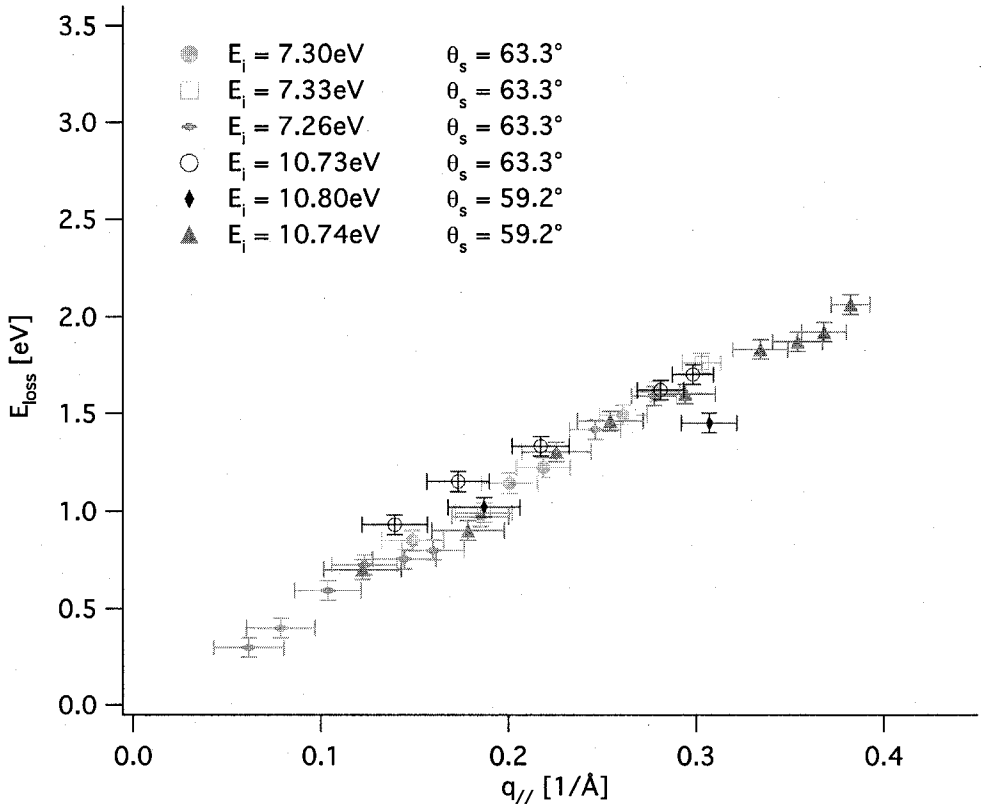

Figure 5-5: Experimental dispersion of the new excitation mode on Be(0001).

by binomial filtering over 21 points). With increasing O_2 exposure, this intensity decreases while its maximum shifts to slightly higher energy (right panel of Figure 5-6). After 12 Langmuir (L) O_2 the oxygen loss intensity has increased by a factor of 4, while the ASP loss intensity has decreased by approximatively 4.5 times. Since it is estimated by Auger electron spectroscopy that the contamination level of the nominally clean surface is of the order of 2% of a monolayer, the ASP loss has almost completely vanished at 8% oxygen contamination. It has also been checked whether the disappearance of the ASP loss at large oxygen exposure might be linked to the variation of the surface work function induced by oxygen adsorption. Therefore, EEL spectra were recorded at fixed (12 L) O_2 exposure for different work function compensations, but the intensity and energy of the ASP loss

could not be recovered. It can thus be concluded that a small oxygen contamination level does not affect the Be ASP dispersion and that the plasmon excitation is nearly suppressed at exposures of the order of 12 L of O_2. These results give an a posteriori confirmation that most of the inelastic signal is due to the ASP excitation rather than to electron–hole pairs, since the latter are expected to be less sensitive to oxygen contamination, and they contribute to the low energy loss side of the loss peak. Removing the contribution of the ASP loss to the inelastic intensity should therefore cause a shift of its maximum towards lower frequencies, contrary to experimental evidence.

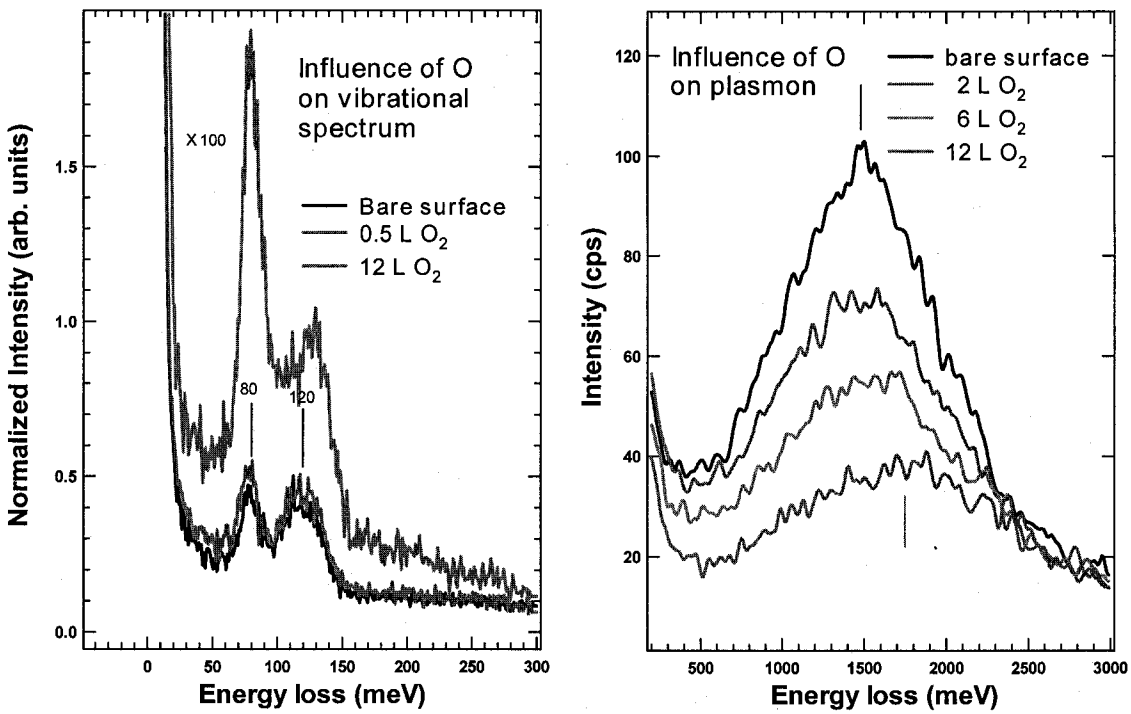

Figure 5-6: Oxygen exposure influence on acoustic surface plasmon.

5.3 Theoretical interpretation

Metal surfaces such as Be(0001) and the (111) surfaces of noble metals support a partially occupied band of Shockley surface states with energies near the Fermi level. Their wave functions are strongly localized near the surface and decay exponentially into the solid thus forming a quasi 2D electron gas overlapping the 3D bulk electrons. While employing a local dielectric function to describe the 3D continuum[67] has suggested that a complete screening of a 2D charge density *overlapping* a 3D plasma will prevent *any* low energy collective excitations to exist, we show that these experimental data can be interpreted as a novel type of collective electronic excitation (acoustic surface plasmon) of the quasi 2D surface charge distribution if a full non–local dynamical screening at the surface due to underlying 3D bulk electrons is considered. This collective mode corresponds to out–of–phase charge density oscillations of the 2D and 3D electron subsystems at a metal surface.

Information on collective electronic excitations at surfaces is obtained from the peak position of the imaginary part of the surface response function $g(\mathbf{q}_{\|},\omega)$ which depends on the two-dimensional momentum transfer parallel to the surface $\mathbf{q}_{\|}$ and the frequency ω [111, 57] (we use atomic units, i.e. $e^2 = \hbar = m_e = 1$):

$$g(\mathbf{q}_{\|},\omega) = \int d\mathbf{r} \int d\mathbf{r}' e^{q_{\|}z} \chi(\mathbf{r},\mathbf{r}',\omega) V_{ext}(\mathbf{r}',\omega), \tag{5.3}$$

where the external potential is of the form $V_{ext}(\mathbf{r}',\omega) = -\frac{2\pi}{q_{\|}} e^{q_{\|}z'} e^{i\mathbf{q}_{\|}\cdot\mathbf{r}_{\|}} e^{-i\omega t}$ and the non-local frequency-dependent density-response function of the interacting electron system $\chi(\mathbf{r},\mathbf{r}',\omega)$ is calculated in the framework of time-dependent density-functional theory using the integral equation (in symbolic form) $\chi = \chi^0 + \chi^0(\upsilon + f_{xc})\chi$, where υ is the bare Coulomb potential, χ^0 represents the density-response function of non-interacting electrons, and f_{xc} is the so-called exchange-correlation kernel chosen here to be zero (random-phase approximation).

The calculations were performed by Slava Silkin and Eugene Chulkov of Donastia International Physics Center, San Sebastian, Spain, for a slab of 24 Be atomic layers in a repeated-slabs geometry. The response function of non-interacting electrons χ^0 has a form

$$\chi^0_{\mathbf{G},\mathbf{G}'}(\mathbf{q}_\parallel,\omega) = \frac{2}{\mathrm{S}} \sum_{\mathbf{k}_\parallel}^{\mathrm{2DBZ}} \sum_{n,n'} \frac{f_{\mathbf{k}_\parallel,n} - f_{\mathbf{k}_\parallel+\mathbf{q}_\parallel,n'}}{E_{\mathbf{k}_\parallel,n} - E_{\mathbf{k}_\parallel+\mathbf{q}_\parallel,n'} + (\omega + i\eta)} \times$$

$$< \phi_{\mathbf{k}_\parallel,n} | e^{-i(\mathbf{q}_\parallel \cdot \mathbf{r}_\parallel + \mathbf{G}\cdot\mathbf{r})} | \phi_{\mathbf{k}_\parallel+\mathbf{q}_\parallel,n'} >< \phi_{\mathbf{k}_\parallel+\mathbf{q}_\parallel,n'} | e^{i(\mathbf{q}_\parallel \cdot \mathbf{r}_\parallel + \mathbf{G}'\cdot\mathbf{r})} | \phi_{\mathbf{k}_\parallel,n} > . \quad (5.4)$$

Here $f_{\mathbf{k}_\parallel,n}$ is the Fermi distribution function. The self-consistent one-electron energies $E_{\mathbf{k}_\parallel,n}$ and wave functions $\phi_{\mathbf{k}_\parallel,n}$ (expanded in plane waves with a cutoff of 20 Ry) were evaluated in the local density approximation with the use of *ab initio* norm-conserving pseudopotential and the exchange-correlation potential of Ref. [112]. The sums over all occupied and unoccupied energy bands n, n' were expanded up to 50 eV above the Fermi level. The 2D Brillouin zone (2DBZ) sampling was performed on the 108 × 108 mesh. The computed electronic surface structure of Be(0001) surface is shown in Figure 5-7.

The black dashed line shown in Fig. 5-8 is the acoustic dispersion curve that has been predicted assuming a free-electron like behavior for the surface state on Be(0001) located in a wide 3D-energy gap around $\overline{\Gamma}$ [113]. The calculation agrees qualitatively with the experiment in the sense that both have an acoustic character, but the quantitative agreement is rather poor. The reason for this turns out to be the insufficient accuracy in describing the surface electron state dispersion. We are able to reproduce the experimental dispersion quantitatively by employing an *ab initio* description of the surface electronic structure and the surface response function. The proper surface state dispersion around $\overline{\Gamma}$ (Fig. 5-7) deviates from the free-electron scenario. In the occupied part it is nearly parabolic with a binding energy of 2.7 eV at $\overline{\Gamma}$, in close agreement with photoemission measurements and previous calculations [114, 70, 115]. Nevertheless, important differences between the

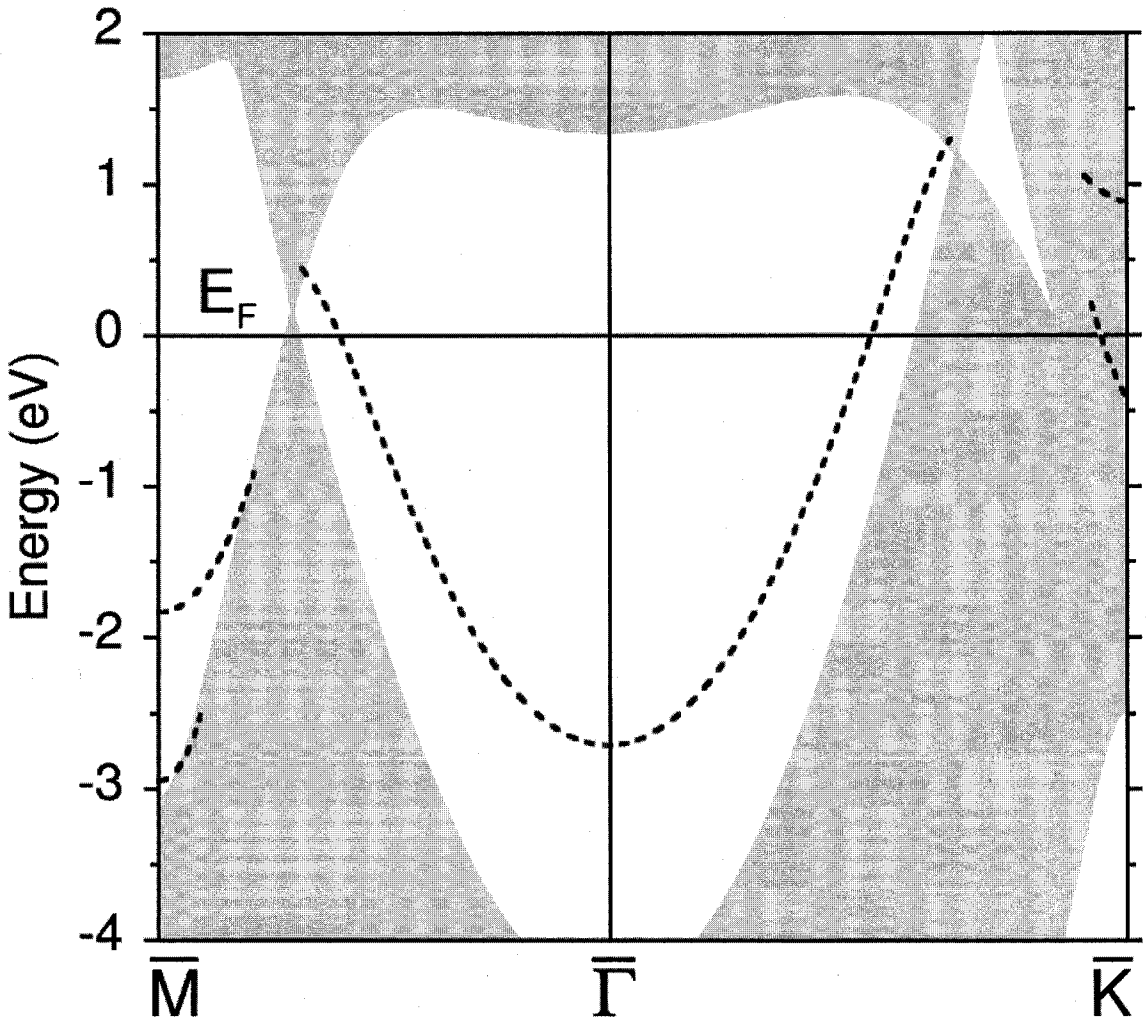

Figure 5-7: Be(0001) surface electronic structure. The surface states are shown by dashed lines. The colored areas show the projected bulk electronic bands.

actual surface–state band and a band of free electrons are (i) the considerable deviation from parabolic behavior above the Fermi level and (ii) the abrupt cut at the borders of the energy gap around 1 eV above the Fermi level. Using the *ab initio* surface state dispersion as a starting point for a calculation of the acoustic surface plasmon dispersion results in the red line in Fig. 5-8. Clearly, the agreement with the experimental data is much better, greatly increasing our confidence in the interpretation. The small difference between experimental and *ab initio* dispersions is attributed to the local density approximation used in the surface electronic structure evaluation.

The acoustic surface plasmon results from the interplay of the partially occupied electronic surface state, acting as a 2D electron density overlapping in the same region of space with the bulk electron gas, and the long–range Coulomb interaction manifested in the form of 3D dynamical screening of the 2D surface electron density. It corresponds to the out–of–phase charge oscillations between 2D and 3D subsystems and its dispersion is mainly determined by the surface-state Fermi velocity v_F^{2D} and follows closely the upper edge of the continuum for electron-hole pair excitations within the surface-state band (Fig. 5-8). The situation on Be(0001), which has a high v_F^{2D}, is favorable for an experimental observation because in this case the new collective excitation is well defined up to relatively high energies of more than 1 eV. On other surfaces with a partially occupied surface-state band, such as the noble-metal (111) surfaces, the new mode is expected to be best defined at lower energies up to about several hundreds meV[116] thus making its EELS detection more difficult[117] – one needs to be careful when choosing the scattering geometry and incident energy such that the scanned energy loss will cross the acoustic dispersion curve at low enough loss energies where electron-hole transitions from occupied 3D bulk states to unoccupied 2D surface states cannot occur. For its importance in electron and hole dynam-

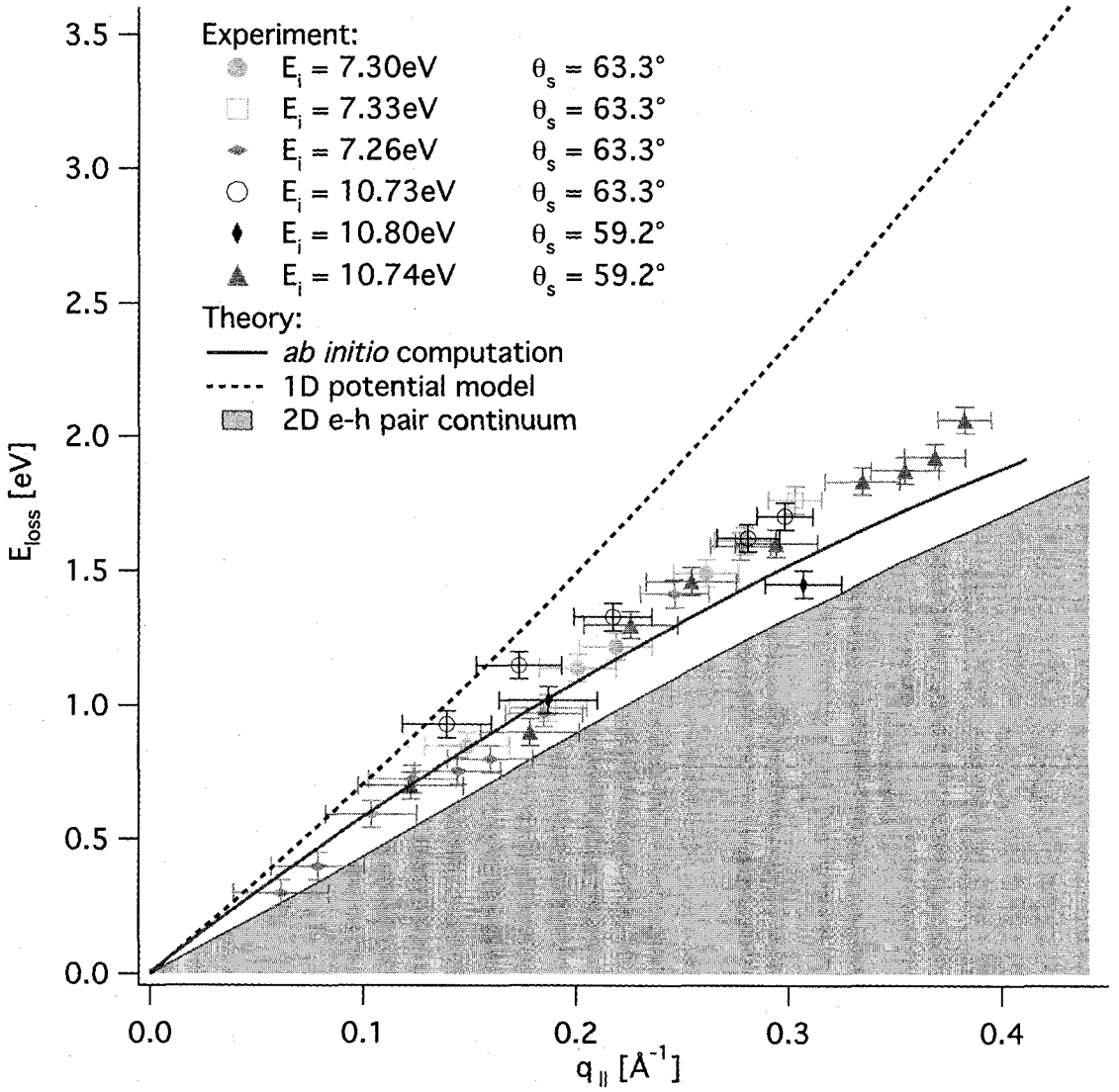

Figure 5-8: Acoustic surface plasmon energy dispersion. (a) Experimental dispersion measured at room temperature and various incident electron energies and scattering angles; energy error bars are due to uncertainties in the multi peak deconvolution procedure of the EEL spectra while $q_{||}$ error bars represent the momentum integration window due to the finite angular acceptance of the EEL spectrometer (as described in supplementary information). Theoretical dispersion: the black dashed line shows the predicted acoustic surface plasmon dispersion obtained for a free-electron like surface state, the solid red line was calculated by using an *ab initio* Be(0001) surface band structure.

ics, however, this restriction is of little relevance since the low-energy region is of highest importance.

Due to the isotropic surface state dispersion around $\bar{\Gamma}$ (Fig. 5-7), the orientation of the electron scattering plane is not expected to have any influence on the dispersion of the new excitation, as confirmed by *ab initio* calculations for the $\bar{\Gamma}$-$\bar{K}$ direction.

5.4 Conclusions

Acoustic surface plasmons, as reported here, owe their existence to the non-local screening due to bulk electrons at surfaces characterized by a partially occupied surface-state band lying in a wide bulk energy gap (Fig. 5-7) and as such they should be a common phenomenon on many metal surfaces. Moreover, since the acoustic plasmon dispersion follows closely the upper edge of electron-hole excitation, it will affect the electron dynamics near the Fermi level much more dramatically than regular 2D plasmons[65], which due to their $q_{\|}^{1/2}$ dispersion overlap in a much narrower range in energy-momentum space with the electron-hole continuum. The possibility to excite a collective mode at very low energies can therefore lead to new situations at metal surfaces due to the competition between the incoherent electron-hole excitations and the new collective coherent mode. Many phenomena, such as electron, phonon and adsorbate dynamics as well as chemical reactions with characteristic energies lower than few eV can be significantly influenced by the opening of a new low-energy decay channel such as the acoustic surface plasmon.

Of particular interest is the interaction of the acoustic surface plasmon with light. Since the slope of the acoustic surface plasmon dispersion, determined by v_F^{2D}, is about three orders of magnitude lower than the speed of light, the direct excitation of the new collective mode by light is not possible. However, the presence of nanometer-size objects at surfaces,

such as atomic steps or molecular structures can serve as a source of coupling between acoustic surface plasmons and light. The acoustic dispersion allows, at the same photon energy, for a collective surface excitation with a much lower associated wavelength than a regular 2D plasmon with its $q_{\parallel}^{1/2}$ dispersion. In this way, the new mode can serve as a tool to confine light in a broad frequency range up to optical frequencies on surface areas of a few nanometers thus ensuring the control of events at metal surfaces with both high spatial (nm) and temporal (fs) resolution. Another consequence of the acoustic character of the dispersion is that both phase and group velocity of the collective excitation are the same so that signals can be transmitted undistorted along the surface, an appealing fact for the field of sub-wavelength optics.

CHAPTER 6

CONCLUSIONS

In this thesis I described recent studies of new physical phenomena in systems with reduced dimensions, of the order of a few nanometers, and the instrumentation which I developed to access this nano length scale. Studies of systems with a size of a few nanometers requires investigation methods able to measure structural and electronic properties at atomic length scales.

A new design, development and performance of an ultra high vacuum and variable temperature scanning tunneling microscope (UHV–VT–STM), which I built at University of New Hampshire, is presented. The instrument provides large scale atomically resolved imaging of metallic surfaces and surface hosted phenomena. The in–vacuum vibration isolation and cryogenic system, which uses a high volume bath cryostat, has an excellent performance, the STM having a vertical resolution better that 2 pm in the whole temperature range of 90 K to 700 K. The scanning area is about 8 μm $\times$ 8 μm and the STM has the ability of finding the same nanometer size area on the sample even after sample preparation. The temperature drift is about 3 K/hour at 100 K. Also, the compact design of the STM–head, corroborated with the ability of preparing the STM tip in the ultra high vacuum environment, allows for fast–scanning, with atomic resolution at room temperature and below, of compact metallic surfaces. For a scanning frame with a size of about 100 Å $\times$ 100 Å and 256 $\times$ 256 pixels, fast scanning times of about 3 s have been achieved on

strained metallic interfaces. The system has also the ability of routinely prepare refractory metal samples, which require high temperature preparation. The sample can be heated via electron bombardment at temperatures in excess of 2200 K. Part of this instrumentation development work was submitted for publication in Ref. [86].

I used the VT–STM instrument to study the self–assembly processes on strained metallic interfaces. Initially, I performed an experimental study of various mechanisms in which ordered cluster arrays grow on various strained metallic thin films, followed by a focused experimental investigation of the most complex case, when a restructuring of the strained thin film takes place after a different atomic specie is adsorbed onto it. For the last, the case study was done on S_2 adsorbed on the short herringbone (SHB) misfit dislocation network of Ag on Ru(0001). The SHB of Ag, with a rectangular symmetry of the unit cell, relaxes toward a triangular unit cell superstructure, with S filled Ag vacancy islands at the corners of the triangle, after small S_2 adsorbs onto the Ag film. The process involves a rearrangement of a large number of Ag atoms. I have found that this self–assembly process is driven by the stress relaxation in the Ag film after S creates Ag vacancy islands by binding on the Ru(0001) surface. The process involves a threading dislocation pair annihilation, which yields to the formation of one Ag vacancy island. At the normal S_2 deposition temperature of 295 K, the S filled Ag vacancy islands are very mobile, and they diffuse along the Ag film. This diffusion allows for the growth of large scale and ordered arrays of Ag vacancy islands, when individually formed Ag vacancy islands are diffusing along the Ru(0001) surface until they meet other vacancy islands and cluster together. The process is described via an atomistic 2D Frenkel–Kontorova model based on first–principles input parameters for the atomic interaction potentials. Such a self–assembly process should be a general one since the only physics requirements are that we start with a strained metallic film (Ag) grown

onto a dissimilar material surface (Ru(0001)), on which a third atomic or molecular specie (S_2) is adsorbed. The third specie must have a higher binding energy on the substrate (Ru(0001)) than on the strained metallic film (Ag). The general study of self–assembly on strained metallic interfaces is presented in Ref. [85] and the S adsorbtion on the SHB of Ag on Ru(0001) is going to be submitted for publication as Ref. [98].

The diversity of cluster arrays sizes and structures that can be grown on the strained metallic surfaces from various atomic or molecular constituents opens the door to novel fundamental electronic, optical, catalytic, magnetic, ferroelectric, chemical, biological, and mechanical properties.

In the last part I have shown how reduced dimensionality can give rise to novel electronic properties. A crystal surface system has physical properties different than the bulk crystal. The surface in this respect can be considered as a nano system, where the dimension normal to the surface is of just few atomic distances. The electron energy loss spectroscopy study of low–energy electronic excitations at the (0001) surface of Be shows the existence of a novel collective excitation of the surface electrons. The energy of the new excitation disperses with the electron momentum parallel to the surface in an acoustic fashion. This unexpected behavior is a consequence of the unoccupied electron surface state of Be(0001), residing in the bandgap of bulk states, which couples dynamically and non–locally with the occupied electron states in the bulk. Thus, it gives rise to a collective oscillation of the surface electrons, as shown by first–principles calculations.

This new phenomena is a general one, also applying to systems like Cu(111) or Ag(111), where a partially occupies electronic surface state band exists in a bandgap of bulk electronic states. The existence of a low-energy collective excitation on surfaces will have important consequences on electron–phonon dynamics and adsorbate chemistry at surfaces, and sub-

wavelength optics, with possible important applications in nano–optics. This last part is presented in Ref. [71].

Appendix A:

Drawings of the Variable Temperature STM

ALUMINUM 6061	UNH, Surface Science - Physics Dept.
	COOLING MASS, TOP VIEW (2)
	07/02/2001 | Scale 1:1
	Bogdan Diaconescu | page 3 of 7

ALUMINUM 6061	UNH, Surface Science - Physics Dept.
	COOLING MASS, TOP VIEW
	07/02/2001 | Scale 1:1
	Bogdan Diaconescu | page 2 of 7

ALUMINUM 6061	UNH, Surface Science - Physics Dept.
	COOLING MASS, 3D
	07/02/2001 | Scale 1:2.5
	Bogdan Diaconescu | page 1 of 7

OFHC copper	UNH, Surface Science - Physics Dept.
	LN2 piece v. 2, Top View
	11/01/02 | Scale 1:1
	Bogdan Diaconescu | page 1 of 6

use only water soluble cutting fluids

St-St 304 (316) for hooks	UNH, Surface Science - Physics Dept.
	Cooling Mass hooks and standoffs
Vespel SP1for Standoffs	12/02/2003 | Scale 2:1
	Bogdan Diaconescu | page 1 of 1

ALUMINUM 6061	UNH, Surface Science - Physics Dept.
	COOLING MASS, BOTTOM VIEW
	07/02/2001 | Scale 1:1
	Bogdan Diaconescu | page 7 of 7

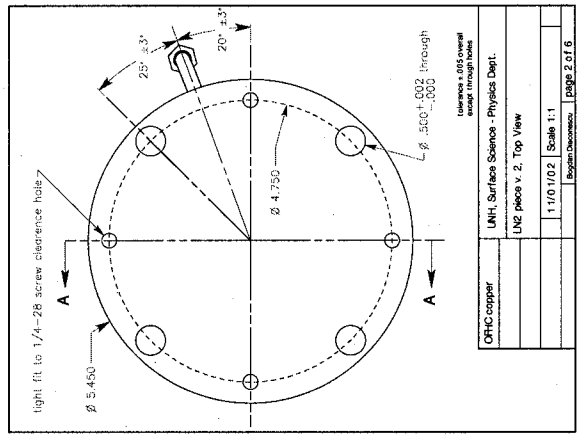

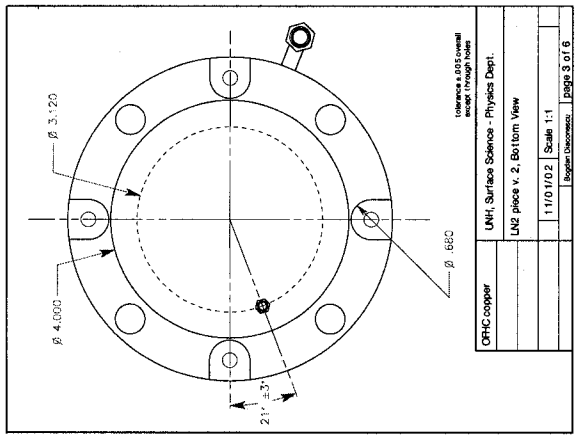

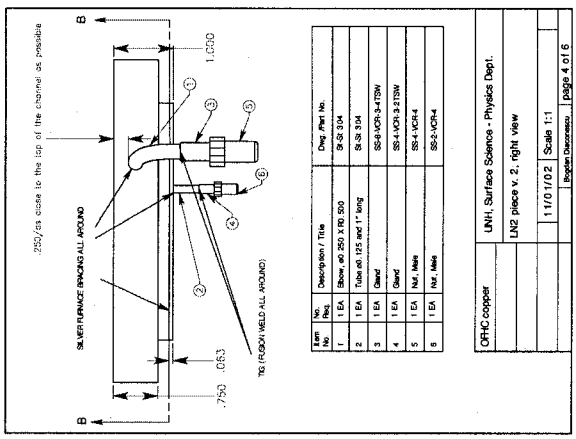

St-St 304	UNH, Surface Science - Physics Dept.
	MAGNET HOLDER, TOP VIEW 12 EACH
	06/24/01 Scale 2:1
	Bogdan Diaconescu page 2 of 4

St-St 304	UNH, Surface Science - Physics Dept.
	MAGNET HOLDER, 3D 12 EACH
	06/24/01 Scale 2:1
	Bogdan Diaconescu page 1 of 4

	UNH, Surface Science - Physics Dept.
	1/4" Custom Liquid Nitrogen Feedthrough
	07/30/01 Drawing NOT on scale
	Bogdan Diaconescu page 1 of 1

St-St 304	UNH, Surface Science - Physics Dept.
	MAGNET RING, 3D
	06/18/01 Scale 1:2
	Bogdan Diaconescu page 1 of 3

St-St 304	UNH, Surface Science - Physics Dept.
	MAGNET HOLDER, VIEW A-A 12 EACH
	06/24/01 Scale 2:1
	Bogdan Diaconescu page 4 of 4

St-St 304	UNH, Surface Science - Physics Dept.
	MAGNET HOLDER, RIGHT VIEW 12 EACH
	06/24/01 Scale 2:1
	Bogdan Diaconescu page 3 of 4

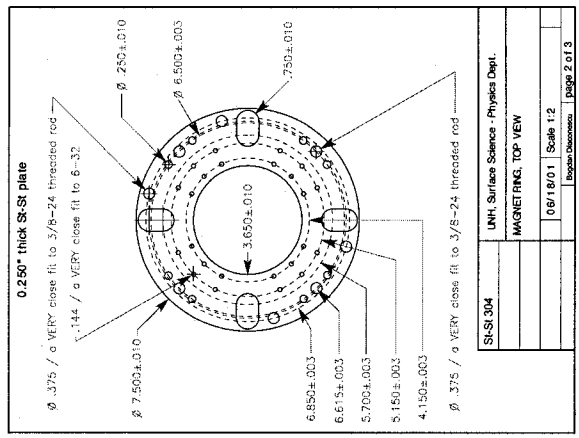

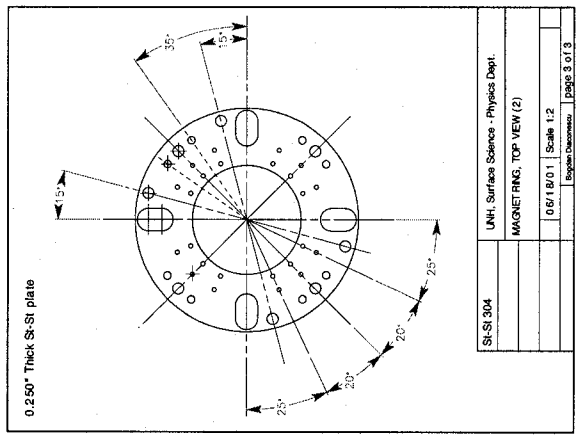

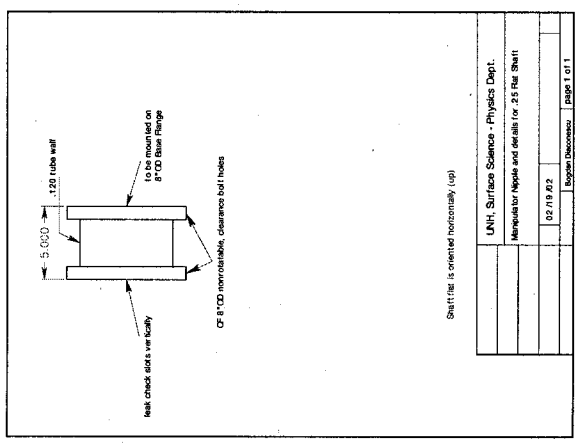

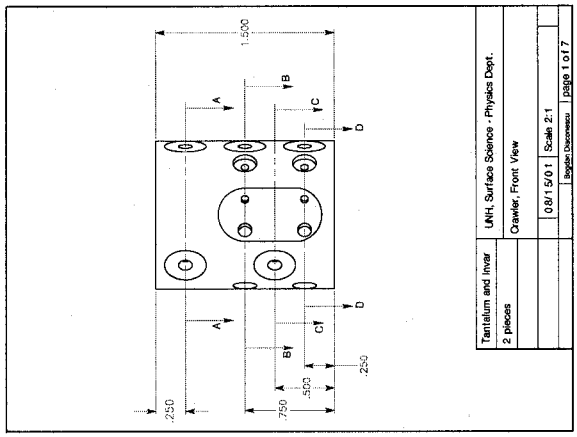

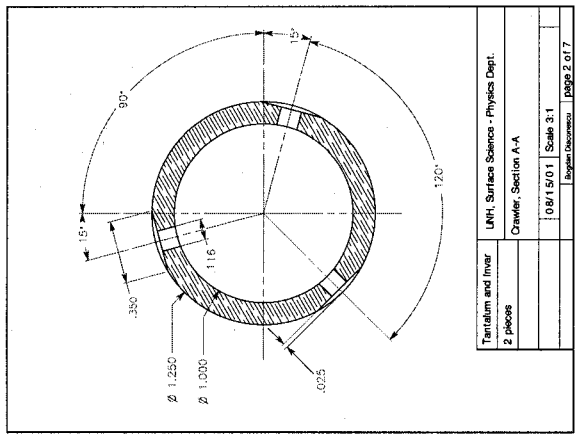

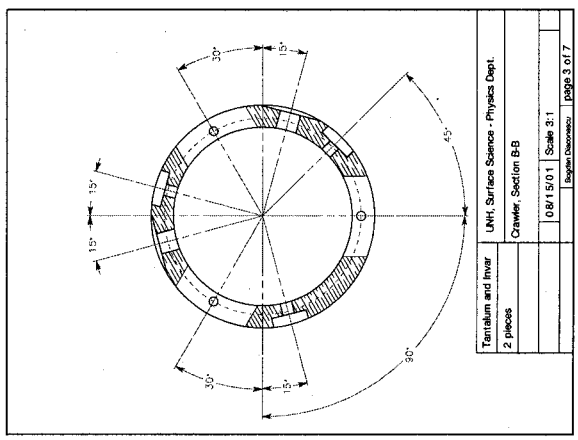

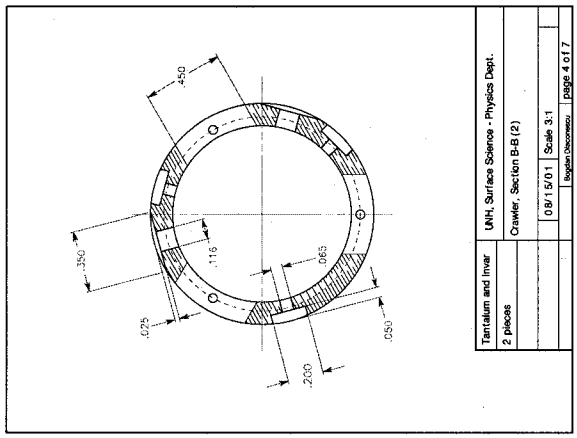

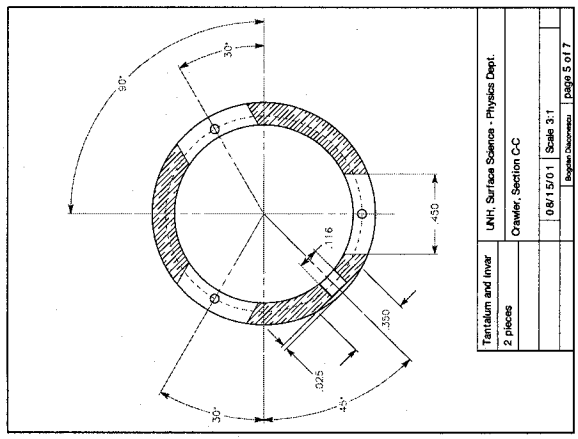

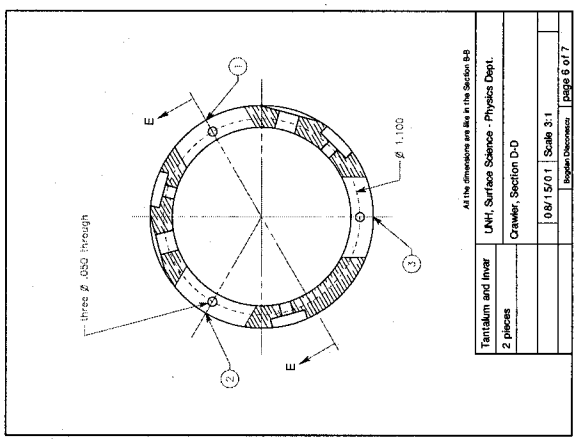

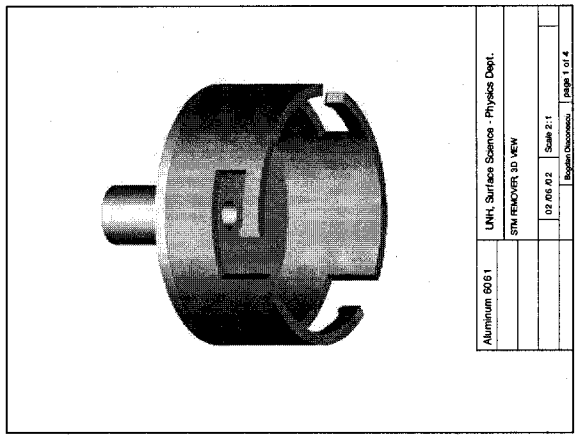

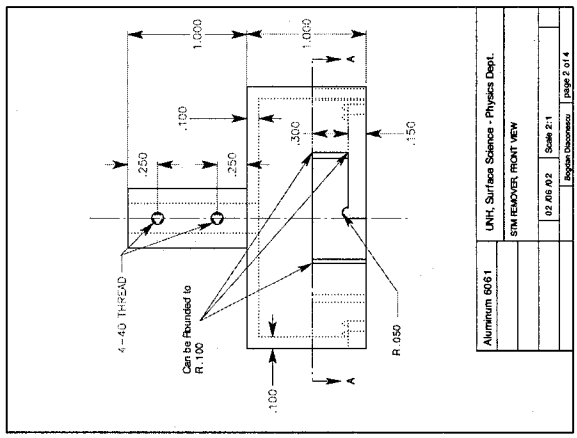

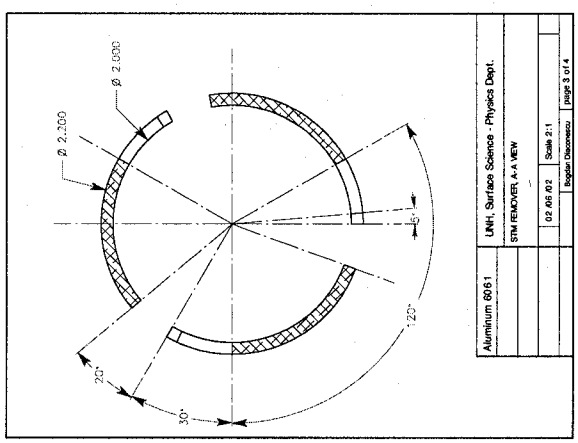

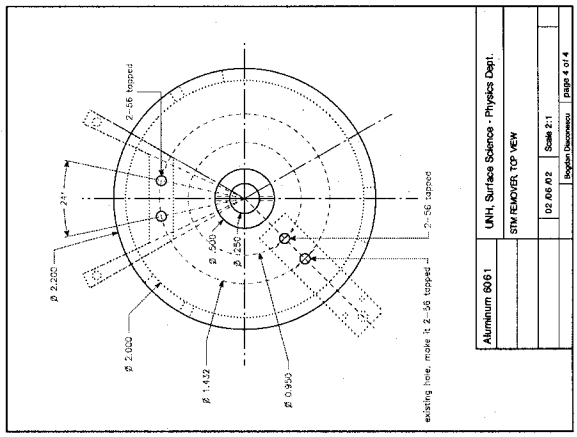

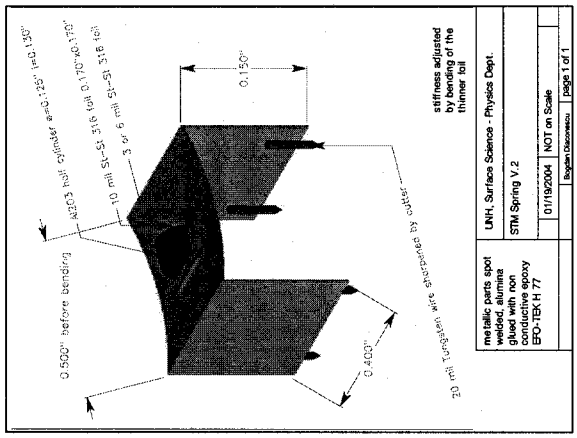

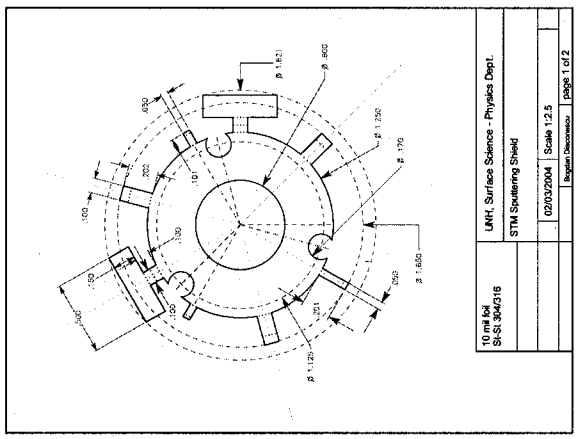

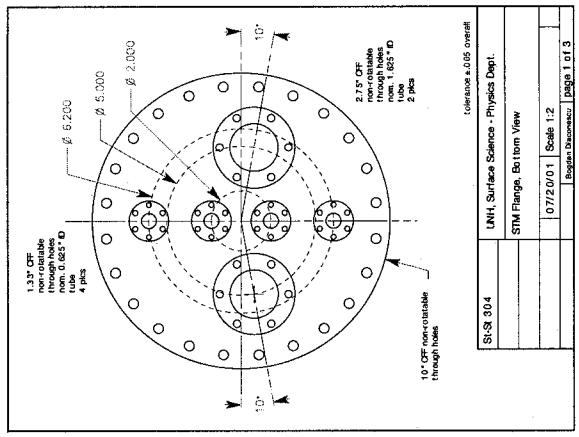

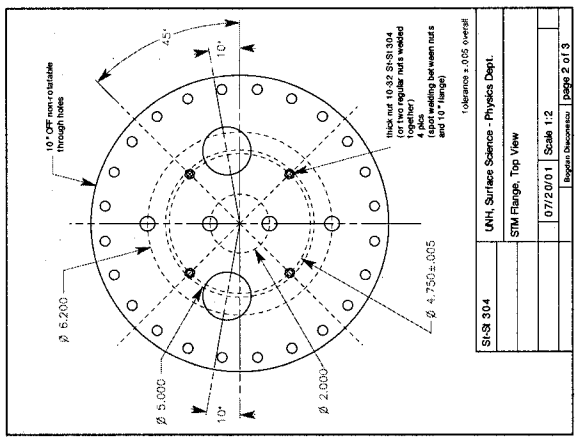

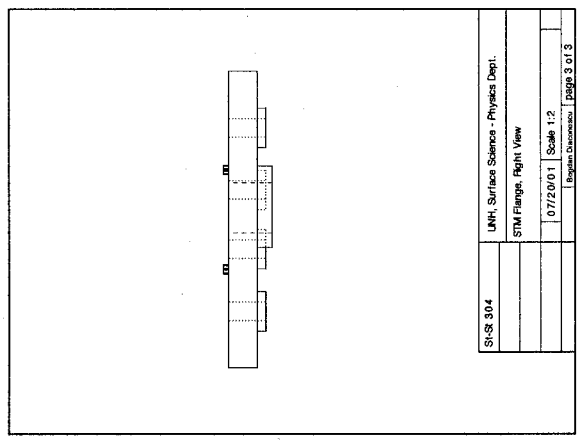

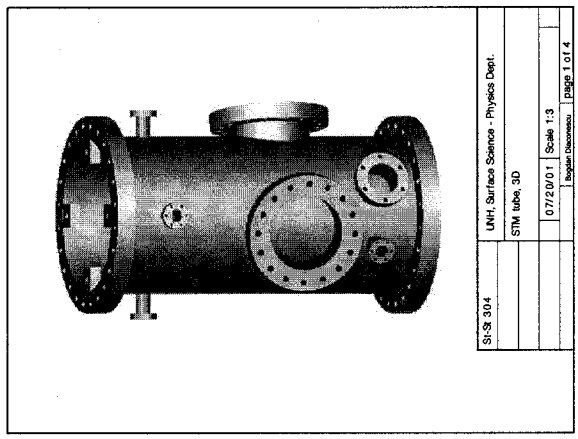

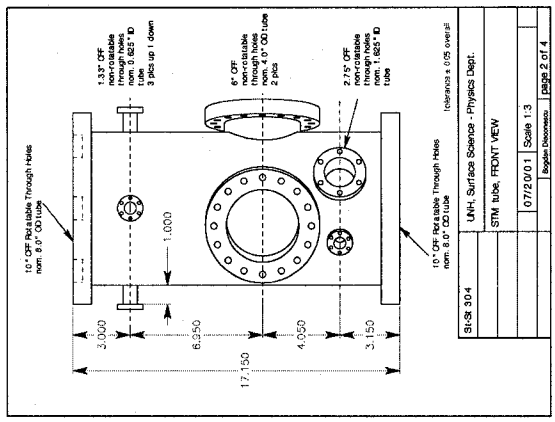

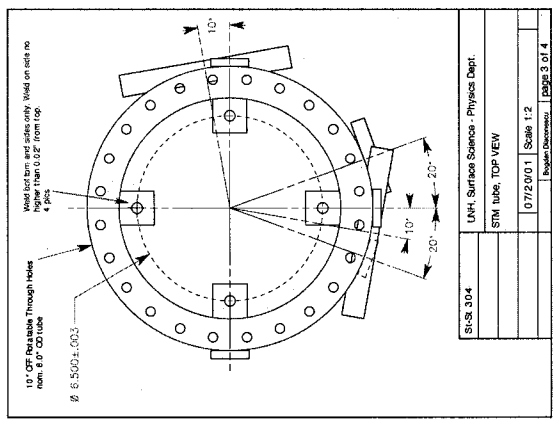

Appendix B:

S phase diagram on Ru(0001)

The following phase diagram was taken from R. Dennert *et al.* [104].

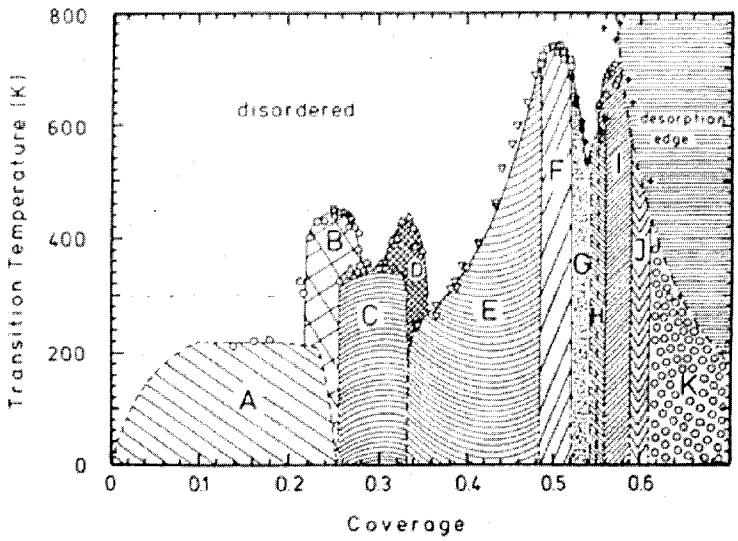

Fig. 9. Phase diagram of the system S/Ru(001) with the following ordered phases: A: p(2 × 2) islands + disordered lattice gas; B: homogeneous p(2 × 2) phase; C: coexistence of p(2 × 2) and $(\sqrt{3} \times \sqrt{3})$R30° ordered domains; D: homogeneous $(\sqrt{3} \times \sqrt{3})$R30° phase; E: striped superheavy domain walls; F: c(2 × 4)-2S structure; G: fluid phase; H: $\begin{pmatrix} 7 & 0 \\ 3 & 2 \end{pmatrix}$ phase; left part: homogeneous phase; right part: coexistence of $\begin{pmatrix} 7 & 0 \\ 3 & 2 \end{pmatrix}$ and $(\sqrt{7} \times \sqrt{7})$R19.1°-4S phases; I: $(\sqrt{7} \times \sqrt{7})$R19.1°-4S phase; J: split $(\sqrt{7} \times \sqrt{7})$R19.1° phase; K: disordered layer, second layer starts to form.

List of References

[1] Eigler, D. M. & Schweizer, E. K. Positioning single atoms with a scanning tunnelling microscope. *Nature* **344**, 524–526 (1990).

[2] Heinrich, A. J., Lutz, C. P., Gupta, J. A. & Eigler, D. M. Molecule Cascades. *Science* **298**, 1381–1387 (2002).

[3] Brust, M., Walker, M., Bethel, D., Schiffrin, D. J. & Whyman, R. Synthesis of thiol-derivatized gold nanoparticles in a two-phase liquid-liquid system. *J. Chem. Soc. Chem. Commun.* **7**, 801–802 (1994).

[4] Brust, M., Bethel, D., Schiffrin, D. J. & Kiely, C. J. Novel gold-dithiol nano-networks with non-metallic electronic properties. *Adv. Mater* **7**, 795–797 (1995).

[5] Moriarty, P. Nanostructured materials. *Rep. Prog. Phys.* 297–381 (2000).

[6] Rosei, F. Nanostructured surfaces: challenges and frontiers in nanotechnology. *J. Phys. Condens. Matter* S1373–S1436 (2004).

[7] Rosei, F., Schunack, M., Naitoh, Y., Jiang, P., Gourdon, A., Laegsgaard, E., Stensgaard, I., Joachim, C. & Besenbacher, F. Properties of large organic molecules on metal surfaces. *Prog. Surf. Sci.* 95–146 (2003).

[8] Smith, R., Lewis, P. & Weiss, P. Patterning self–assembled monolayers. *Prog. Surf. Sci.* 1–68 (2004).

[9] Feynman, P. There is plenty room at the bottom. *http://www.zyvex.com/nanotech/feynman.html – originally published in the February 1960 issue of Caltech's Engineering and Science* (1959).

[10] Binning, G., Rohrer, H., Gerber, C. & Weibel, E. Surface studies by scanning tunneling microscopy. *Phys. Rev. Lett.* **49**, 57–61 (1982).

[11] Binning, G., Rohrer, H., Gerber, C. & Weibel, E. Tunneling through a controllable vacuum gap. *Appl. Phys. Lett.* **40**, 178–180 (1982).

[12] Binning, G. & Rohrer, H. Scanning tunneling microscopy–from birth to adolescence. *Rev. Mod. Phys.* **59**, 615–625 (1987).

[13] Stroscio, J. A. & Kaiser, W. J. *Scanning Probe Microscopy* (Boston Academic Press, Boston, MA, 1993).

[14] Wiesendanger, R. *Scanning Probe Microscopy and Spectroscopy: Methods and Applications* (Cambridge University Press, Cambridge, MA, 1994).

[15] Binning, G., Quate, C. F. & Gerber, C. Atomic Force Microscope. *Phys. Rev. Lett.* 930–933 (1986).

[16] Besenbacher, F. Scanning tunnelling microscopy studies of metal surfaces. *Rep. Prog. Phys.* **59**, 1737–1802 (1996).

[17] Neddermeyer, H. Scanning tunnelling microscopy of semiconductor surfaces. *Rep. Prog. Phys.* **59**, 701–769 (1996).

[18] Eigler, D. M., Lutz, C. P. & Rudge, W. E. An atomic switch realized with the scanning tunnelling microscope. *Nature* **352**, 600–603 (1991).

[19] Manoharan, H. C., Lutz, C. P. & Eigler, D. M. Quantum mirages formed by coherent projection of electronic structure. *Nature* **403**, 512–515 (2000).

[20] Ho, W. Inducing and Viewing Bond Selected Chemistry with Tunneling Electrons. *Acc. Chem. Res.* **31**, 567–573 (1998).

[21] Hla, S. W. & Rieder, K. H. STM CONTROL OF CHEMICAL REACTIONS: Single-Molecule Synthesis. *Annu. Rev. Phys. Chem.* **54**, 307–330 (2003).

[22] Hla, S. W., Bartels, L., Mayer, G. & Rieder, K. H. Inducing All Steps of a Chemical Reaction with the Scanning Tunneling Microscope Tip: Towards Single Molecule Engineering. *Phys. Rev. Lett.* **85**, 2777–2780 (2000).

[23] Pimpinelli, A. & Villain, J. *Physics of Crystal Growth* (Cambridge University Press, Cambridge, 1998).

[24] Venables, J. A. *Introduction to surface and thin film processes* (Cambridge University Press, Cambridge, 2000).

[25] Whitesides, G. M. & Grzybowski, B. Self-assembly at all scales. *Science* **295**, 2418–2421 (2002).

[26] Barth, J. V., Constantini, G. & Kern, K. Engineering atomic and molecular nanostructures at surfaces. *Nature* **437**, 671–679 (2005).

[27] Chambliss, D. D., S., R. J. W. & Chiang. Nucleation of ordered Ni island arrays on Au(111) by surface-lattice dislocations. *Phys. Rev. Lett.* **66**, 1721–1724 (1991).

[28] Barth, J. V., Brune, H., Ertl, G. & Behm, R. J. Scanning tunneling microscopy observations on the reconstructed Au(111) surface: Atomic structure, long-range su-

perstructure, rotational domains, and surface defects. *Phys. Rev. B* **42**, 9307–9318 (1990).

[29] Günther, C., Vrijmoeth, J., Hwang, R. Q. & Behm, R. J. Strain relaxation in hexagonally close-packed metal-metal interfaces. *Phys. Rev. Lett.* **74**, 754–757 (1995).

[30] Brune, H., Giovannini, M., Bromann, K. & Kern, K. Self-organized growth of nanostructure arrays on strain-relief patterns. *Nature* **394**, 451–453 (1998).

[31] van Gastel, R., Plass, R., Bartelt, N. C. & Kellogg, G. L. Thermal motion and energetics of self-assembled domain structures: Pb on Cu(111). *Phys. Rev. Lett.* **91**, 055503 (2003).

[32] Christensen, A., Ruban, A. V., Stoltze, P., Jacobsen, K. W., Skriver, H. L., Nørskov, J. K. & Besenbacher, F. Phase diagrams for surface alloys. *Phys. Rev. B* **56**, 5822–5834 (1997).

[33] S. Helveg, S., Lauritsen, J. V., Lægsgaard, E., Stensgaard, I., Nørskov, J. K., Clausen, B. S., Topsøe, H. & Besenbacher, F. Atomic-scale structure of single-layer MoS_2 nanoclusters. *Phys. Rev. Lett.* **84**, 951–954 (2000).

[34] Ling, W. L., de la Figuera, J., Bartelt, N. C., Hwang, R. Q., Schmid, A. K., Thayer, G. E. & Hamilton, J. C. Strain relief through heterphase interface reconstruction: Ag(111)/Ru(0001). *Phys. Rev. Lett.* **92**, 116102–1–116102–4 (2004).

[35] Pohl, K., Bartelt, M. C., de la Figuera, J., Bartelt, N. C., Hrbek, J. & Hwang, R. Identifying the forces responsible for self-organization of nanostructures at crystal surfaces. *Nature* **397**, 238–241 (1999).

[36] Thürmer, K., Carter, C. B., Bartelt, N. C. & Hwang, R. Q. Self-assembly via adsorbate-driven dislocation reactions. *Phys. Rev. Lett.* **92**, 106101–106104 (2004).

[37] Thürmer, K., Carter, C. B., Bartelt, N. C. & Hwang, R. Q. Surface self-organization caused by dislocation networks. *Science* **311**, 1272–1274 (2006).

[38] Mo, Y. W., Savage, D. E., Swartzentruber, B. S. & Lagally, M. G. Kinetic Pathway in Stranski-Krastanov Growth of Ge on Si(001). *Phys. Rev. Lett.* **65**, 1020–1023 (1990).

[39] Medeiros-Ribeiro, G., Bratkowski, A. M., Kamins, T. I., Ohlberg, D. A. A. & Williams, R. S. Shape Transition of Germanium Nanocrystals on a Silicon (001) Surface from Pyramids to Domes. *Science* **279**, 353–355 (1998).

[40] Ross, F. M., Tromp, R. M. & Reuter, M. C. Transition States Between Pyramids and Domes During Ge/Si Island Growth. *Science* **286**, 1931–1934 (1999).

[41] Theobald, J., Oxtoby, N., Phillips, M. A., Chamness, N. R. & Beton, P. H. Controlling molecular deposition and layer structure with supramolecular surface assemblies. *Nature* **424**, 1029–1031 (2003).

[42] Corso, M., Auwarter, W., Muntwiler, M., Tamai, A., Greber, T. & Osterwalder, J. Boron Nitide nanomesh. *Science* **303**, 217–220 (2004).

[43] Vanderbilt, D. Phase segregation and work-function variations on metal surfaces: spontaneous formation of periodic domain structures. *Surf. Sci.* **268**, L300–L304 (1992).

[44] Alerhand, O. L., Vanderbilt, D., Meade, R. D. & Joannopoulos, J. D. Spontaneous formation of stress domains on crystal surfaces. *Phys. Rev. Lett.* **61**, 1973–1976 (1988).

[45] Marchenko, V. I. Possible structures and phase transitions on the surface of crystals. *Sov. Phys. JETP Lett.* **33**, 381–383 (1981).

[46] Narasimhan, S. & Vanderbilt, D. Elastic stress domains and the herringbone reconstruction on Au(111). *Phys. Rev. Lett.* **69**, 1564–1567 (1992).

[47] Takeuchi, N., Chan, C. T. & Ho, K. M. Au(111): A theoretical study of the surface reconstruction and the surface electronic structure. *Phys. Rev. B* **43**, 13899–13906 (1991).

[48] Bott, M., Hohage, M., Michely, T. & Comsa, G. Pt(111) reconstruction induced by enhanced pt gas-phase chemical potential. *Phys. Rev. Lett.* **70**, 1489–1492 (1993).

[49] Hwang, R. Q., Hamilton, J. C., Stevens, J. L. & Foiles, S. M. Near-surface buckling in strained metal overlayer systems. *Phys. Rev. Lett.* **75**, 4242–4245 (1995).

[50] Tersoff, J. & Hamann, D. R. Theory and application for the scanning tunneling microscope. *Phys. Rev. Lett.* **50**, 1993 (1983).

[51] Pines, D. & Bohm, D. A collective description of electron interactions: II. Collective vs. individual particle aspects of the interactions. *Phys. Rev.* **85**, 338–352 (1952).

[52] Pines, D. Collective Energy Losses in Solids. *Rev. Mod. Phys.* **28**, 184–198 (1956).

[53] Ritchie, R. H. Plasma Losses by Fast Electrons in Thin Films. *Phys. Rev.* **106**, 874–881 (1957).

[54] Stern, E. A. & Farrell, R. A. Surface Plasma Oscillations of a Degenerate Electron Gas. *Phys. Rev.* **120**, 130–136 (1960).

[55] Feibelman, P. J. Inclusion of dynamics in the ion-metal surface interaction. *Surf. Sci.* **27**, 438–450 (1971).

[56] Tsuei, K.-D., Plummer, E. W. & Feibelman, P. J. Surface-Plasmon Dispersion in Simple Metals. *Phys. Rev. Lett.* **63**, 2256–2259 (1989).

[57] Liebsch, A. *Electronic Excitations at Metal Surfaces* (Plenum Press, London, 1997).

[58] Rocca, M. Low-energy EELS investigation of surface electronic excitations on metals. *Surf. Sci. Rep.* **22**, 1–71 (1995).

[59] Schuster, S. C., Swanson, R. V., Alex, L. A., Bourret, R. B. & Simon, M. I. Assembly and function of a quaternary signal transduction complex monitored by surface plasmon resonance. *Nature* **365**, 343–347 (1993).

[60] Pendry, J. Playing Tricks with Light. *Science* **285**, 1687–1688 (1999).

[61] Barnes, W. L., Dereux, A. & Ebbesen, T. W. Surface plasmon subwavelength optics. *Nature* **424**, 824–830 (2003).

[62] Lezec, H., Degiron, A., Devaux, E., Linke, R. A., Martin-Moreno, L., Garcia-Vidal, F. J. & Ebbesen, T. W. Beaming Light from a Subwavelength Aperture. *Science* **297**, 820–822 (2002).

[63] Stern, F. Polarizability of a Two-Dimensional Electron Gas. *Phys. Rev. Lett.* **18**, 546–548 (1967).

[64] S. J. Allen and, D. C. T. & Logan, R. A. Observation of the Two-Dimensional Plasmon in Silicon Inversion Layers. *Phys. Rev. Lett.* **38**, 980–983 (1977).

[65] Nagao, T., Hildebrandt, T., Henzler, M. & Hasegawa, S. Dispersion and Damping of a Two-Dimensional Plasmon in a Metallic Surface-State Band. *Phys. Rev. Lett.* **86**, 5747–5750 (2001).

[66] Chaplik, A. V. Possible Crystallization of Charge Carriers in Low-Density Inversion Layers. *Sov. Phys. JETP* **35**, 395–398 (1972).

[67] Sarma, S. D. & Madhukar, A. Collective modes of spatially separated, two-component, two-dimensional plasma in solids. *Phys. Rev. B* **23**, 805–815 (1981).

[68] Eguiluz, A., Lee, T. K., J, Q., J & Chiu, K. W. Interface excitations in metal–insulator–semiconductor structures. *Phys. Rev. B* **11**, 4989–4993 (1975).

[69] Inglesfield, J. E. Surface electronic structure. *Rep. Prog. Phys.* **45**, 223–284 (1982).

[70] Bartynski, R. A., Jensen, E., Gustafsson, T. & Plummer, E. W. Angle-resolved photoemission investigation of the electronic structure of Be: Surface states. *Phys. Rev. B* **32**, 1921–1926 (1985).

[71] Diaconescu, B., Pohl, K., Vattuone, L., Savio, L., Hofmann, P., Silkin, V. M., Pitarke, J. M., Chulkov, E. V., Echenique, P. M., Farías, D. & Rocca, M. Low-energy acoustic plasmons at metal surfaces in–press.

[72] March, N. H. & Tosi, M. P. Collective effects in condensed conducting phase including low-dimensional systems. *Adv. Phys.* **44**, 299–386 (1995).

[73] Ruvalds, J. Are plasmons the key to superconducting oxides? *Nature* **328**, 299 (1987).

[74] Bott, M., Micheley, T. & Comsa, G. Design principles of a variable temperature scanning tunneling microscope. *Rev. Sci. Instrum.* **66**, 4235–4139 (1995).

[75] Dubson, M. A. & Hwang, J. S. Simple, variable-temperature, scanning tunneling microscope. *Rev. Sci. Instrum.* **63**, 3643–3645 (1992).

[76] Insaco Incorporated. URL `http:// www.insaco.com`.

[77] DuPont. URL `http://www.dupont.com`.

[78] Staveley NDT Technologies. URL `http://www.staveleyndt.com`.

[79] Epoxy Technology. Epoteck H–27 D. URL `http:// www.epotek.com`.

[80] Epoxy Technology. Epoteck H–77. URL `http:// www.epotek.com`.

[81] A. K. Schmid. Private communication.

[82] Thayer, G. E. *The role of stress in thin alloy films: a scanning tunneling microscopy investigation of CoAg/Ru(0001).* Ph.D. thesis, University of California at Davis (2001).

[83] Pan, S. H., Hudson, E. W. & Davis, J. C. ^{3}He refrigerator based very low temperature scanning tunneling microscope. *Rev. Sci. Instrum.* **66**, 4235–4139 (1995).

[84] Ibe, J. P., Jr., P. P. B., Brandow, S. L., Brizzolara, R. A., Burnham, N. A., DiLella, D. P., Lee, K. P., Marrian, C. R. K. & Colton, R. J. On the electrochemical etching of tips for scanning tunneling microscopy. *J. Vac. Sci. Technol.* **8**, 3570–3575 (1990).

[85] Diaconescu, B., Nenchev, G., Jones, J. & Pohl, K. Self-organized nanotemplating on misfit dislocation networks investigated by scanning tunneling microscopy. *Microscopy Res. Technique* (in press).

[86] Diaconescu, B., Nenchev, G., de la Figuera, J. & Pohl, K. An ultra high vacuum fast–scanning and variable temperature scanning tunneling microscope for large scale imaging. *Review of Scientific Instruments* (submitted).

[87] Ling, W. L., Hamilton, J. C., Thürmer, K., Thayer, G., de la Figuera, J., Hwang, R., Carter, C., Bartelt, N. & McCarty, K. Herringbone and triangular patterns of dislocations in Ag, Au, and AgAu alloy films on Ru(0001). *Surf. Sci.* **600**, 1735–1757 (2006).

[88] Hamilton, J. C. & Foiles, S. M. Misfit dislocation structure for clode-packed metal-metal interfaces. *Phys. Rev. Lett.* **75**, 882–885 (1995).

[89] Hamilton, J. C. Dislocation nucleation rates during submonolayer growth of heteroepitaxial thin films. *Phys. Rev. B* **55**, R7402–R7405 (1997).

[90] Hamilton, J. C., Stumpf, R., Bromann, K., Giovannini, M., Kern, K. & Brune, H. Dislocation structures of submonolayer films near the commensurate-incommensurate phase transition: Ag on Pt(111). *Phys. Rev. Lett.* **82**, 4488–4491 (1999).

[91] Thayer, G. E., Bartelt, N. C., Ozolins, V., Schmid, A. K., Chiang, S. & Hwang, R. Q. Linking surface stress to surface structure: Measurement of atomic strain in a surface alloy using scanning tunneling microscopy. *Phys. Rev. Lett.* **89**, 036101–1–036101–4 (2002).

[92] Voigtländer, B., Meyer, G. & Amer, N. M. Epitaxial growth of thin magnetic cobalt films on Au(111) studied by scanning tunneling microscopy. *Phys. Rev. B* **44**, 10354–10357 (1991).

[93] Fruchart, O., Klaua, M., Barthel, J. & Kirschner, J. Self-organized growth of nano-sized vertical magnetic Co pillars onAu(111). *Phys. Rev. Lett.* **83**, 2769–2772 (1999).

[94] Stroscio, J. A., Pierce, D. T., Dragoset, R. A. & First, P. N. Microscopic aspects of the initial growth of metastable fcc iron on Au(111). *J. Vac. Sci. Technol. A* **10**, 1981–1985 (1992).

[95] Chambliss, D. D., Wilson, R. J. & Chiang, S. Nucleation of ordered Ni island array on Au(111) by the surface-lattice dislocations. *Phys. Rev. Lett.* **66**, 1721–1724 (1991).

[96] Chambliss, D. D., Wilson, R. J. & Chiang, S. Ordered nucleation of Ni and Au islands on Au(111) studied by scanning tunneling microscopy. *J. Vac. Sci. Technol. B* **9**, 933–937 (1991).

[97] Xu, G. Q. & Hrbek, J. New adsorption states of hydrogen on sulfur modified Ru(001). *Catal. Lett.* **2**, 35–41 (1989).

[98] Diaconescu, B. & Pohl, K. Self assembly of 2D nanocluster array via dislocation pair annihilation and glide (to be published).

[99] Hrbek, J., de la Figuera, J., Pohl, K., Jirsak, T., Rodriguez, J. A., Schmid, A. K., Bartelt, N. C. & Hwang, R. Q. A prelude to surface chemical reaction: Imaging the induction period of sulfur interaction with a strained Cu layer. *J. Phys. Chem. B* **103**, 10557–10561 (1999).

[100] de la Figuera, J., Carter, C. B., Bartelt, N. C. & Hwang, R. Q. Interplay between gas adsorption and dislocation structure on a metal surface. *Surf. Sci.* **531**, 29–38 (2003).

[101] Poirier, G. E. & Pylant, E. D. The self–assembly mechanism of alkenethiols on Au(111). *Science* **272**, 1145–1148 (1996).

[102] Fitts, W. P., White, J. M. & Poirier, G. E. Low-coverage decanethiolate structure on Au(111): substrate effects. *Langmuir* **18**, 1561–1566 (2002).

[103] Maksymovych, P., Sorescu, D. C. & John T Yates, J. Gold-adatom-mediated bonding in self–assembly short–chain alkanethiolate species on the Au(111) surface. *Phys. Rev. Lett.* **97**, 146103–1–146103–4 (2006).

[104] Dennert, R., Sokolowski, M. & Pfnur, H. Ordered phases and phase diagram of sulfur adsorbed on Ru(0001). *Surf. Sci.* **271**, 1–20 (1992).

[105] Dushman, S. & Lafferty, J. *Scientific foundations of vacuum technique* (John Wiley, New York, 1992).

[106] Hirth, J. P. & Lothe, J. *Theory of Dislocations* (McGraw–Hillbook Company, New York, 1993).

[107] Flatgen, G., Krischer, K., Pettinger, B., Doblhofer, K., Junkes, H. & Ertl, G. Two-Dimensional Imaging of Potential Waves in Electrochemical Systems by Surface Plasmon Microscopy. *Science* **269**, 668–671 (1995).

[108] Rocca, M., Valbusa, U., Gussoni, A., Maloberti, G. & Racca, L. Apparatus for adsorption studies. *Rev. Sci. Instrum.* **62**, 2172–2176 (1991).

[109] Hannon, J. B., Mele, E. J. & Plummer, E. W. Phonon dispersion at the Be(0001) surface. *Phys. Rev. B* **53**, 2090–2100 (1996).

[110] Hannon, J. B. & Dürr, H. private communication .

[111] Persson, B. N. J. & Zaremba, E. Electron-hole pair production at metal surfaces. *Phys. Rev. B* **31**, 1863–1872 (1985).

[112] Perdew, J. P. & Zunger, A. Self–interaction correction to density–functional approximations for many–electron systems. *Phys. Rev. B* **23**, 5048–5079 (1981).

[113] Silkin, V. M., Garcia-Lekue, A., Pitarke, J. M., Chulkov, E. V., Zaremba, E. & Echenique, P. M. Novel low-energy collective excitation at metal surfaces. *Europhys. Lett.* **66**, 260–264 (2004).

[114] Karlsson, U. O., Flodström, S. A., Engelhardt, R., Gädeke, W. & Koch, E. E. Intrinsic surface state on Be(0001). *Solid State Commun.* **49**, 711–714 (1984).

[115] Chulkov, E. V., Silkin, V. M. & Shirykalov, E. N. Surface electronic structure of Be(0001) and Mg(0001). *Surf. Sci.* **188**, 287–300 (1987).

[116] Silkin, V. M., Pitarke, J. M., Chulkov, E. V. & Echenique, P. M. Acoustic surface plasmons in the noble metals Cu, Ag, and Au. *Phys. Rev. B* **72**, 115435–115441 (2005).

[117] Politano, A., Chiarello, G., Formoso, V., Agostino, R. & Colavita, E. Plasmon of Shockley surface states in Cu(111): A high-resolution electron energy loss spectroscopy study. *Phys. Rev. B* **74**, 081401(R)–081404(R) (2006).